

Winter 2011

# Investigation of variables for wireless capacitive strain sensing on a CNC mill

Justin Patrick Bray

*University of New Hampshire, Durham*

Follow this and additional works at: <https://scholars.unh.edu/thesis>

---

## Recommended Citation

Bray, Justin Patrick, "Investigation of variables for wireless capacitive strain sensing on a CNC mill" (2011). *Master's Theses and Capstones*. 674.

<https://scholars.unh.edu/thesis/674>

This Thesis is brought to you for free and open access by the Student Scholarship at University of New Hampshire Scholars' Repository. It has been accepted for inclusion in Master's Theses and Capstones by an authorized administrator of University of New Hampshire Scholars' Repository. For more information, please contact [nicole.hentz@unh.edu](mailto:nicole.hentz@unh.edu).

INVESTIGATION OF VARIABLES FOR WIRELESS CAPACITIVE  
STRAIN SENSING ON A CNC MILL

BY

JUSTIN PATRICK BRAY

Baccalaureate of Science, University of New Hampshire, 2009

Submitted to the University of New Hampshire

In Partial Fulfillment of

The Requirements for the Degree of

Master of Science

in

Mechanical Engineering

December, 2011

UMI Number: 1507812

All rights reserved

**INFORMATION TO ALL USERS**

The quality of this reproduction is dependent upon the quality of the copy submitted.

In the unlikely event that the author did not send a complete manuscript and there are missing pages, these will be noted. Also, if material had to be removed, a note will indicate the deletion.



UMI 1507812

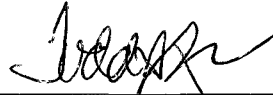
Copyright 2012 by ProQuest LLC.

All rights reserved. This edition of the work is protected against unauthorized copying under Title 17, United States Code.



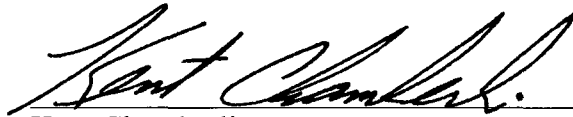
ProQuest LLC  
789 East Eisenhower Parkway  
P.O. Box 1346  
Ann Arbor, MI 48106-1346

This thesis has been examined and approved.



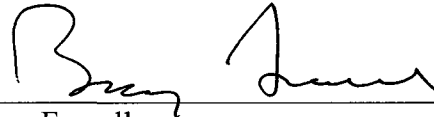
---

Thesis Director, Todd Gross,  
Professor and Chair of Mechanical Engineering



---

Kent Chamberlin,  
Professor of Electrical Engineering



---

Barry Fussell,  
Professor of Mechanical Engineering

12/19/11

---

Date

Dedicated to my parents, William and Diane Bray

## ACKNOWLEDGEMENTS

This research was made possible by support from the National Science Foundation Civil, Mechanical, and Manufacturing Innovation Division under grant number 0900054.

To begin, I would like to thank my advisors, Todd Gross and Kent Chamberlain. They have put in as much time molding me into a better engineer as I have put in to this research. They said that this research encountered more difficulties than any of their other projects, but as Jeff Potter said in *Cooking for Geeks* – “there’s not much to learn when things work. When they [the recipes] fail, you have a chance to understand where the boundary conditions are and an opportunity to learn how to save something in the future when things go awry.”

Next, I would like to express my appreciation for my family and friends. They have given me strength and guidance when the metaphorical ‘darkness’ in the tunnel, seemed to make me lose my way. To paraphrase, you are only as strong as the shoulders of those on whom you stand.

In addition, I'd like to thank my senior project mentor, Donald Troop, for his shining example of work ethic and infinite intelligence – his advice and guidance always help me keep my feet firmly planted on the ground. Also, thanks to Bob Champlin in the Mechanical Engineering’s Machine Shop for his amazing knowledge and insight for manufacturing processes.

Finally, a big thank to you to the mechanical and electrical departments’ technicians: Sheldon Parent and Adam Perkins for their insight and advice; while at times it seemed stiff, it was always astute and paved the way for a great learning experience.

## Table of Contents

ACKNOWLEDGEMENTS .....	IV
LIST OF TABLES .....	VII
LIST OF FIGURES .....	VIII
ABSTRACT .....	XIV
CHAPTER 1 .....	1
1.1 INTRODUCTION .....	1
1.2 SYSTEM OVERVIEW .....	3
1.3 PROOF OF CONCEPT .....	8
1.4 PREVIOUS WORK.....	15
1.4.1 Theoretical Analysis of Resonantly Coupled Antennas for Passive Sensors ..	16
1.4.2 Wireless Strain Detection via Deformable Resonant Cavity .....	17
1.4.3 Resonant Circuit Capacitive Pressure Sensor .....	18
1.4.4 Environmental Parameter Resonant Circuit Detection.....	19
1.4.5 Resonant Circuit for Strain Detection on a Planar Surface.....	22
1.4.6 Integrated Circuit Fabricated Vector Network Analyzer.....	24
CHAPTER 2 .....	26
2.1 LOOP GEOMETRY .....	26
2.2 PROBE DIAMETER.....	29
2.2.1 Theoretical Estimation .....	30
2.2.2 Experimental Results .....	37
2.3 LOAD BALANCING.....	39
2.4 CHAPTER SUMMARY.....	43
CHAPTER 3 .....	45
3.1 SENSOR CAPACITANCE .....	45
3.1.1 Discrete Capacitors .....	45
3.1.2 Parallel Plate Capacitors .....	49
3.2 INSERT MATERIAL.....	53
3.3 DIELECTRIC THICKNESS.....	60
3.4 SENSOR PERTURBATIONS .....	63
3.5 CHAPTER SUMMARY.....	68

CHAPTER 4 .....	70
4.1 SENSOR MATERIAL .....	70
4.2 ICCS DESIGN.....	72
4.3 TOOL DEFORMATION.....	76
4.4 ICCS ORIENTATION .....	78
4.5 CHAPTER SUMMARY.....	81
CHAPTER 5 .....	82
5.1 COMMERCIAL VECTOR NETWORK ANALYZER.....	82
5.2 IN-HOUSE FABRICATED VECTOR NETWORK ANALYZER.....	83
5.3 CHAPTER SUMMARY.....	89
CHAPTER 6 .....	90
CHAPTER 7 .....	92
7.1 SENSOR DESIGN .....	92
7.2 PROBE/DETECTION CIRCUITRY IMPLEMENTATION.....	93
7.3 DETECTION CIRCUITRY DESIGN .....	94
REFERENCES .....	96
APPENDICES .....	98



## LIST OF TABLES

Table 2-1 - Values for the probe self inductance and mutual inductance.....	32
Table 2-2 – Experimentally derived resonance parameters.....	38
Table 2-3 – Component values for the simplified schematic .....	39
Table 2-4 – Quality factors for probe loop with varying resistive impedance .....	43
Table 3-1 - Capacitance and resonant frequency information from discrete capacitors...	49
Table 3-2 - Capacitance and Resonant frequency information from overlap capacitor sensor loops.....	52
Table 3-3 - Quality factors for the insert materials tested .....	60
Table 3-4 - Sensor loop to tool separation distance.....	60

## LIST OF FIGURES

Figure 1.1 - Black box representation.....	4
Figure 1.2 - A capacitors reactance versus frequency curve (left) and an inductors reactance versus frequency curve (right) .....	5
Figure 1.3 - Inside the DUT .....	5
Figure 1.4 - Illustration of input frequency DUT behavior .....	6
Figure 1.5 - Reactance plot showing resonance and impedance plot showing resonance for LC circuit.....	6
Figure 1.6 - Equivalent resonant circuit representation.....	7
Figure 1.7 - Schematic and actual DUT representation.....	7
Figure 1.8 - Tool bit with mounted sensor loop.....	8
Figure 1.9 - Probe loop physical structure .....	9
Figure 1.10 - Sensor loop mounted on aluminum tube.....	9
Figure 1.11 - Loading case/overlap capacitor parameters (left), and sensor coordinate system (right) .....	10
Figure 1.12 - Predicted resonant frequency response versus applied strain .....	12
Figure 1.13 - Compressive loading experimental set up.....	12
Figure 1.14 – Experimentally obtained normalized change in frequency versus strain plot .....	13
Figure 1.15 - Frequency variation due to vertical displacement (a star represents Frequency and a circle represents $\Delta f/f_0$ ).....	14
Figure 1.16 - Simulated and experimental change in frequency versus strain .....	15
Figure 1.17 - Resonant cavity assembly (top and middle) and resonant cavity exhibiting the dominant lowest TEM mode (6) .....	18
Figure 1.18 - Structure of pressure sensitive resonant circuit (7) .....	19
Figure 1.19 - a) Parallel plate capacitor resonant circuit, b) Interdigitated comb capacitor resonant circuit (8).....	20
Figure 1.20 - Left: Two loop sensing system and response, Right: One loop sensing system and response.....	21

Figure 1.21 - Resonant circuit schematic and physical layout (5).....	22
Figure 2.1 - Probe loops: 12.7 mm ID loop (a), 35.6 mm ID loop (b), 39.6 mm square (c) .....	27
Figure 2.2 - Equipment: VNA 75 ohm Type-N port (a), 50 ohm Type-N to 50 ohm SMA adapter (b), .....	27
Figure 2.3 – Magnitude and phase response for the equipment shown in Figure 2 .....	27
Figure 2.4 - Probe loop impedance response .....	28
Figure 2.5 - Sensor mounted to copper cylinder .....	29
Figure 2.6 – Probe loops (left to right): 14.53 mm, 15.09 mm, and 15.54 mm.....	30
Figure 2.7 - Experimental set up and close-up picture of probe/sensor loop .....	30
Figure 2.8 - Cross-sectional view of probe, sensor, and insert .....	31
Figure 2.9 - Circuit representation illustrating the lumped components of the system ....	31
Figure 2.10 - Skin depth as a function of frequency .....	33
Figure 2.11 - Sensor/insert cross-section .....	33
Figure 2.12 - Copper insert inductance as a function of frequency .....	34
Figure 2.13 - Total system inductance as a function of frequency .....	35
Figure 2.14 - Geometrical variables for probe, sensor, and insert (cross-section view)...	35
Figure 2.15 - Probe loop resistance versus frequency using Equation 1.11 .....	36
Figure 2.16 - Left: Sensor loop resistance versus frequency; Right: Insert material resistance versus frequency.....	36
Figure 2.17 - Total system resistance as a function of frequency.....	36
Figure 2.18 - 14.53 mm ID probe loop and sensor loop mounted on copper cylinder response.....	37
Figure 2.19 - 15.09 mm ID probe loop and sensor loop mounted on copper cylinder response.....	37
Figure 2.20 - 15.54 mm ID probe loop and sensor loop mounted on copper cylinder response.....	38
Figure 2.21 - Simplified resonant circuit .....	38

Figure 2.22 –Loop Electrical Schematics: A) No resistance, B) 75 $\Omega$ on input terminal, C) 75 $\Omega$ on ground terminal, and D) 36 $\Omega$ on input and ground terminals.....	40
Figure 2.23 - Probe Loops (clockwise from top left): no resistance, 75 $\Omega$ on input terminal, 36 $\Omega$ on input and ground terminals, and 75 $\Omega$ on ground terminal.....	41
Figure 2.24 - Sensor loop and tool bit.....	41
Figure 2.25 – Response for no resistance probe loop .....	42
Figure 2.26 – Response for 75 $\Omega$ on input terminal probe loop .....	42
Figure 2.27 - Response for 75 $\Omega$ on ground terminal probe loop .....	43
Figure 2.28 - Response for 36 $\Omega$ on input and ground terminals probe loop .....	43
Figure 3.1 - Tool bit with sensor loops with varying capacitance .....	46
Figure 3.2 - Probe loop used to excite the 0.1 to 1.5 pF sensor loops .....	46
Figure 3.3 - Photo of experimental set-up .....	47
Figure 3.4 - System response for probe loop .....	47
Figure 3.5 - System response for 0.2 pF sensor loop.....	47
Figure 3.6 - Close up of 11.55 pF solder connections and sensor loop .....	48
Figure 3.7 - SMB connector/ probe loop and experimental set-up.....	48
Figure 3.8 - System response due to only SMB loop .....	49
Figure 3.9 - System response for 11.55 pF sensor loop.....	49
Figure 3.10 - Sensor loop with parallel plate capacitor .....	50
Figure 3.11 - Tool bit with three overlap-type sensor loops, only one of which is being monitored externally .....	50
Figure 3.12 - Simulated capacitance variation due to manufacturing tolerance using equation 1.3.....	51
Figure 3.13 – Simulation for variation in relative permittivity using equation 1.3 .....	51
Figure 3.14 – System response due to 1.968 pF sensor loop with narrowed frequency range.....	51
Figure 3.15 - System response for 5.89 pF sensor loop.....	51

Figure 3.16 - Resonant frequency vs. sensor loop capacitance .....	52
Figure 3.17 - Interdigitated capacitor and vias .....	53
Figure 3.18 - Sensor loop on polycarbonate cylinder .....	54
Figure 3.19 – Polycarbonate sensor loop inside probe loop .....	54
Figure 3.20 - Polycarbonate mounted sensor loop response.....	55
Figure 3.21 - Sensor loop on copper cylinder.....	55
Figure 3.22 – Copper sensor loop inside probe loop .....	55
Figure 3.23 - Copper mounted sensor loop response.....	56
Figure 3.24 - Sensor loop on high strength steel tool bit.....	56
Figure 3.25 – HSS sensor loop inside probe loop.....	56
Figure 3.26 - High strength steel tool bit mounted sensor loop response.....	57
Figure 3.27 - Sensor loop on carbide tool bit.....	57
Figure 3.28 – Carbide sensor loop inside probe loop .....	57
Figure 3.29 - Carbide tool bit mounted sensor loop response .....	58
Figure 3.30 - Sensor loop on HSS .....	58
Figure 3.31 – Carbide sensor loop inside probe loop .....	58
Figure 3.32 - System response of sensor loop with Ag/Cu standoff on HSS tool bit.....	59
Figure 3.33 - System response of sensor loop with Ag/Cu standoff on carbide tool bit ..	59
Figure 3.34 - Sensor loops mounted on carbide tool bit.....	61
Figure 3.35 - Only Probe Loop's response.....	62
Figure 3.36 - Probe loop and no-standoff sensor response.....	62
Figure 3.37 - Probe loop and one-ply standoff sensor response .....	63
Figure 3.38 - Probe loop and two-ply standoff sensor response.....	63
Figure 3.39 – Equipment layout and coordinate system.....	64
Figure 3.40 - Close-up of Pyralux sensor on Aluminum tube .....	65

Figure 3.41 - Double turn PCB probe loop.....	65
Figure 3.42 - Photo of experimental set-up showing rotational and translational stages .	65
Figure 3.43 - Resonant frequency variation due to x-direction displacement .....	66
Figure 3.44 - Resonant frequency variation due to y-direction displacement .....	67
Figure 3.45 - Resonant frequency variation due to z-direction displacement .....	68
Figure 3.46 - Normalized change in frequency for various displacement directions .....	68
Figure 4.1 - Simplified sensor loop representation.....	70
Figure 4.2 - 2-layer flexible circuit construction (16).....	71
Figure 4.3 - Strain sensitive areas (red cross-hatched) for sensors with different number of fingers .....	73
Figure 4.4 - Torsional strain sensors on the same assembly (equal number fingers, differing length of fingers).....	73
Figure 4.5 - Left is the circuit schematic representation, right is the board .....	73
Figure 4.6 - Perspective, Top, Side, and Bottom view of Sensor assembly .....	74
Figure 4.7 – Parametric view of assembly with associated capacitance.....	74
Figure 4.8 - Side View of assembly with associated capacitance.....	74
Figure 4.9 - Expanded capacitance for sensor loop assembly .....	75
Figure 4.10 – ICSS designs: A) fixed via to via distance, B) fixed via to sensor distance, and C) sensor without vias.....	75
Figure 4.11 – Left: Via connection with parallel plate capacitance, Right: Via connection with negligible parallel plate capacitance .....	76
Figure 4.12 - Work piece and tool bit during cutting process (18).....	76
Figure 4.13 - Undeformed tool (a), tool exhibiting bending stress (b), and tool exhibiting torsional stress (c) .....	77
Figure 4.14 - Bending Sensor .....	77
Figure 4.15 - Torsional Sensor.....	77
Figure 4.16 - Comb capacitor orientations .....	78

Figure 4.17 - Comb capacitor orientation perpendicular to force application and resulting output .....	79
Figure 4.18 - Comb capacitor orientation parallel to force application and resulting output .....	79
Figure 4.19 - Pure shear strained differential element.....	80
Figure 4.20 - Complex strain state differential element .....	80
Figure 5.1 - Simplified version of Vector Network Analyzer .....	83
Figure 5.2 - Block diagram for the resonance detection circuit, Phase 1 .....	84
Figure 5.3 - Block diagram for the resonance detection circuit, Phase 2 .....	85
Figure 5.4 - Block diagram of the resonance detection circuit, Phase 3.....	86
Figure 5.5 - Front and Top View of actual Detection Circuit and Probe Loop .....	87
Figure 5.6 - VNA captured magnitude and phase plot .....	88
Figure 5.7 – Averaged magnitude plot and corresponding standard deviation .....	88
Figure 5.8 – Averaged phase plot and corresponding standard deviation .....	89
Figure 7.1 - SMT MLCC and internal design (21) .....	92
Figure 7.2 - Loop mounted parallel to ground plane .....	93
Figure 7.3 - Loop mounted perpendicular to ground plane .....	93
Figure 7.4 - Block diagram for resonance detection circuit, Phase 4, Final Design.....	94

## ABSTRACT

### INVESTIGATION OF VARIABLES FOR WIRELESS CAPACITIVE STRAIN SENSING ON A CNC MILL

by

Justin Bray

University of New Hampshire, December, 2011

As demand in the manufacturing sector increases, so does the need for greater process throughput and reduced component variability. These two objectives can be achieved by a process known as ‘smart machining’. Smart machining utilizes sensors inside the machining environment to relay information to the machine controller. Most sensor systems adversely affect the machine dynamics, by reducing the machining envelope or reducing the machine’s stiffness, or require physical connections to conditioning electronics. In this research, variables regarding a resonantly coupled wireless capacitive strain sensor were investigated. A parallel plate capacitive sensor prototype system yielded a strain sensitivity five times greater than analytical predictions. Experimental investigations were performed on probe design, sensor design, and application dynamics. Computer simulations were performed for the change in capacitance of an interdigitated comb capacitor for simplified loading cases. Finally, a simplified resonance detection circuit attached to the probe loop was designed, assembled, and successfully tested.



## CHAPTER 1

### 1.1 INTRODUCTION

In the early part of the 20 century, the metal-cutting process was controlled by an experienced machinist. The machine's parameters, such as feed rate and spindle speed, were determined and controlled by the machinist's hand. Therefore, the complexity and quality of the part was primarily dependent on the skill of the machinist.

With the onset of the computer era, the human controlled machine was transformed to a computer numerically controlled (CNC) machine. This transformation allowed for faster throughput of complex designs and the removal of the dependence on the machinist's skill. As the demand for production increased, engineers and scientists began focusing on aspects of machining to improve output and reduce tool failure. To make these improvements, they needed to understand what was going on inside the machining environment. This led to the design and implementation of sensors. This information was used to make observations and conclusions. However, from a control system engineer's perspective, this presented an opportunity for closed loop feedback control.

Smart machining is the process in which information gathered from sensors in the machining environment is allowed to manipulate machine control parameters. The types of sensors found in the machining environment can be classified into two categories: non-intrusive and intrusive. Non-intrusive sensors do not alter the machines dynamics and only in-directly provide cutting force information, whereas intrusive sensors can provide direct measurement of cutting force parameters but can add additional measurement

dynamics. An example of a non-intrusive sensor is a microphone, whose signal can be analyzed with Harmonizer to detect chatter in a tool bit (1). An example of an intrusive sensor is a Kistler force dynamometer located below the work piece and vise. This sensor provides direct measurement of cutting forces at the tool bit/work piece interface. The microphone is a non-contact observer, whereas the force dynamometer decreases the machine's stiffness and reduces the machining envelope.

An alternative method to the Kistler dynamometer has been designed by our colleagues at the Design and Manufacturing Lab at the University of New Hampshire. They mounted resistive based strain gages in the tool holder to measure cutting forces at the tool bit/ work piece interface. This method requires electronics to be located in the tool holder for power distribution, signal processing, and data transmission. A detraction of this design is the need for a specialized tool holder and periodic charging of the on-board power supply. Our system improves and simplifies the design by measuring the strain closer to the tool bit/work piece interface because the strain sensor would be located on the shank of the tool bit rather than in the tool holder, and removing the need for electronics in the tool holder. We employed a strain sensitive resonant circuit to achieve this goal.

A resonant circuit can be wirelessly energized and remotely monitored for cutting force measurements. The sensor, and an inductive loop placed around the tool shank, completes a resonant circuit. The advantages of this design are the simplicity, low cost, ease of implementation, and real-time measurement. Although, a drawback as with any measurement system is bandwidth limitation.

In this thesis, we investigate variables for a capacitively-based strain gage resonant circuit system for use on a CNC mill. In the remainder of this chapter, we present an overview of the system, results from a prototype proof-of-concept experiment, and summarize relevant past research. Chapter 2 discusses theoretical and experimental results regarding the probe loop portion of the system, such as design, geometry, and load balancing. Experiments for the characterization of the sensor loop, including effects due to insert material and sensor loop displacement, are presented in Chapter 3. Chapter 4 describes interdigitated comb capacitor design and strain versus change in capacitance simulation results for simplified loading cases. The system used for resonance detection and thus strain detection is detailed in Chapter 5. The in-house fabricated resonance detection circuit design and results are presented. Finally, conclusions are presented in Chapter 6 and future work is discussed in Chapter 7.

The specific questions which were investigated in this thesis are as follows. Can strain in a metallic cylindrical structure be detected wirelessly with a completely passive circuit? What is the impact of the shape of the probe loop? Does displacing the sensor circuit farther from the insert material yield a higher quality factor for the resonance? Can a simplified resonance detection circuit yield results comparable to a commercially available Vector Network Analyzer?

## **1.2 SYSTEM OVERVIEW**

The system we used to detect strain contains several sub-systems. Immediate analysis of the sub-systems without an understanding of their interplay can cause confusion. This section begins with an upper level representation of the system, and then adds complexity illustrating the components while maintaining understanding.

The entire system can be represented as a black box, shown in Figure 1.1 as the device under test (DUT). In this schematic, radio frequency (RF) signals are sent via the 50 ohm characteristic impedance path (Input) and those signals are altered by the DUT and then returned through the 50 ohm impedance path (Output).

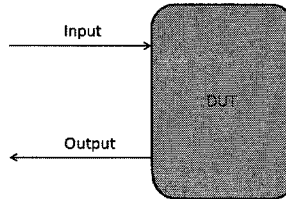


Figure 1.1 - Black box representation

The RF signals that we are referring to are electro-magnetic waves comprised of both a voltage and current waveform. If the DUT is purely resistive, the voltage and current waveforms are in-phase. If the DUT is capacitive, the current waveform will lead the voltage waveform. Lastly, if the DUT is inductive, the voltage waveform will lead the current waveform. These phase relations are important because they enable us to characterize the black box from the voltage and current waveforms.

In addition to the voltage and current waveform relation of inductors and capacitors, their reactances are also a function of frequency. For example, at low frequencies a capacitor's reactance can be represented as an open circuit and at high frequencies its reactance can be represented as a short circuit. An example application of this is when capacitors are used as DC-blocks. Inductors are the dual of capacitors, where an inductor's reactance at low frequencies can be represented as a short circuit and at high frequencies its reactance can be represented as an open circuit. An example application of this is when inductors are used as RF-blocks. Figure 1.2 shows plots of a capacitor's reactance ( $X_C$ ) and an inductor's reactance ( $X_L$ ) as a function of frequency.

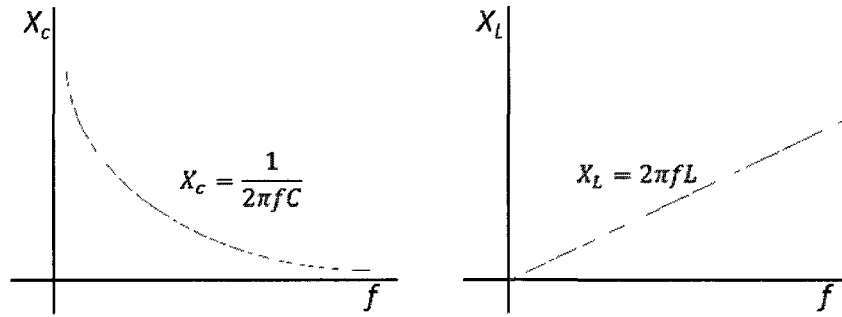


Figure 1.2 - A capacitors reactance versus frequency curve (left) and an inductors reactance versus frequency curve (right)

For our system, the interior of the DUT is both capacitive and inductive, this is known as an LC-tank circuit. If we step into the DUT and remove the black box representation, the system resembles Figure 1.3.

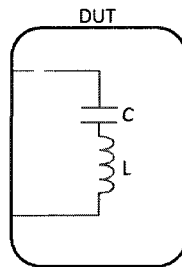


Figure 1.3 - Inside the DUT

In this configuration, if the input frequency is below a specific frequency (known as the resonant frequency,  $f_{res}$ ) the device exhibits behavior similar to that of a capacitor. If input frequency is greater than that of the resonant frequency, then the device exhibits behavior similar to that of an inductor (2). Finally, if the input frequency is equal to that of the resonant frequency, the reactance's of the inductor and capacitor cancel resulting in a short circuit condition. This concept is illustrated in Figure 1.4 and shown in graphical form in Figure 1.5. The relationship between reactance and impedance is shown in Equation 1.1, where  $Z$  is the impedance.

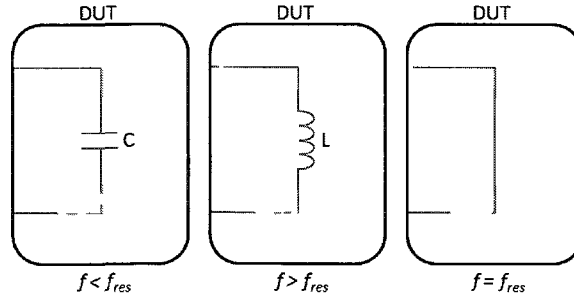


Figure 1.4 - Illustration of input frequency DUT behavior

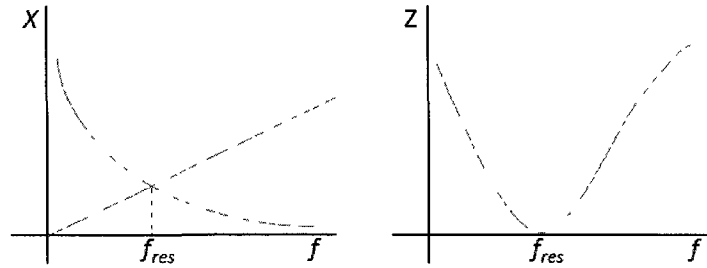


Figure 1.5 - Reactance plot showing resonance and impedance plot showing resonance for LC circuit

$$Z = \sqrt{[X_L(f) - X_c(f)]^2} \quad (1.1)$$

The impedance plot shown in Figure 1.5 is stationary if the inductive and capacitive component values are constant. The value of the resonant frequency can be calculated from

$$f_{res} = \frac{1}{2\pi\sqrt{L * C}} \quad (1.2)$$

where  $f_{res}$  is the resonant frequency of the system,  $L$  is the inductance, and  $C$  is the capacitance. In this relation, if we replace the fixed capacitor with a variable capacitor, then the location of the resonant frequency will vary according to the above equation. A variable capacitive element is typically represented in schematics by an arrow across the capacitor, as shown in Figure 1.6 below.

To more closely represent the system, additional complexity will be added to the DUT from Figure 1.3. Figure 1.6 shows functionally equivalent resonant circuits.

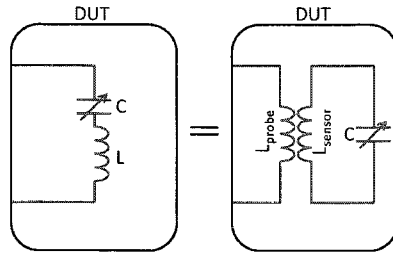


Figure 1.6 - Equivalent resonant circuit representation

The purpose of our system is to measure strain wirelessly. The DUT to the left shows a physically connected resonant circuit and to the right is an inductively coupled resonant circuit. This configuration allows for wireless transfer of energy and resonant information (3), yielding a completely passive sensor loop. Figure 1.7 shows the schematic DUT representation, the physical/schematic DUT representation, and the actual DUT. In the actual DUT image, the green is the FR-4 substrate and the gold is conductor. The structure labeled  $L_{probe}$  is what we refer to as the probe loop, and the structure labeled  $L_{sensor}$  is what we refer to as the sensor loop.

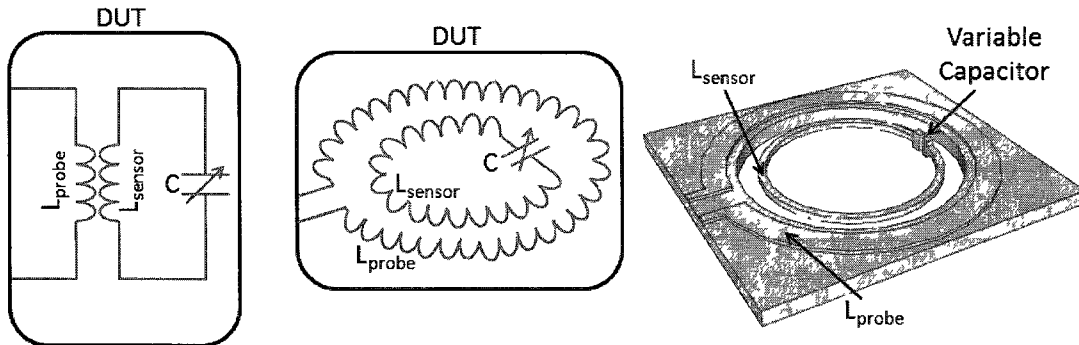


Figure 1.7 - Schematic and actual DUT representation

The sensor loop is mounted to the shank of the tool bit. Figure 1.8 shows a CAD model of a 2 flute end mill tool bit with an interdigitated comb capacitor sensor loop. The comb capacitor converts the mechanical deformation of the tool bit during the cutting process to a change in capacitance. This change in capacitance from the undeformed state of the tool bit to the deformed state of the tool bit will cause a change in resonant frequency of the system. The change in resonant frequency can be calibrated to

reflect the change in strain of the tool, thus resulting in a wireless method to monitor strain on the tool bit.

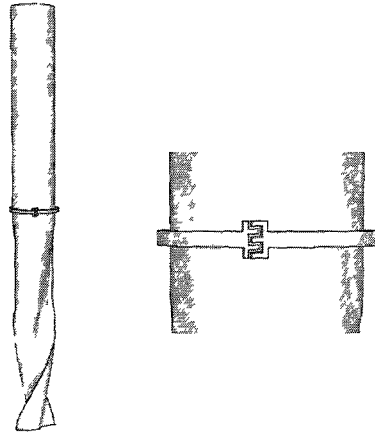


Figure 1.8 - Tool bit with mounted sensor loop

### **1.3 PROOF OF CONCEPT**

The purpose of this experiment was to show that an external probe loop can wirelessly detect a strain signal produced by a capacitively-terminated sensor loop. We measured strain with an extensometer and correlated it with the resonant frequency shift. The resonant frequency of the system was defined by the zero crossing in the  $S_{11}$  phase data.  $S_{11}$  is the input port voltage reflection coefficient and was measured at the probe circuit input port. This zero crossing is indicative of resonance because it is a result of when the reactive components of the load cancel.

The probe loop we used to interrogate the sensor loop was a 35.55 mm inner diameter circular loop with a copper trace width of 0.6 mm and lead spacing of 2.92 mm on 1.39 mm thick FR-4 substrate. The probe loop was connected to the vector network analyzer (VNA) with a 50-ohm subminiature type A (SMA) end launch connector. Figure 1.9 shows the probe loop used for this experiment.



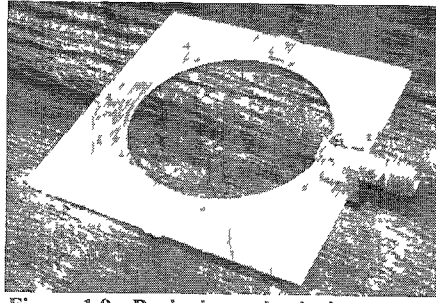


Figure 1.9 - Probe loop physical structure

The sensor loop was a 4.18 mm wide pyralux LF9120R band wrapped around a 31.67 mm outer diameter aluminum tube. The Pyralux material had a copper thickness of  $\sim 50 \mu\text{m}$ , an acrylic adhesive thickness of  $25 \mu\text{m}$ , and a DuPont Kapton polyimide film thickness of  $25 \mu\text{m}$ . The strain sensitive capacitive sensor was produced by overlapping the ends of the Pyralux and joining them with cyanoacrylate. The overlap area had a length of 7.2 mm and a width of 4.18 mm. This configuration of pyralux yields a parallel plate capacitive structure. The capacitance of this structure was estimated to be 3.2 pF using the following relation

$$C = \frac{A\epsilon_0\epsilon_r}{D} \quad (1.3)$$

where  $A$  is the overlap area,  $\epsilon_0$  is the permittivity of free space,  $\epsilon_r$  is the relative permittivity of the medium, and  $D$  is the plate separation distance. The parallel plate structure is sensitive to strain because the overlap area changes due to the mechanical deformation (strain) of the aluminum tube. This change in overlap area causes a change in capacitance which results in a change of system resonant frequency. Figure 1.10 shows a close up picture of the overlap area/sensor loop.

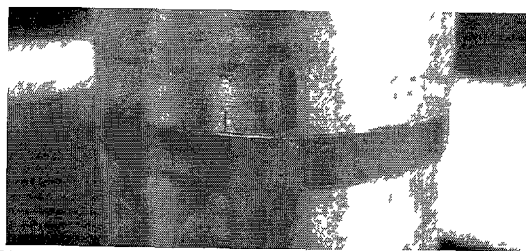


Figure 1.10 - Sensor loop mounted on aluminum tube

Figure 1.11 shows a CAD model displaying the uniaxial loading case, the definition of the sensors geometric variables, and a coordinate system at the sensor location used for strain identification. The blue represents aluminum, the yellow represents copper, and red represents polyimide.

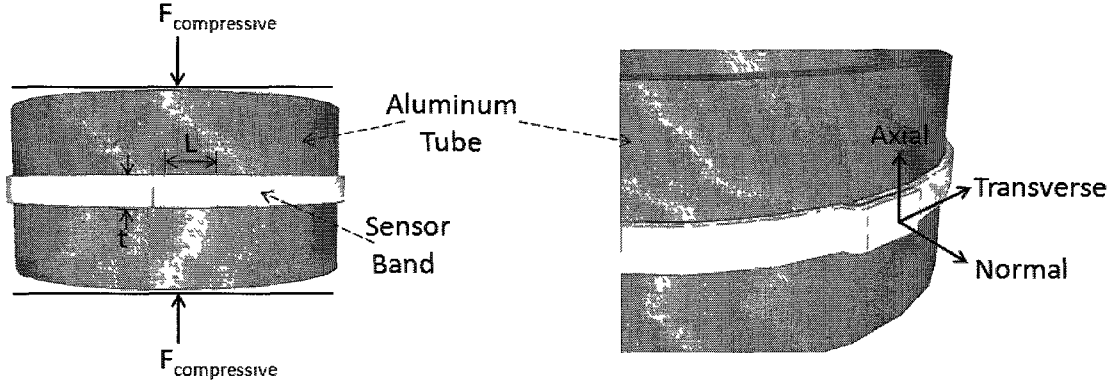


Figure 1.11 - Loading case/overlap capacitor parameters (left), and sensor coordinate system (right)

The expected change in capacitance due to applied strain can be mathematically predicted using equation 1.3. First we substitute the respective geometrical parameters for the overlap area, yielding a capacitance equation of

$$C = \frac{l \times t \times \varepsilon}{D} \quad (1.4)$$

where  $\varepsilon = \varepsilon_0 \varepsilon_r$ ,  $l$  is the length of the overlap area, and  $t$  is the height of the overlap area.

We take the derivative of Equation 1.4 to produce an equation that shows a differential change in the capacitors physical parameters.

$$dC = \frac{t * \varepsilon}{D} dl + \frac{l * \varepsilon}{D} dt - \frac{l * t * \varepsilon}{D^2} dD \quad (1.5)$$

Substituting Equation 1.4 into Equation 1.5, the normalized change in the physical parameters becomes apparent.

$$dC = C_0 \frac{dl}{l} + C_0 \frac{dt}{t} - C_0 \frac{dD}{D} \quad (1.6)$$

where  $C_0$  is the unstrained capacitance value. Mechanical strain is defined as the ratio of elongation normalized with respect to the original length (4)

$$d\epsilon = \frac{dX}{X} \quad (1.7)$$

where  $\epsilon$  is strain and  $X$  is the original length of the element. Replacing the differential terms of Equation 1.6 with their respective strains yields

$$dC = C_0 d\epsilon_{\text{axial}} + C_0 d\epsilon_{\text{transverse}} - C_0 d\epsilon_{\text{normal}} \quad (1.8)$$

where  $\epsilon_{\text{axial}}$  is the strain in the axial direction,  $\epsilon_{\text{transverse}}$  is the strain in the transverse direction, and  $\epsilon_{\text{normal}}$  is the strain in the normal direction. Given that the aluminum tube was loaded in a uniaxial fashion, the strain in the transverse and normal directions can be replaced with Poisson's ratio ( $\nu$ ) and the axial strain ( $\epsilon_{\text{axial}}$ ). The change in capacitance can therefore be written as

$$dC = C_0 d\epsilon_{\text{axial}} + C_0(-\nu)d\epsilon_{\text{axial}} - C_0(-\nu)d\epsilon_{\text{axial}} \quad (1.9)$$

which reduces and integrates to

$$\Delta C = C_0 \epsilon_{\text{axial}} \quad (1.10)$$

Given Equation 1.2 that defines a resonant circuit, we can write a relation for the change in frequency of a resonant circuit based on a change in capacitance

$$\Delta f = \frac{1}{2\pi\sqrt{LC_0}} - \frac{1}{2\pi\sqrt{L(C_0 + \Delta C)}} \quad (1.11)$$

Substituting Equation 1.10 into Equation 1.11 yields a resonant frequency relationship for strain.

$$\Delta f(\epsilon_{\text{ax}}) = \frac{1}{2\pi\sqrt{LC_0}} - \frac{1}{2\pi\sqrt{LC_0(1 + \epsilon_{\text{ax}})}} \quad (1.12)$$

Equation 1.12 can be simplified using a first order Taylor series for small values of strain yielding

$$\Delta f(\epsilon_{\text{ax}}) = \frac{\epsilon_{\text{ax}}}{4\pi\sqrt{LC_0}} \quad (1.13)$$

Figure 1.12 shows the predicted normalized change in resonant frequency for an applied strain of 1 to 1100  $\mu\epsilon$ .

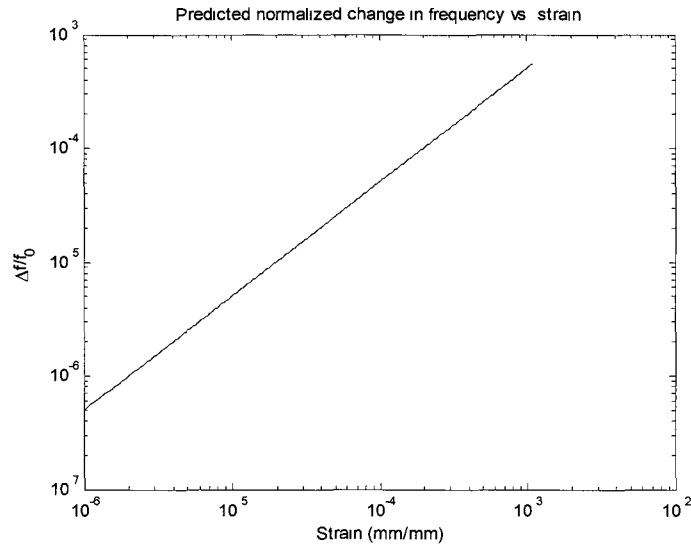


Figure 1.12 - Predicted resonant frequency response versus applied strain

The aluminum tube was compressively loaded with an Instron model 1350 material testing machine. An extensometer was physically mounted to the aluminum tube, in close proximity to the overlap section of the sensor, to directly measure the strain. The tube was loaded to a value of strain below the elastic limit of the aluminum, to prevent buckling and non-linear behavior. Figure 1.13 shows the experimental set up and VNA used for data collection.

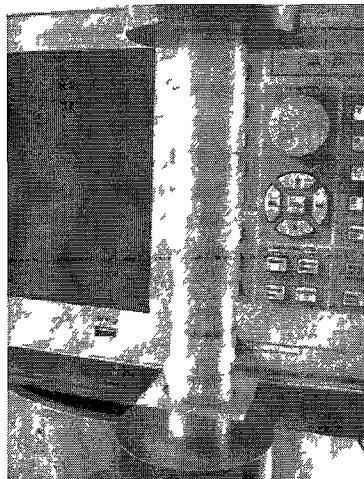


Figure 1.13 - Compressive loading experimental set up

Figure 1.14 shows the normalized change in frequency versus strain for the aluminum tube sensor. The dashed line represents the experimental data from the loading

and unloading of the specimen. The inconsistency of the process was believed to be caused by a materials properties change of the adherent (5). A least squares regression fit was applied to the data to determine the linear relationship between the normalized frequency change and the strain, this relationship is shown in Equation 1.14. The value for the coefficient of determination for this fit to the data is 0.9586.

$$\frac{\Delta f}{f_0} = 2.4943\varepsilon - 0.0002 \quad (1.14)$$

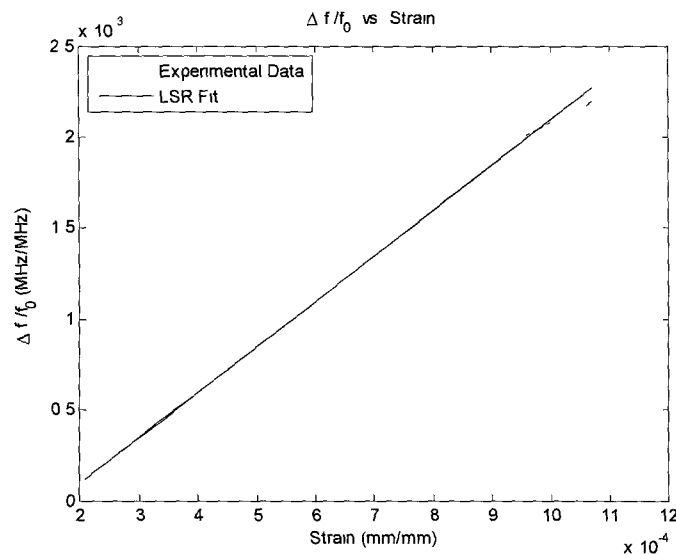


Figure 1.14 – Experimentally obtained normalized change in frequency versus strain plot

We verified the measurement was not a result of the vertical displacement of the sensor by traversing the unloaded sensor and tube assembly vertically through the probe loop and measuring the response. Figure 1.15 shows the frequency and normalized change in frequency due to shifting the tube a distance of  $\pm 2$  mm, where zero on the abscissa is when the sensor loop is coplanar with the probe loop.

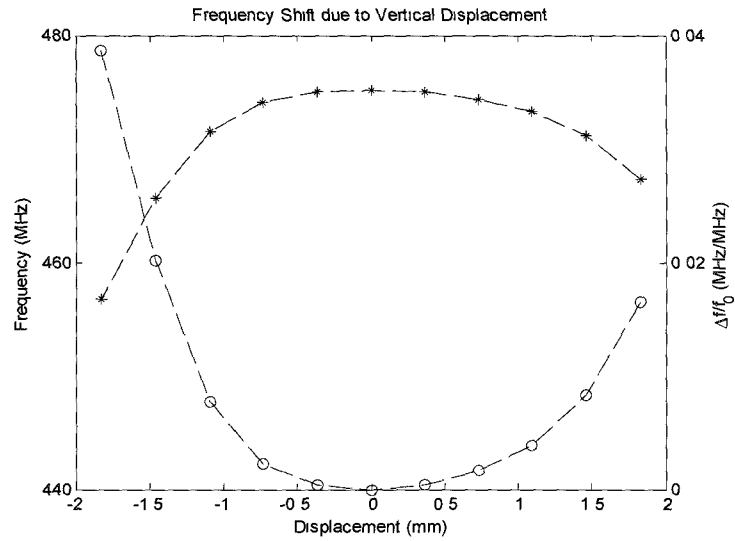


Figure 1.15 - Frequency variation due to vertical displacement (a star represents Frequency and a circle represents  $\Delta f/f_0$ )

Given the original length of the aluminum tube was 180.97 mm and the maximum strain applied to the tube during the loading experiment was 0.0011, using Equation 1.7 the maximum vertical shift the sensor experienced was 199  $\mu\text{m}$ . We interpolate the change in normalized frequency for a 199  $\mu\text{m}$  vertical displacement (using Figure 1.15) to be  $2.1 \cdot 10^{-4}$ . The unstrained maximum vertical shift produced less than 10 % of the signal when compared to the strained response.

Figure 1.16 shows the predicted normalized change in resonant frequency and the experimentally derived fit versus strain.

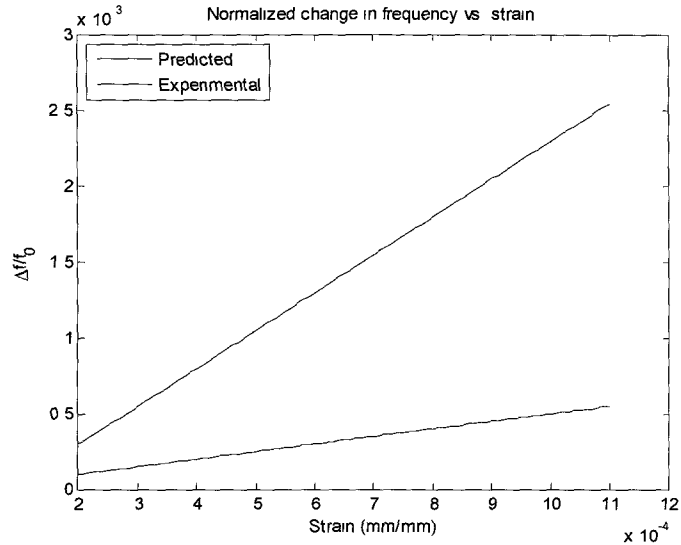


Figure 1.16 - Simulated and experimental change in frequency versus strain

The experimental result shows a greater resonant frequency to strain sensitivity than was estimated with our prediction. The slope of the experimental fit is 5 times higher than the prediction and the source that caused this difference is not yet known. Further effort was not invested to resolve the deviation because these results provide the foundation needed for the proof of concept.

This experiment shows that the measuring of strain produced by a stationary capacitively-terminated sensor loop wirelessly using inductive coupling was possible.

#### **1.4 PREVIOUS WORK**

The following section denotes relevant work from past research and publications regarding resonant circuits. We begin with Resonant Coupled Antennas for Passive Sensors, which explores the theory and analysis of a passive sensor in a resonant circuit. Then we look at an application of a resonant circuit in “*Embeddable Wireless Strain Sensor based on Resonant RF Cavities*” (6) where they measure strain, through the deformation of a resonant cavity, in a concrete column. Then we discuss an application

of a capacitive transducer in a resonant circuit for pressure detection in “*A Wireless Batch Sealed Absolute Capacitive Pressure Sensor*” (7). Next, we summarize “*Resonant Printed Circuit for Monitoring of Environmental Parameters*” (8) and “*Design and Characterization of a Passive Wireless Strain Sensor*” (5) which utilize interdigitated capacitive transducers to detect environmental variables and mechanical deformation, respectively. We conclude this section with an application note titled Vector-SOC, which describes the design procedure for producing an ultra-high frequency network analyzer.

#### **1.4.1 Theoretical Analysis of Resonantly Coupled Antennas for Passive Sensors**

Rindorf, Lading and Breinbjerg present an analysis based on the theory of using resonantly-coupled circuits for passive wireless sensor interrogation in their paper “*Resonantly Coupled Antennas for Passive Sensors*” (9). They describe how the quality factor (Q) of the transceiver and the device circuits relates to the transfer coefficient for magnetically inductive antennas. The Q-factor for the transceiver circuit is a function of the transceiver radiation resistance and ohmic losses, whereas the Q-factor for the device circuit is dependent on the devices radiation resistance, ohmic losses, and the passive sensors Q-factor.

As an example, they analyzed a device circuit whose change in capacitance variation can be detected via the transceiver input impedance. A figure-of-merit for this circuit is constructed based on the expected value of the estimator for the change in input impedance with a change in capacitance. From this analysis, they state that an “optimum transceiver Q is generally close to the Q of the sensing circuit” (9).



#### **1.4.2 Wireless Strain Detection via Deformable Resonant Cavity**

Chuang, Thomson, and Bridges designed and fabricated an embeddable wireless strain sensor based on a resonant RF cavity for applications in structural health monitoring. Shown in Figure 1.17, the resonant device is a closed, cylindrical cavity with a small wire probe mounted in the middle of the longitudinal direction of the cylinder with its center conductor extending into the center of the cavity. The resonant frequency of the device is inversely proportional to the length of the cavity. The change in resonant frequency from the undeformed cavity to the deformed cavity yields the strain information.

This device is communicated to wirelessly by receiving electromagnetic waves with a loop antenna and directing them to the probe port with a waveguide. Their detection system works on a call and answer method in which they sweep an RF bandwidth and then monitor the response to determine the resonant frequency in the cavity. The cavity they designed had a resonant frequency of 2.42 GHz and a Q-factor of 2000. Due to the high Q-factor of the cavity and the time-domain gating function of the RF switch, Chuang et al said the reflections due to the environment are expected to die out quickly when compared to the cavity's response.

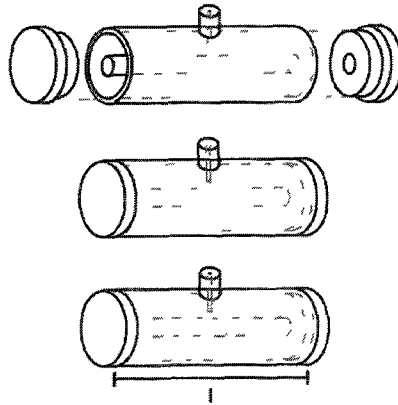


Figure 1.17 - Resonant cavity assembly (top and middle) and resonant cavity exhibiting the dominant lowest TEM mode (6)

### **1.4.3 Resonant Circuit Capacitive Pressure Sensor**

Akar, Akin and Najafi designed and fabricated a pressure-sensitive resonant circuit composed of a pressure-sensitive capacitor and planar coil, shown in Figure 1.18. The pressure sensing element was a parallel-plate capacitor, in which one plate was connected to a deformable silicon diaphragm and other plate was fixed to a glass substrate. The planar coil was a 24-turns gold-electroplated inductor with a measured inductance value of  $1.2 \mu\text{H}$  and a maximum Q-factor of 8 at 103 MHz. The resonant circuit was produced in a sealed cavity  $2.6 \text{ mm} \times 1.6 \text{ mm}^2$  in size, and was communicated to via wireless inductive coupling. The resonant circuit was energized by an external 3 mm diameter 10-turns hand-wound coil parallel to the planar coil separated by a vertical distance of 2mm. The resonant behavior was measured with an impedance analyzer connected to the external coil. They state that the sensor's resonant frequency change "is more detectable if the phase of  $Z_e$  [the impedance of the reader antenna] is monitored" (7). Their sensors were designed for a dynamic range of 0-50 mmHg and they produced a measured pressure responsivity and sensitivity of 120 kHz/mmHg and 1579 ppm/mmHg, respectively.

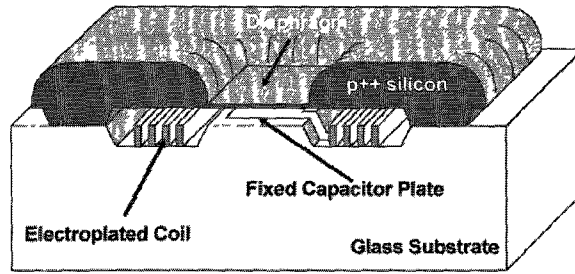


Figure 1.18 - Structure of pressure sensitive resonant circuit (7)

#### **1.4.4 Environmental Parameter Resonant Circuit Detection**

Ong and Grimes designed and produced two different types of resonant circuits for monitoring of environmental parameters. The two circuits differed by the design of the sensing capacitor. The capacitor that was assembled to sense pressure differences used a parallel-plate design and the other, which was built to sense humidity levels and phase transitions, used an interdigitated design. The parallel-plate capacitor was sensitive to pressure because of the variable gap between the (top and bottom layer) plates, and the interdigitated capacitor measured phase transitions through the change in electrical permittivity of the adjoining materials. The functionality of the interdigitated capacitor was extended to measure humidity by coating the capacitor with titanium dioxide, a material whose electrical permittivity changes in response to humidity. Both circuits used the same planar inductor geometry to complete the resonant circuit. The schematic drawings and physical structures of the circuits are shown in Figure 1.19.

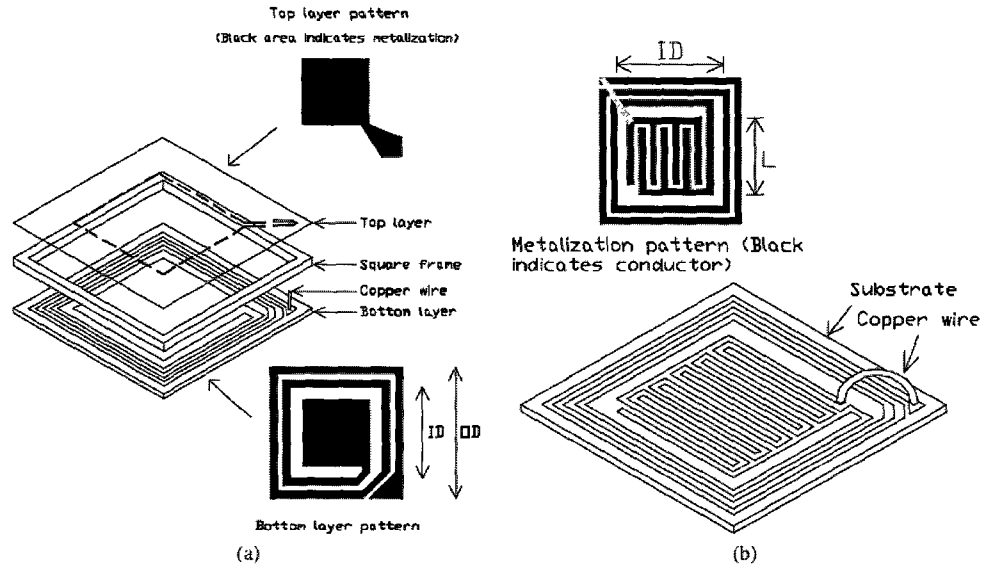
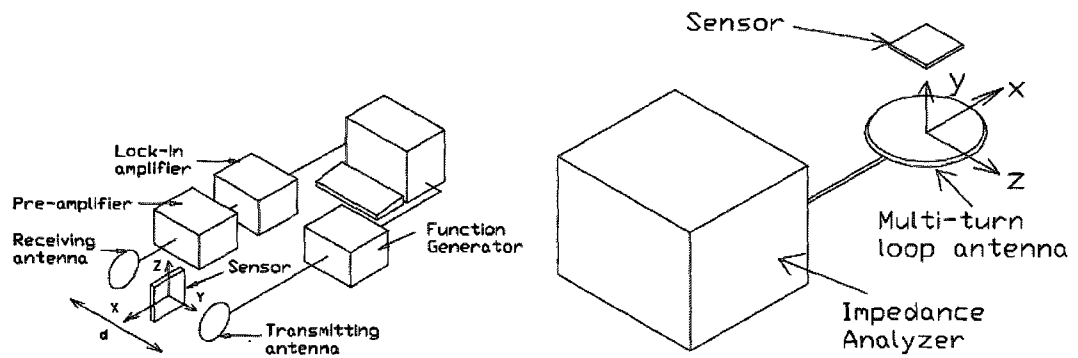


Figure 1.19 - a) Parallel plate capacitor resonant circuit, b) Interdigitated comb capacitor resonant circuit (8)

Two different methods were evaluated for interrogating the resonant circuit. The first method used a transmitting and receiving antenna, where the transmitting antenna received an electromagnetic wave from a function generator and the receiving antenna's output voltage was recorded using a lock-in amplifier. The second method used one loop whose impedance spectrum was monitored using an impedance analyzer. Figure 1.20 shows the physical set-up and their responses.



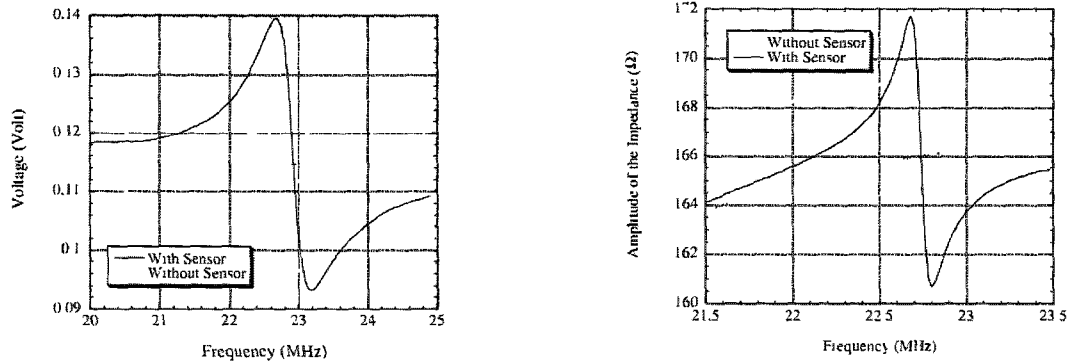


Figure 1.20 - Left: Two loop sensing system and response, Right: One loop sensing system and response

They used the two sensor loop method to perform their experimental evaluation of the pressure sensor, humidity sensor, and phase transition sensor. The pressure sensor had an undeformed resonant frequency of 22.5 MHz and was cycled between -3 psi to 4 psi; it produced a pressure sensitivity of  $670 \text{ kHz psi}^{-1}$ . The humidity sensor had a 2% humidity resonant frequency of 23.38 MHz and was cycled between 2% and 98% humidity; it yielded a shift of 800 KHz between low and high humidity levels. The phase transition sensor had an uncured epoxy resonant frequency of 20.25 MHz and was tested with 5-minute epoxy and 30-minute epoxy. The results from the 5 and 30 minute epoxy show first-order responses with the 30 minute having a longer rise time, but no quantitative sensitivity was reported.

Experiments were also performed, using the single-loop detection method, on how the number of turns for the probe loop affects the sensing distance. They determined for a  $4.2 \times 4.2 \text{ cm}^2$  sensor and 9.5 cm diameter loop antenna, the furthest distance for which the sensor was still detectable was 10 cm with 5 turns on the loop antenna. Investigation into the detection volume relative to the sensing loop was performed using a  $4.2 \times 4.2 \text{ cm}^2$  sensor and single, two turn, 6 cm diameter antenna. They determined for a detection volume of  $6 \times 6 \times 10 \text{ cm}^3$  (relative to the coordinate system in Figure 1.20)

and an orientation angle of less than 50 degrees from the antenna loop plane (from the x-axis towards the y-axis), an error of less than 70 kHz was observed.

They investigated the limitations of the two antenna detection method by changing the distance between the antennas and the location and orientation of the sensor. The antenna diameter was 5.5 cm and the sensor used was  $4.2 \times 4.2 \text{ cm}^2$ . They determined that for a test area of  $30 \times 18 \times 18 \text{ cm}^3$  and an orientation angle less than 60 degrees (measured from the x-axis towards the y-axis in Figure 1.20) an error of less than 100 kHz was observed. In general, they said “using larger sensors or larger antennas can increase the volume of space over which the sensor can be accurately monitored” (8).

### 1.4.5 Resonant Circuit for Strain Detection on a Planar Surface

Jia, Sun, Agosoto, and Quiñones designed and fabricated a thick-film, wireless, strain-sensitive resonant circuit, shown in Figure 1.21. This circuit is similar to the resonant circuit produced by Ong and Grimes, but instead of using the interdigitated capacitor to detect humidity or a material phase transition, Jia et al used the interdigitated capacitor to detect mechanical deformation (also known as strain). They experimentally validated the concept using a prototype resonant circuit and cantilever beam; it produced an unloaded resonant frequency of 11.525 MHz and a strain sensitivity of 0.964 (MHz/MHz)/mε. The fingers of the capacitor were orientated perpendicular to the direction of strain, which produced a better strain sensitivity.

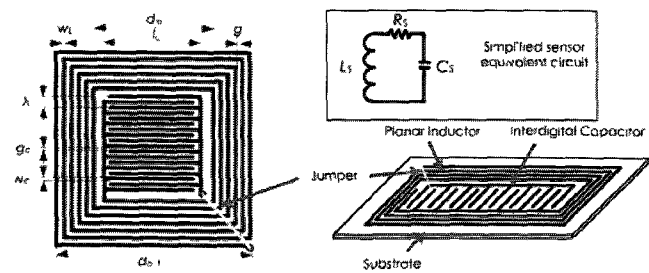


Figure 1.21 - Resonant circuit schematic and physical layout (5)

They analytically evaluated the Q-factor of the resonant circuit by including a discrete series resistor in their resonant circuit schematic ( $R_s$  in Figure 1.21). The value of the resistor was a summation of the series resistance of the interdigitated capacitor due to the skin effect and the resistance due to the turn-bend at each corner of the turn of the inductor. The total resistance was stated to be  $6.3293 \Omega$ .

Energy was provided to, and information was extracted from the resonant circuit through the use of a single loop interrogation system. The interrogation system consisted of a 20 MHz function generator, transistor current amplifier, single-loop antenna, and a signal processing circuit connected to a data acquisition board. They state that the maximum distance between the antenna and the resonant circuit from experimentation was 120 mm and the relative angle should be less than 75 degrees. They also proceed to state “generally speaking, noise may only change the magnitude of the measurement, not the frequency of the measurement” (5).

The resonant circuits we have discussed operated in the high-frequency regime (3-30 MHz) of the electromagnetic spectrum. The electromagnetic waves and amplitude information in this spectrum are able to be decoded by a simple envelope detector (diode and R-C circuit). As for our system, we experimentally determined that our strain sensitive resonant circuit resonates in the ultra-high frequency regime, primarily between 1 and 2 GHz. In this range, measurement and detection is more difficult. A system that is capable of measuring the parameters to characterize RF signals (e.g. reflection coefficient, scattering parameters, or gain and phase) is a RF vector network analyzer. These devices are extremely complex and highly sensitive, and therefore carry a large price tag (typically >\$20k).

#### **1.4.6 Integrated Circuit Fabricated Vector Network Analyzer**

Robert Lacoste of Alciom electronics wrote an application note (AN2090) for Cypress MicroSystems, detailing his design and fabrication procedure for a low-cost VNA using several integrated components and a Cypress programmable system on chip (PSoC) microcontroller. His design contained three major sub-systems: generator, receiver, and controller.

The generator portion of his system was responsible for producing the 0-1 GHz signal to be applied to the device under test. This signal was generated using two Mini-circuits surface mount voltage controlled oscillators, a mixer, two power splitters, and several filters. A more precise frequency could have been generated if frequency synthesizers were employed, although with this increase in precision comes complexity and cost (10).

The receiver circuit was responsible for two jobs: measuring the true input frequency and measuring the gain and phase of the device under test (DUT). The frequency measurement was performed by the PSoC, but a pre-scaler chip was required to reduce the RF input frequency to an acceptable range. The gain and phase measurement was accomplished by using a highly integrated circuit from Analog Devices, the AD8302. This circuit requires two inputs, one to serve as a reference signal and the other as a test signal. The AD8302 utilizes logarithmic amplifiers and arithmetic to yield two analog voltages representative of magnitude and phase, which are then read by the PSoC.

The previously mentioned sub-systems were controlled and interfaced to a computer via a Cypress MicroSystems CY8C26443 chip. This chip was responsible for



sending the control voltages for the two VCO's, measuring the true input frequency from the pre-scaler chip, measuring the magnitude and phase analogue voltages from the AD8302, and sending information and receiving commands to and from the host computer.

As with any VNA, a calibration routine was performed prior to operation to nullify the effects produced by board design and interconnects. A direct connection was attached between the output and input ports of the VNA, serving as a 'short' standard, which yielded the closed loop response of the system. The values from the closed loop response were used to correct the measured magnitude and phase measurements when a DUT was attached. The open-loop calibration was performed with two 'load' standards, one connected to the VNA output and one connected to the VNA input. The information from the open-loop calibration was used to determine the VNA's noise floor.

## CHAPTER 2

### PROBE CIRCUIT

This chapter is focused on variables that are specific to the probe circuit portion of the system. We begin with probe geometry, in which we experimentally evaluate different loop designs to determine the candidate with the best spectral characteristics. Then we look at theory regarding the inner diameter of the probe loop and coupling of the sensor loop, and its associated experimental results. Finally, we experimentally evaluate the impact of balancing the load with the source and the effect it has on the quality factor of the system resonance.

#### **2.1 PROBE GEOMETRY**

The purpose of this experiment was to evaluate how the shape of the probe loop affects the input impedance. We evaluated the magnitude and phase behavior of the probe loop with measurements acquired from an Agilent Technologies E5062A 75-ohm Vector Network Analyzer (VNA). The VNA measures input impedance as a function of frequency. We post-processed the data with Matlab to convert the complex input impedance into polar form (magnitude and phase).

The probe loops we investigated were fabricated using an LPKF S-62 circuit board plotter which produced circuit boards with 18  $\mu\text{m}$  thick and 0.83 mm wide copper traces on 1.27 mm thick FR-4. The probe loops we investigated were a 12.7 mm inner diameter circle, a 35.6 mm inner diameter circle, and a 39.6 mm square (Figure 2.1). The VNA was connected to the probe loops with a 50-ohm Type N to 50-ohm SMA adapter

and 50-ohm SMA end-launch connector. Figure 2.2 shows the 75 ohm VNA Type-N port, the adapter, and the connector.

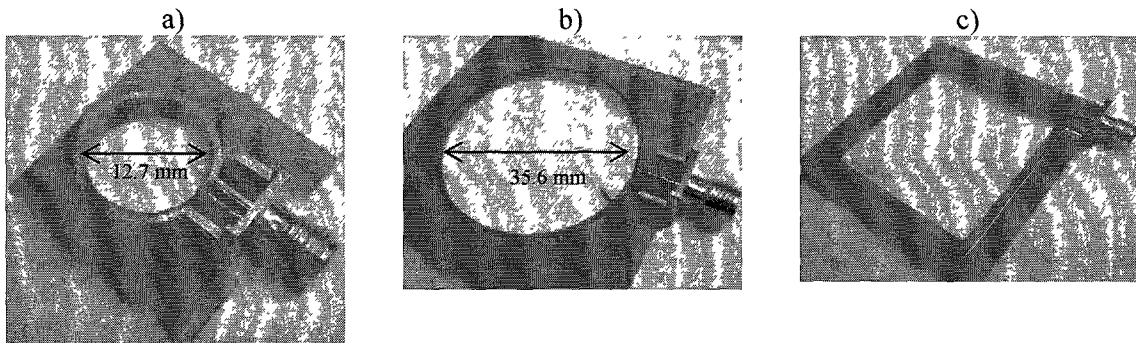


Figure 2.1 - Probe loops: 12.7 mm ID loop (a), 35.6 mm ID loop (b), 39.6 mm square (c)

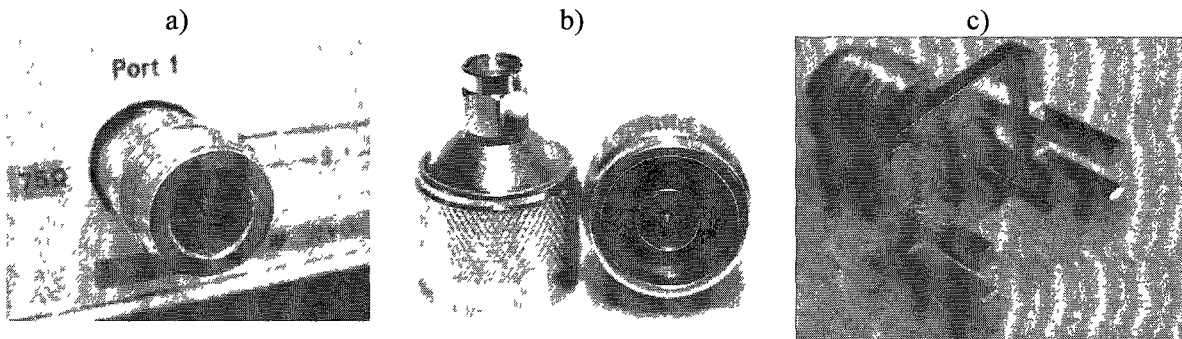


Figure 2.2 - Equipment: VNA 75 ohm Type-N port (a), 50 ohm Type-N to 50 ohm SMA adapter (b), 50 ohm SMB end launch connector (c)

Figure 2.3 shows the magnitude and phase response for the VNA without any attachments on the 75-ohm Type-N port (a), the VNA with the 50-ohm Type N to 50-ohm SMA adapter (b), and the VNA with the adapter and the 50-ohm SMA connector attached(c). From these plots, we see that the adapter alone produces a “self-resonance” at 2.1 GHz; the adapter and connector produce a self-resonance at 1.6 GHz.

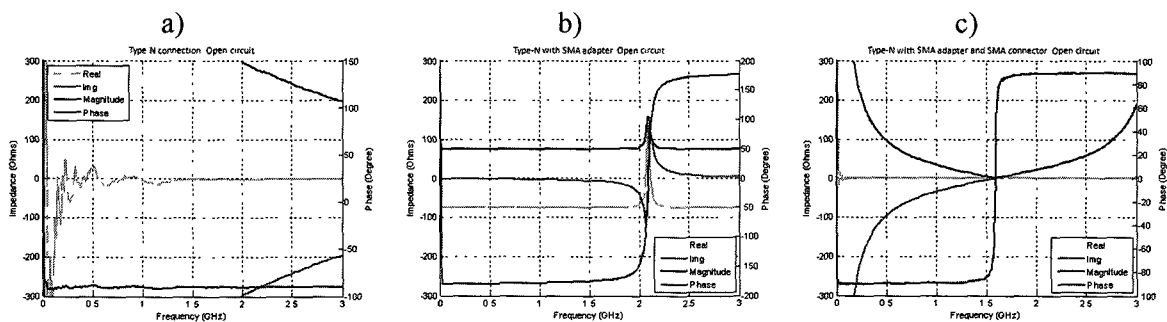


Figure 2.3 – Magnitude and phase response for the equipment shown in Figure 2

Figure 2.4 shows the input impedance magnitude and phase response for the probe loops pictured in Figure 2.1. Comparing these probe responses to Figure 2.3c, we see that the phenomena we previously referred to as the connectors “self-resonance” has shifted to a lower frequency for all cases. The 12.7 mm circular loop response shown in Figure 2.4a, does not produce a secondary resonance besides its self-resonance at 450 MHz. The 35.6 mm circular loop response shown in Figure 2.4b, produces two self-resonances, one at 250 MHz and the other at 2.2 GHz. The 39.6 mm square probe loop response shown in Figure 2.4c, produces three self-resonances which occur at 200 MHz, 1.7 GHz, and 2.75 GHz.

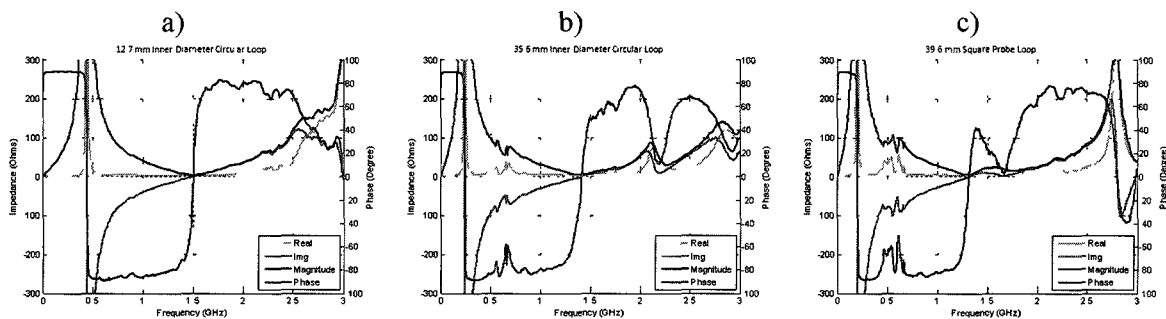


Figure 2.4 - Probe loop impedance response

The small circular loop pictured in Figure 2.1a is the probe loop we used to excite our sensor loops. The inner diameter of this probe loop provides close proximity to the sensor loop for good coupling; its spectral response between 1.6 GHz and 2.3 GHz is clear of any self-resonance. The lack of a self-resonance in this bandwidth means that the self-resonance won't mask the sensor loops resonance and the sensor loop resonance is thus easily detected error free.

## **2.2 PROBE DIAMETER**

The purpose of this section is to evaluate the impact of probe diameter on the quality factor of the resonance as well as the system resonant frequency. We know with two coplanar concentric loops, that increasing the inner loop radius will maximize the flux thus increasing the quality factor and coupling. We experimentally evaluated the response for three probe loops with varying inner diameters and compared the response to analytical approximations.

We used a solid copper cylinder for the insert material to represent a tool bit made of a low loss material. On the copper cylinder, we mounted a flexible circuit fabricated sensor loop with an interdigitated comb capacitor structure (ICCS). The ICCS design was horizontal to the axial direction of the cylinder with 11 fingers, 2.54 mm by 0.25 mm, with a separation distance of 0.25 mm, and via to sensor distance of 0.66 mm (see Figure 4.10). The vertical thickness of the band connected to the sensor was 1.27 mm. The capacitance of the ICCS, while mounted on the copper insert, was measured to be 0.856 pF using Analog Devices AD7746 capacitance to digital converter evaluation board. The same sensor loop configuration was interrogated with the various probe loops. The outer diameter of the sensor loop, not including the exterior insulation layer, was 13.15 mm. Figure 2.5 shows the sensor loop assembly.

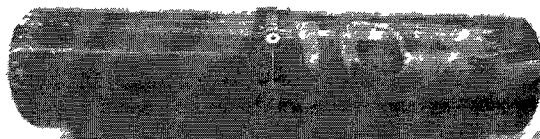


Figure 2.5 - Sensor mounted to copper cylinder

The probe loops were single turn loops with 0.83 mm wide copper traces, fabricated on 1.23 mm thick FR-4, with a terminal spacing of 0.46 mm. The inner

diameters of the loops were 14.53 mm, 15.09 mm, and 15.54 mm. These diameters were chosen because we observed a good resonance with our first prototype (14.53 mm) and then decided to investigate the probe dependence by increasing the radius by 0.254 mm. The probes were connected to the VNA with a 75-ohm mini-SMB end launch connector. Figure 2.6 shows the probe loops and their connectors.

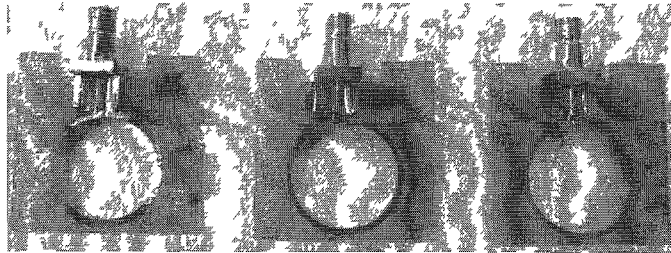


Figure 2.6 – Probe loops (left to right): 14.53 mm, 15.09 mm, and 15.54 mm

The experimental set-up consisted of a vertical and horizontal translation stage mounted to a vertical post fixed to a bread board. Attached to the horizontal translation stage was a 12.7 mm inner diameter polycarbonate mounting platform for holding the copper cylinder. Figure 2.7 shows the experimental set-up and a close-up image of the sensor/probe configuration.



Figure 2.7 - Experimental set up and close-up picture of probe/sensor loop

### **2.2.1 Theoretical Estimation**

Figure 2.8 provides a CAD model of the circuit schematic in Figure 2.9.

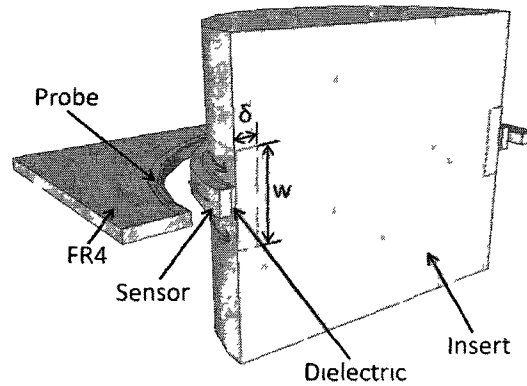


Figure 2.8 - Cross-sectional view of probe, sensor, and insert

In Figure 2.8,  $\delta$  is the skin depth,  $w$  is the width of the surface currents induced in the insert, the probe's red arrow is the current driven by the generator, the sensor's red arrow is the induced current due to the probe, and the red arrows on the insert are the induced eddy/surface currents due to the probe and sensor. The circuit representation for the probe, sensor, and insert components is shown in Figure 2.9

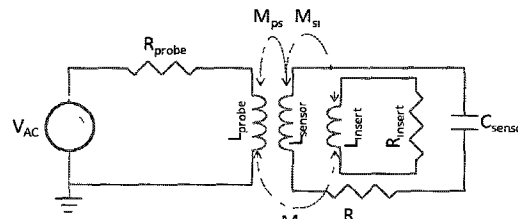


Figure 2.9 - Circuit representation illustrating the lumped components of the system

where  $R_{probe}$  is the resistance of the probe loop,  $R_{sensor}$  is the resistance of the sensor loop,  $R_{insert}$  is the resistance of the insert material due to eddy currents,  $L_{probe}$  is the inductance of the probe loop,  $L_{sensor}$  is the inductance of the sensor loop,  $L_{insert}$  is the inductance of the insert material due to eddy currents,  $C_{sensor}$  is the capacitance of the sensor,  $M_{ps}$  is the mutual inductance between the probe and sensor,  $M_{si}$  is the mutual inductance between the sensor and insert, and  $M_{pi}$  is the mutual inductance between the probe and insert. While the probe and sensor inductances can be estimated from their geometrical properties and the capacitance was physically measured, the resistance and insert

inductance are estimated for a frequency range (1.75 to 1.81 GHz) because of their dependence on skin depth.

The sensor and probe inductances were estimated based on their geometrical properties using

$$L = \mu_0 R_{loop} \left( \ln \left( \frac{R_{loop}}{r} \right) - 2 \right) \quad (2.1)$$

where  $L$  is the inductance,  $\mu_0$  is the permeability of free space,  $r$  is the radius of the wire, and  $R_{loop}$  is the radius of the loop (11). The sensor loop self inductance is independent of the probe loop and is calculated to be 32 nH, the self inductance of the various probe loops are listed in Table 2-1. The mutual inductance formed between the probe loop and sensor loop can be estimated with

$$M = \mu_0 \sqrt{r_{sensor} r_{probe}} \left[ \left( \frac{2}{k} - k \right) K(k) - \frac{2}{k} E(k) \right] \quad (2.2)$$

where

$$k = \frac{4 * r_{sensor} r_{probe}}{\sqrt{(r_{sensor} + r_{probe})^2 + d^2}} \quad (2.3)$$

and  $M$  is the mutual inductance,  $r_{sensor}$  is the sensor loop radius,  $r_{probe}$  is the probe loop radius,  $d$  is the separation distance between the loops, and  $K(k)$  and  $E(k)$  are the complete elliptic integrals of the first and second kind, respectively (11). The mutual inductance values for the probe loop and sensor loop calculated using Equations 2.1, 2.2, and 2.3 are listed in Table 2-1.

<b>Probe Diameter (mm)</b>	<b>Probe Self Inductance (nH)</b>	<b>Mutual Inductance (nH)</b>
14.53	46.3	19.6
15.09	48.3	17.8
15.54	50.0	16.7

Table 2-1 - Values for the probe self inductance and mutual inductance

The inductance of the insert material is a function of skin depth. The skin depth, also known as the depth of penetration of the electromagnetic waves, can be determined from



$$\delta = \sqrt{\frac{2}{\omega\mu\sigma}} \quad (2.4)$$

where  $\delta$  is the skin depth,  $\omega$  is the angular frequency,  $\mu$  is the permeability, and  $\sigma$  is the conductivity (11). Figure 2.10 shows a plot of the skin depth versus frequency.

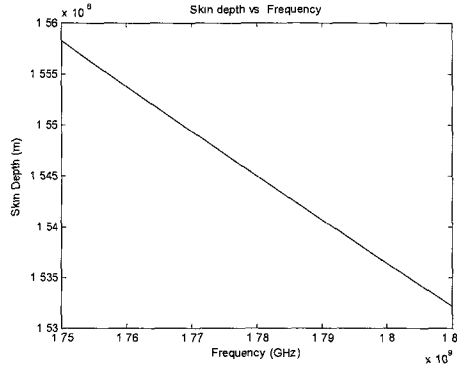


Figure 2.10 - Skin depth as a function of frequency

If we assume a uniform current distribution throughout the sensor cross-section, Figure 2.11 can be used to determine the width ( $w$  in Figure 2.8) of the induced currents on the insert material.

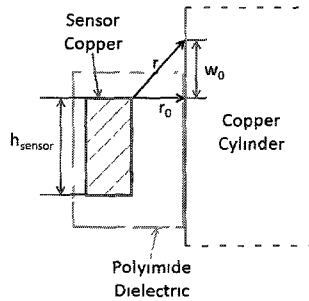


Figure 2.11 - Sensor/insert cross-section

The relation to calculate the vertical height of the induced currents on the insert is

$$w_0 = H_{max}e^{-1} \quad (2.5)$$

where  $w_0$  is the vertical height above the sensor band and  $H_{max}$  is the magnetic field maximum (see Appendix: Chamberlin, Kent). Given  $H_{max}$  equal to 1, we can rewrite Equation 2.5 in terms of the parameters from Figure 2.11

$$r = \frac{r_0}{e^{-1}} \quad (2.6)$$

where  $r_0$  is the distance from the sensor to the insert and  $r$  is the distance to the location where the induced currents in the insert are negligible. Using Pythagoreans theorem and solving for  $w_0$ , the total width ( $w$  in Figure 2.8) can then be calculated from

$$w = h_{sensor} + 2 * w_0 \quad (2.7)$$

where  $h_{sensor}$  is the vertical height of the sensor. The total width was calculated to be 2.3 mm.

Assuming a shorted copper loop based on the thickness of the skin depth and width ( $w$  from Equation 1.9), the inductance of the insert material can be calculated using Equation 2.1. Figure 2.12 shows the insert material inductance as a function of frequency.

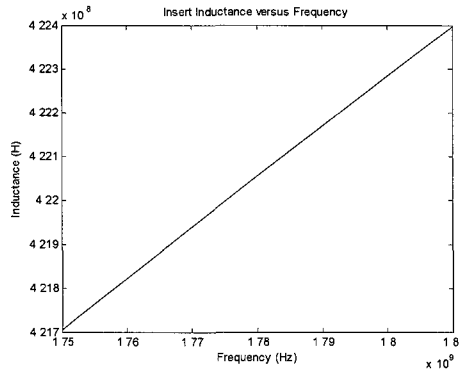


Figure 2.12 - Copper insert inductance as a function of frequency

Assuming for the sensor and insert total inductance that the inductance's add in parallel and that  $M_{ps}$  has a much greater influence than  $M_{pi}$  and  $M_{si}$ , and assuming that the wireless inductive coupling can be represented as a parallel configuration with opposing probe and sensor inductors, the total inductance can be calculated

$$L_{total} = \frac{L_{sensor/insert}L_{probe} - M_{ps}^2}{L_{sensor/insert} + L_{probe} + 2M_{ps}} \quad (2.8)$$

where  $L_{total}$  is the equivalent inductance,  $L_{sensor/insert}$  is the sensor/insert parallel inductance, and  $L_{probe}$  is the probe inductance (12). The equivalent inductance is shown in Figure 2.13.

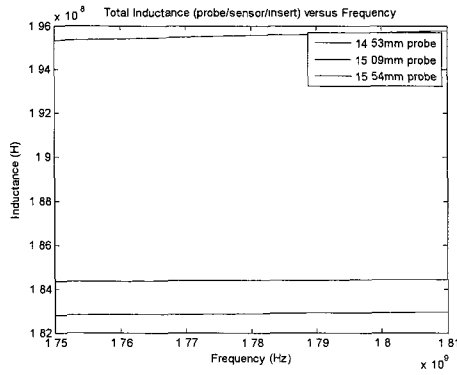


Figure 2.13 - Total system inductance as a function of frequency

The resistance due to the skin depth for the probe, sensor and copper insert can also be calculated from

$$R = \frac{\rho l}{w\delta(1 - e^{-h/\delta})} \quad (2.9)$$

where  $\rho$  is the resistivity of the material,  $l$  is the length,  $w$  is the width, and  $h$  is the height (7). Figure 2.14 shows the width and height of the probe, sensor, and inductor used for calculation in Equation 2.10.

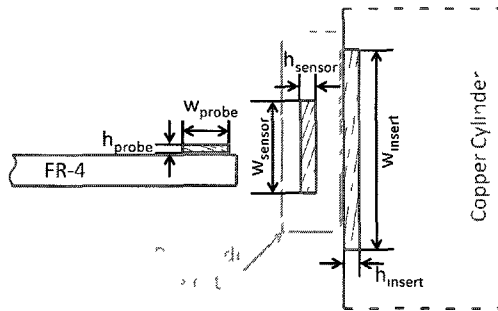


Figure 2.14 - Geometrical variables for probe, sensor, and insert (cross-section view)

Figure 2.15 shows the probe loop resistance as a function of frequency.

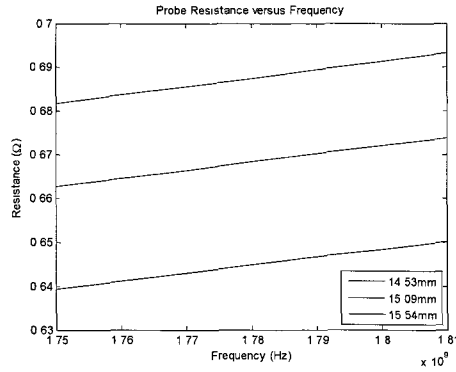


Figure 2.15 - Probe loop resistance versus frequency using Equation 1.11

Figure 2.16 shows the sensor loop and insert material's resistance as a function of frequency.

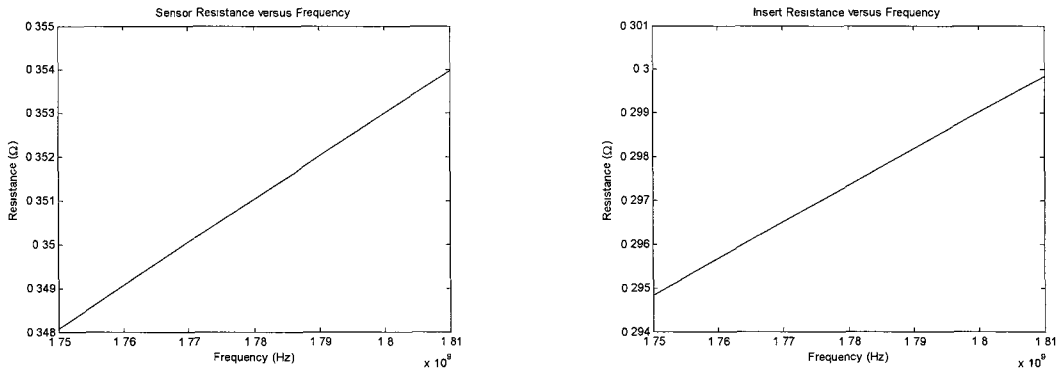


Figure 2.16 - Left: Sensor loop resistance versus frequency; Right: Insert material resistance versus frequency

Assuming these resistances can be lumped together in a serial fashion, Figure 2.17 shows the total system resistance.

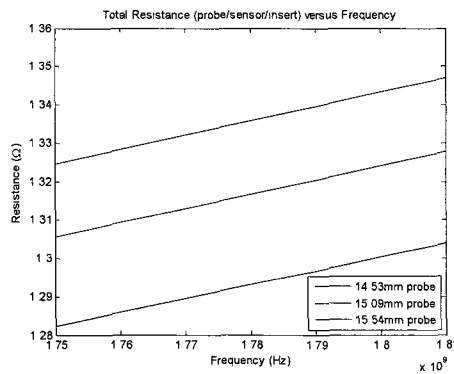


Figure 2.17 - Total system resistance as a function of frequency

## 2.2.2 Experimental Results

Figure 2.18 shows the impedance and phase response for the 14.53 mm diameter probe loop and the sensor loop mounted to a copper cylinder.

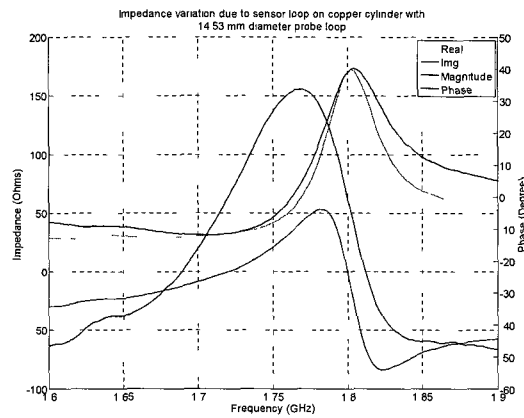


Figure 2.18 - 14.53 mm ID probe loop and sensor loop mounted on copper cylinder response

Figure 2.19 shows the impedance and phase response for the 15.09 mm diameter probe loop and the sensor loop mounted to a copper cylinder.

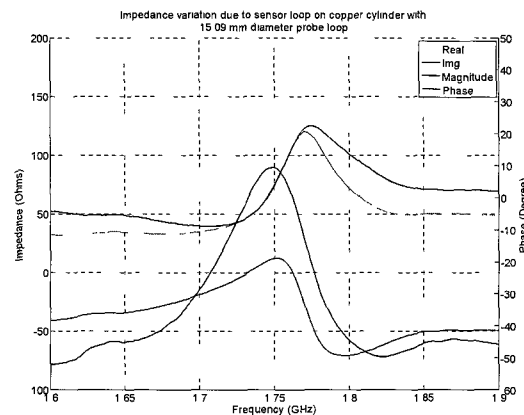


Figure 2.19 - 15.09 mm ID probe loop and sensor loop mounted on copper cylinder response

Figure 2.20 shows the impedance and phase response for the 15.54 mm diameter probe loop and the sensor loop mounted to a copper cylinder.

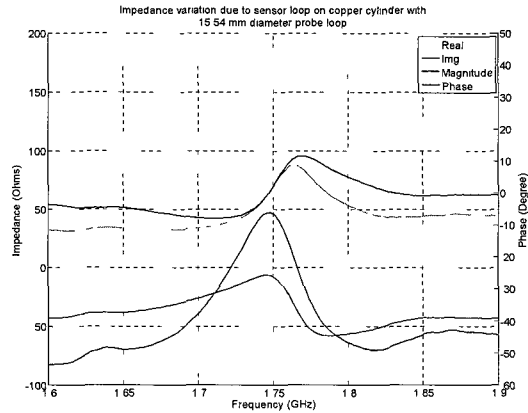


Figure 2.20 - 15.54 mm ID probe loop and sensor loop mounted on copper cylinder response

Table 2-2 displays the resonant frequencies and Q-factors for Figure 2.18 through Figure 2.20.

Probe Diameter (mm)	Resonant Frequency (GHz)	Q-factor
14.53	1.802	54.9
15.09	1.770	47.2
15.54	1.764	40.9

Table 2-2 – Experimentally derived resonance parameters

We can make two observations from these results. First, the inductance must increase as the probe diameter increases because there is a decrease in the resonant frequency, which is consistent with the analytical formulas. Second, the Q-factor decreases as the probe diameter increases which results in a more smoothed resonant peak. Assuming a resonant circuit in the form of Figure 2.21 and given the measurement of the ICCS capacitance, we can estimate the value of inductance and resistance from the resonant frequency and Q-factor, respectively.

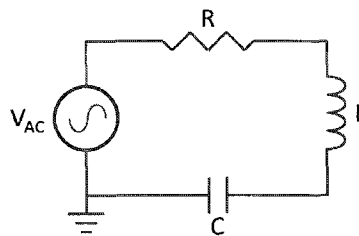


Figure 2.21 - Simplified resonant circuit

The resonant frequency relation used for calculating the inductance is shown in Equation 1.2. The Q-factor equation used to calculate the resistance is

$$Q = \frac{1}{R} \sqrt{\frac{L}{C}} \quad (2.10)$$

where Q is the quality factor, L is the inductance, C is the capacitance, and R is the resistance (13). Table 2-3 shows the empirically derived values of the inductor and resistor for Figure 2.21. The estimated values of inductance and resistance are within an order of magnitude of the experimentally derived values.

Probe Diameter (mm)	Inductance (nH)	Resistance ( $\Omega$ )
14.53	9.11	1.88
15.09	9.62	2.25
15.54	9.71	2.60

Table 2-3 – Component values for the simplified schematic

In conclusion, the probe loop should be as close as possible to the sensor loop to produce the highest Q-factor. The probe diameter will be chosen based on the eccentricity and displacement due to strain in the tool bit during the machining process.

### **2.3 LOAD BALANCING**

The purpose of this experiment was to evaluate if adding resistance to the load circuit increases the quality factor of the resonance. This was investigated because maximum power transfer occurs when the load impedance is the complex conjugate of the source impedance (2). At resonance, the reactance of the inductor and capacitor cancel resulting in a short circuit condition. The hypothesis is that the 75  $\Omega$  resistive load will provide the impedance match for the source, thus delivering maximum power to the circuit. The four designs we investigated were a no resistance case, a 75  $\Omega$  resistor in between the probe loop and the ground terminal, a 75  $\Omega$  resistor in between the

subminiature type B (SMB) input and the probe loop terminal, and a  $36\ \Omega$  resistor in between the SMB input and the probe loop and a  $36\ \Omega$  resistor in between the probe loop and ground terminal. Figure 2.22 shows the electrical schematics for the VNA and the probe loops mentioned above (note that Agilent E5062A VNA was used for measurement, therefore  $R_{\text{source}}$  is  $75\ \Omega$ ).

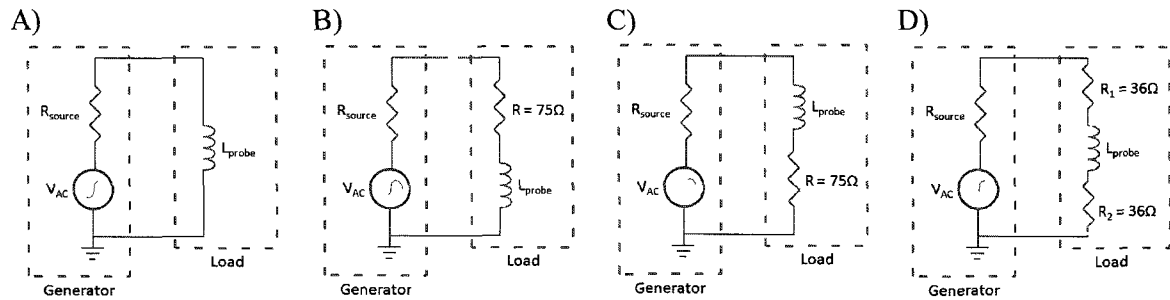


Figure 2.22 –Loop Electrical Schematics: A) No resistance, B)  $75\ \Omega$  on input terminal, C)  $75\ \Omega$  on ground terminal, and D)  $36\ \Omega$  on input and ground terminals

The probe loop was printed on FR-4 with an inner diameter of 14.5 mm, a trace width of 0.81 mm, and terminal spacing of 0.46 mm. The probe loop was connected to the VNA with a mini-SMB 75-ohm end launch connector. To allow room for the surface mount resistors the connector was displaced from the loop by 3.25 mm. Figure 2.23 shows images of the actual probe loops.



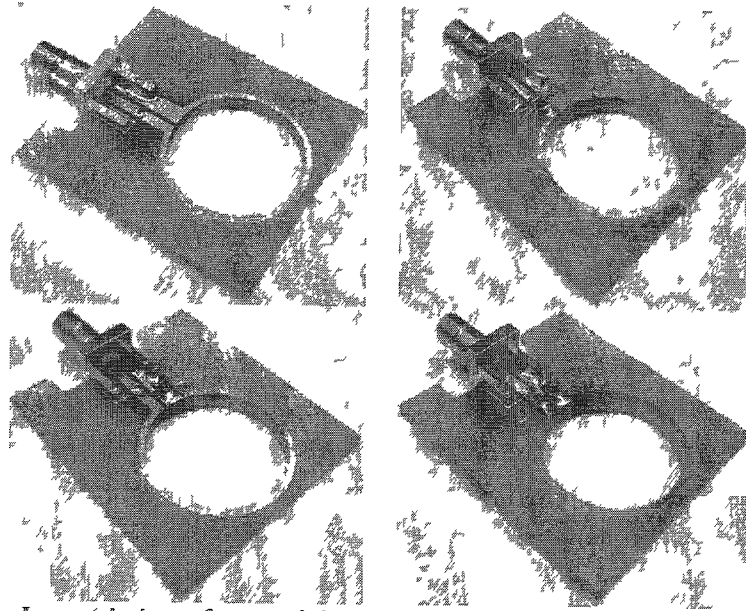


Figure 2.23 - Probe Loops (clockwise from top left): no resistance, 75  $\Omega$  on input terminal, 36  $\Omega$  on input and ground terminals, and 75  $\Omega$  on ground terminal

All of the probe loops interrogated the same sensor loop assembly. The sensor loop was composed of an interdigitated comb capacitor structure (ICCS) and non-insulated 30 AWG wire. The ICCS design was horizontally oriented to the tool axis with 11 fingers, 1.27 mm long and a separation distance of 0.13 mm. The ICCS was adhered directly to the tool bit with cyanoacrylate. The 30 AWG wire was soldered to the vias of the ICCS and displaced from the tool bit by 177  $\mu\text{m}$  of polyimide insulation (Dupont Kapton tape). The sensor loop was mounted on a two flute carbide end mill. Figure 2.24 shows a picture of the sensor loop and tool bit, the sensor loop to the left was used for this experiment.

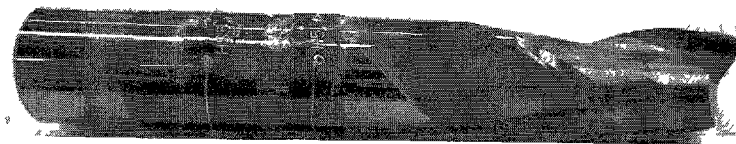


Figure 2.24 - Sensor loop and tool bit

Although the addition of the resistance will satisfy the impedance match criterion, it may reduce the quality factor because we are increasing the series resistance with the inductor. The quality factor of an inductor is given in the relation

$$Q = \frac{\omega L}{R} \tag{2.11}$$

where  $\omega$  is the angular frequency, L is the inductance, and R is the internal resistance.

Figure 2.25 shows the impedance and phase response for the no resistance probe loop and sensor loop.

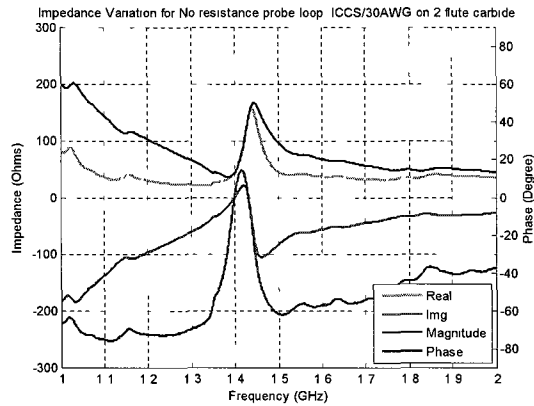


Figure 2.25 – Response for no resistance probe loop

Figure 2.26 shows the impedance and phase response for the probe loop with the 75  $\Omega$  resistor on the ground terminal and sensor loop.

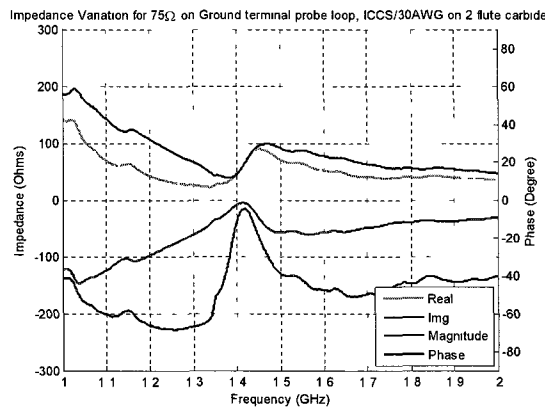


Figure 2.26 – Response for 75  $\Omega$  on input terminal probe loop

Figure 2.27 shows the impedance and phase response for the probe loop with the 75  $\Omega$  resistor on the input terminal and sensor loop.

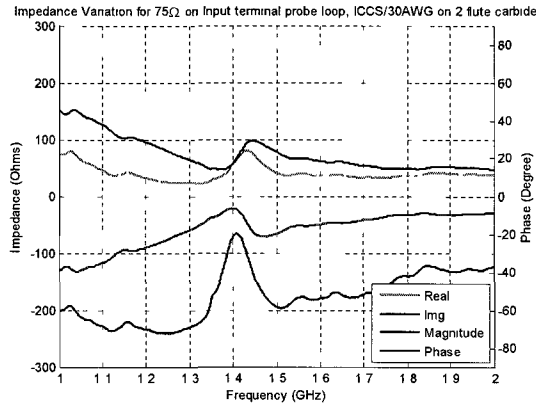


Figure 2.27 - Response for 75 Ω on ground terminal probe loop

Figure 2.28 shows the impedance and phase response for the probe loop with the 36 Ω resistors on the input and output terminal and sensor loop.

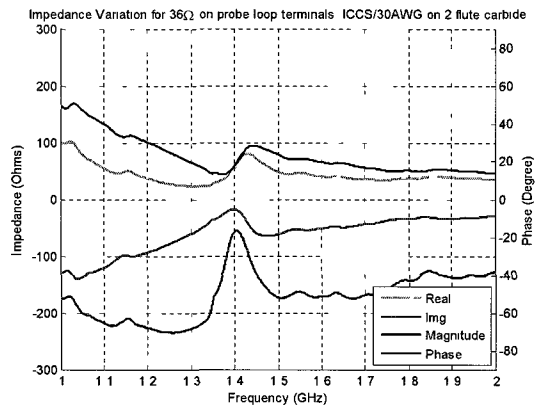


Figure 2.28 - Response for 36 Ω on input and ground terminals probe loop

Table 2-4 displays the quality factors calculated from Figure 2.25 through Figure 2.28.

Description	Quality Factor
No Resistance	27.8
75-ohm on Ground Terminal	6.1
75-ohm on Input Terminal	13.0
36-ohm on Input and Ground Terminals	7.9

Table 2-4 – Quality factors for probe loop with varying resistive impedance

In conclusion, the system resonance has the highest Q-factor when the probe loop does not contain any resistance. The power delivered to the load is at a maximum due to the impedance match, but the quality factor is degraded because of the increase in probe resistance.

## **2.4 CHAPTER SUMMARY**

In this chapter, we experimentally determined that a 12.7 mm inner diameter circular probe loop yielded a spectral response clear of self-resonance's in the frequency spectrum of interest.

We analytically determined and experimentally verified that our resonant system achieved the highest quality factor when the probe loop is in close proximity to the sensor loop. From our experiments, the probe loop achieved the highest quality factor of 54.9 with a sensor loop to probe loop separation distance of 0.69 mm.

Finally, we experimentally determined that the quality factor of the system resonance was reduced with the addition of a resistive element to the probe loop circuit. The highest quality factor of 27.8 was observed when the probe loop circuit's resistance was due only to skin effect of the copper trace.

## CHAPTER 3

### SENSOR LOOP

This chapter is focused on variables that are specific to the sensor loop. We begin with sensor capacitance, in which we experimentally evaluate discrete capacitors and parallel plate overlap capacitors at the sensor loop junction. Next, we look at different insert materials in which we experimentally evaluate how they impact the quality factor of the system resonance. Then through experimental observations we assess the dielectric stand-off distance and how it impacts the resonances quality factor. Finally, we experimentally evaluate sensor loop location to determine how it affects the resonant frequency.

#### **3.1 SENSOR CAPACITANCE**

The purpose of this experiment was to determine the system resonant frequency sensitivity to variations in the sensor loop capacitance. The sensor loop capacitance was varied by placing different valued capacitors at the termination of the sensor loop.

##### **3.1.1 Discrete Capacitors**

The sensor loops were mounted on a 3 flute carbide tool bit with a polyimide stand-off distance of 80  $\mu\text{m}$ . The ceramic capacitors were of nominal capacitance ranging from 0.1 to 0.9 pF in increments of 100 fF as well as a 1.5 pF capacitor, and were placed at the termination of a 30 AWG wire. The physical size was 1 mm by 0.5 mm, and they were attached to the polyimide with cyanoacrylate. Figure 3.1 shows the sensor loops mounted to a 3-flute carbide end mill tool bit, the sensor loop with the larger

conductor was not used in this experiment. All measurements were performed with the capacitor directly opposite the probe loop input terminals.

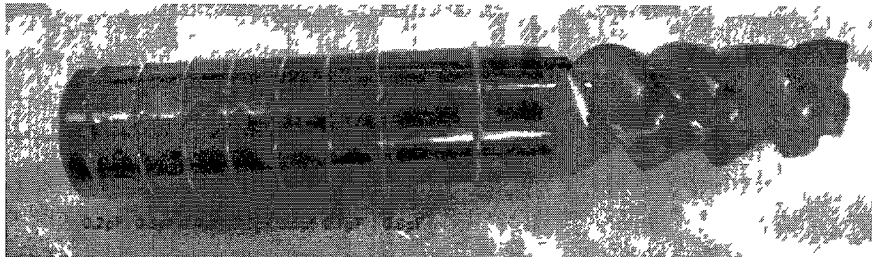


Figure 3.1 - Tool bit with sensor loops with varying capacitance

The probe loop we used to excite the sensor loop was a 14.1 mm inner diameter single turn loop with a trace width of 0.82 mm printed on FR-4. The connection to the loop was made with a 50-ohm SMA end launch connector with a connection terminal spacing of 2.16 mm. Figure 3.2 shows the probe loop and connector.

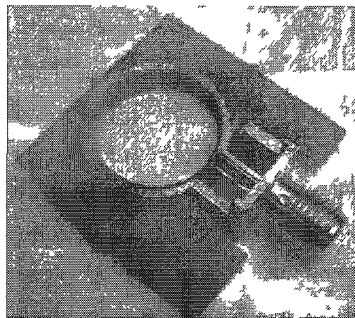


Figure 3.2 - Probe loop used to excite the 0.1 to 1.5 pF sensor loops

Figure 3.3 shows a tool bit placed inside the probe loop on an aluminum platform attached to a vertical translation stage fixed to a vertical post on an optical breadboard. This experimental setup allowed us to evaluate multiple loops without having to physically touch the specimen.



Figure 3.3 - Photo of experimental set-up

Figure 3.4 shows the impedance and phase dependence for the SMA connector with the probe loop connected to the VNA. Figure 3.5 shows the impedance and phase behavior for the 0.2 pF sensor loop positioned inside the probe loop connected to the VNA.

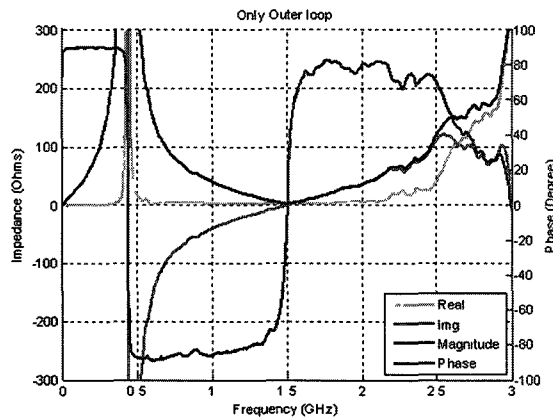


Figure 3.4 - System response for probe loop

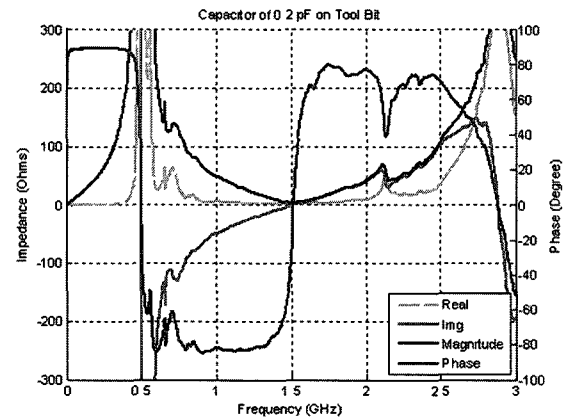


Figure 3.5 - System response for 0.2 pF sensor loop

We also tested a sensor loop with a 1.54 mm by 3.19 mm 11.55 pF ceramic capacitor with a pyralux sensor loop with two layers of 0.063 mm thick Kapton tape connected to the capacitor with 30 AWG wire. There was not enough clearance for this sensor loop to pass through the probe loop, therefore the capacitor was placed in the

keyed area of the tool bit. Figure 3.6 shows a close up picture of the solder connections of the capacitor as well as a picture of the sensor loop.

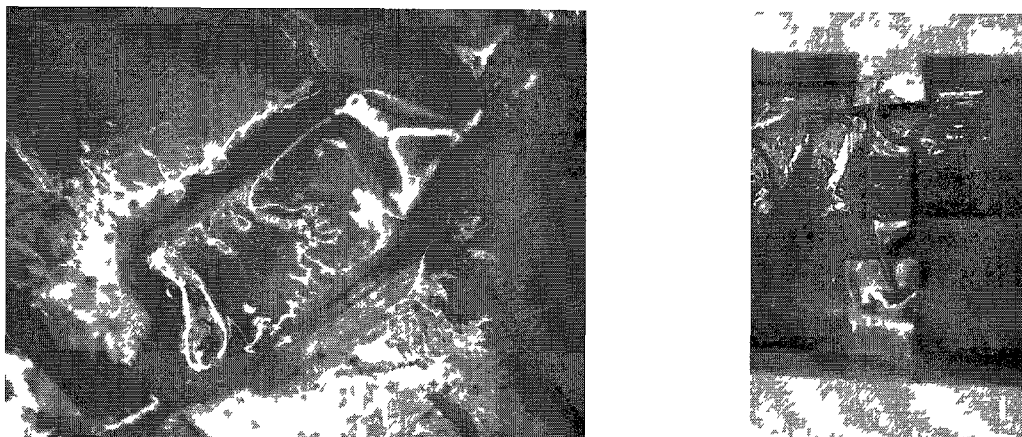


Figure 3.6 - Close up of 11.55 pF solder connections and sensor loop

The probe loop used to excite this sensor loop was of the same physical dimensions as the one shown in Figure 3.2. The only differences were the connector, which was a 75-ohm mini-SMB end launch connector, and the terminal spacing, which was 0.41 mm. Figure 3.7 shows the probe loop and connector attached to the Vector Network Analyzer and the experimental set up with the sensor loop inside the probe loop.

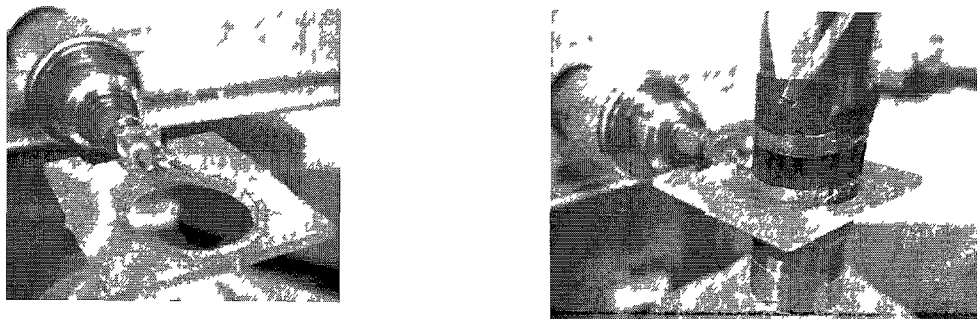


Figure 3.7 - SMB connector/ probe loop and experimental set-up

Figure 3.8 shows the impedance and phase dependence for the SMB probe loop connected to the VNA. Comparing Figure 3.4 to Figure 3.8, we see that the first resonance has shifted from approximately 400 MHz to 700 MHz and the second resonance at 1.5 GHz has been removed. The 1.5 GHz can therefore be attributed to the 75-ohm source and 50-ohm load impedance mismatch due to the connector and adapter.



Figure 3.9 shows the impedance and phase behavior for the 11.55 pF sensor loop positioned inside the SMB probe loop connected to the VNA.

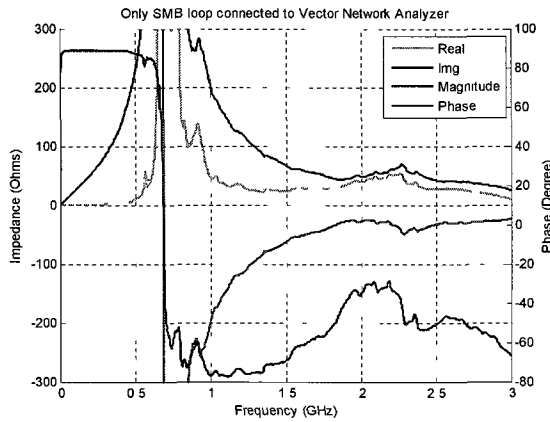


Figure 3.8 - System response due to only SMB loop

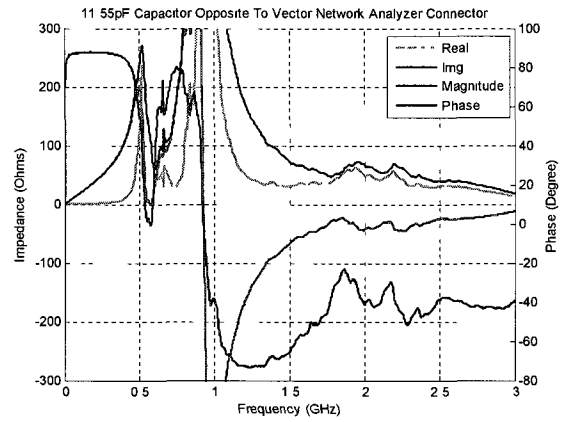


Figure 3.9 - System response for 11.55 pF sensor loop

Table 3-1 shows the resonant frequency information determined from the sensor loops with discrete valued capacitors.

Capacitance (pF)	Resonant Frequency (GHz)
0.1	2.3
0.2	2.1
0.3	1.95
0.4	1.88
0.5	1.79
0.6	1.65
0.7	1.59
0.8	1.53
0.9	1.39
1.5	1.18
11.55	0.5

Table 3-1 - Capacitance and resonant frequency information from discrete capacitors

### **3.1.2 Parallel Plate Capacitors**

Another form of capacitor we investigated was a parallel-plate capacitor. It was produced by overlapping the ends of the Pyralux material and bonding them together with cyanoacrylate. The polyimide backing of the Pyralux served as the dielectric material for the capacitor. Figure 3.10 shows a 3-D CAD model of the overlap capacitor sensor loop, and Figure 3.11 shows three physical loops mounted on a drill bit.

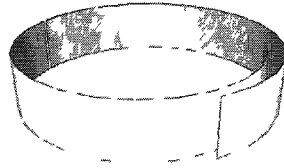


Figure 3.10 - Sensor loop with parallel plate capacitor

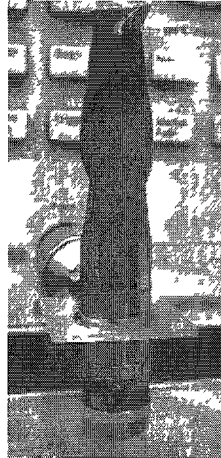


Figure 3.11 - Tool bit with three overlap-type sensor loops, only one of which is being monitored externally

The probe loop we used to excite these sensor loops was the same one shown in Figure 3.2, which utilized a SMA connector.

We did not directly measure the capacitance of the overlapped area and estimated the capacitance using the formula for a parallel plate capacitor shown in Equation 1.3. The thickness of the polyimide dielectric for the Dupont Pyralux LF9120R has a manufacturing tolerance of  $\pm 10\%$  and the relative permittivity of the cyanoacrylate was not known. The capacitances of these sensors were estimated to be 1.73, 1.97, 2.47, 3.07, 3.39, 5.84, and 5.89 pF. Figure 3.12 shows the capacitance estimation variation due to the manufacturing tolerance of the Pyralux. Figure 3.13 shows the capacitance estimation variation due to a  $\pm 5\%$  variation in the relative permittivity of the dielectric.

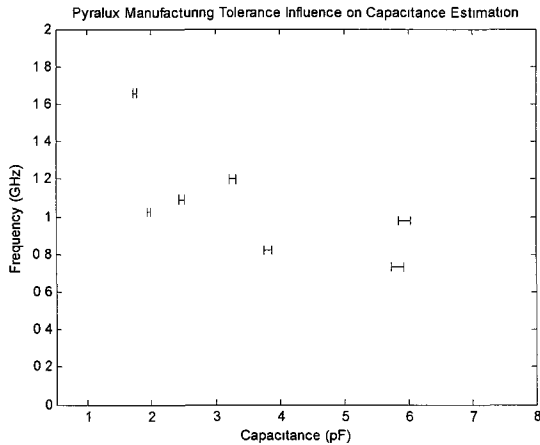


Figure 3.12 - Simulated capacitance variation due to manufacturing tolerance using equation 1.3

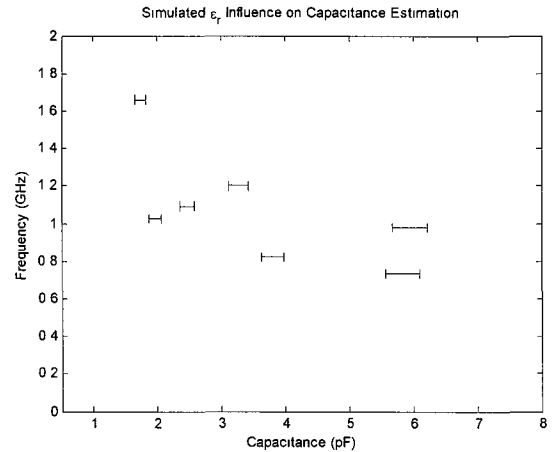


Figure 3.13 - Simulation for variation in relative permittivity using equation 1.3

Figure 3.14 shows the impedance and phase behavior for the 1.968 pF sensor loop positioned inside the probe loop connected to the VNA, this figure has a narrowed frequency range in order to focus only on the resonance caused by the sensor loop. Figure 3.15 shows the impedance and phase behavior for the 5.89 pF sensor loop positioned inside the probe loop connected to the VNA.

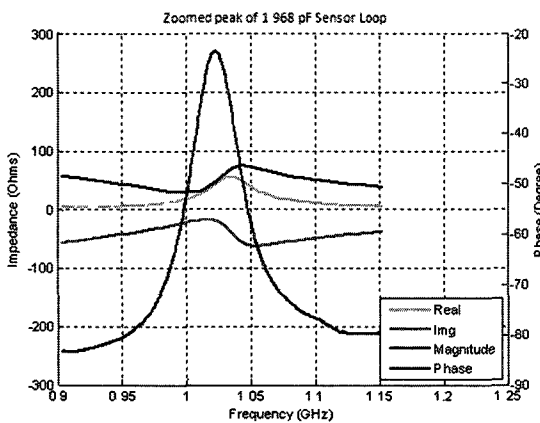


Figure 3.14 - System response due to 1.968 pF sensor loop with narrowed frequency range

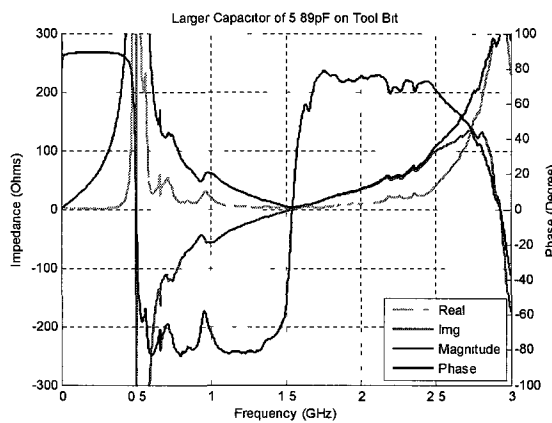


Figure 3.15 - System response for 5.89 pF sensor loop

Table 3-2 shows the resonant frequency information extracted from the different valued overlapping capacitors.

Capacitance (pF)	Resonant Frequency (GHz)
1.73	1.66
1.97	1.027
2.47	1.092
3.07	0.821
3.39	1.2
5.84	0.734
5.89	0.98

Table 3-2 - Capacitance and Resonant frequency information from overlap capacitor sensor loops

Figure 3.16 shows the dependence of the resonant frequency versus capacitance information from Table 3-1 and Table 3-2. The equation of the power law in Figure 3.16 is

$$f = 1.3805 * C^{-0.294} \quad (3.1)$$

where C is the value of capacitance and f is the frequency.

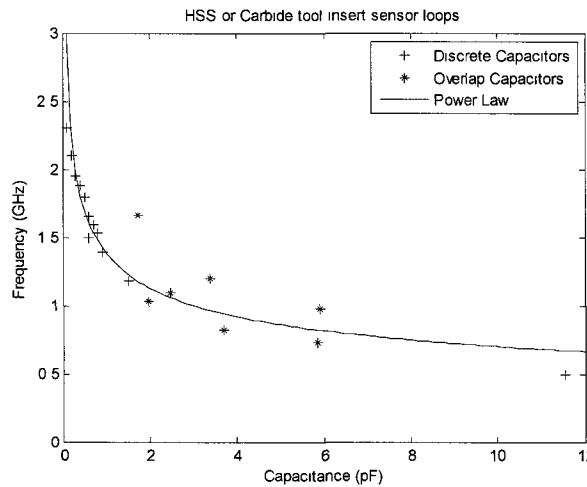


Figure 3.16 - Resonant frequency vs. sensor loop capacitance

While this plot shows a general power-law trend, the data was obtained using different sensor loops for the higher capacitance data and different connectors. While the connector is not likely to shift the frequencies, the inductance of the loop could be much different.

From these measurements and provided that the frequency is directly proportional to strain, we are able to state that a strain detection system with a lower sensor capacitance will produce a greater frequency change and thus a greater strain sensitivity.

### **3.2 INSERT MATERIAL**

The purpose of this experiment was to determine the effect of insert material on the quality of system resonance. The quality of resonance was evaluated for identical sensor loops mounted on an insulator (polycarbonate), and three conductors with different conductivity: copper, steel, and cemented carbide.

The sensor design was a horizontally orientated interdigitated comb capacitor, which consisted of a total of 11 fingers, 127  $\mu\text{m}$  by 2.54 mm, and a finger spacing of 127  $\mu\text{m}$ . The outer band vertical thickness for the sensor loop was 1.27 mm. Figure 3.17 shows a picture of the actual horizontal capacitor.

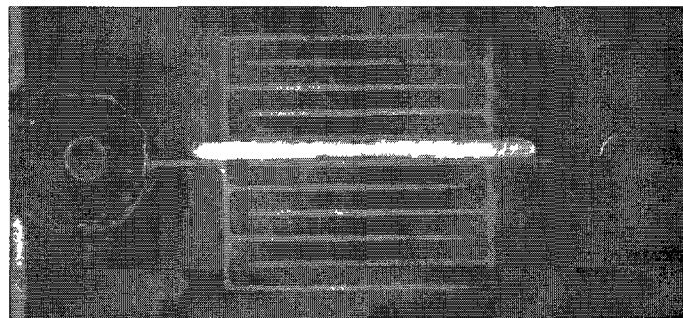


Figure 3.17 - Interdigitated capacitor and vias

The probe loop used to excite the sensor loop was an 18  $\mu\text{m}$  thick 14.35 mm inner diameter loop printed on FR-4 with a trace width of 0.81 mm connected to the 75-ohm vector network analyzer with a 75-ohm mini-SMB end launch.

We investigated four different insert materials: polycarbonate (non-magnetic material), copper (diamagnetic material), high strength steel, and cemented carbide (ferromagnetic materials). A system with a good Q-factor makes resonance detection

easier and more reliable. We expect different insert materials with lower conductivity to decrease the quality (Q) factor of the resonance because of power loss in the form of eddy currents. The relation of power loss to insert material resistance is

$$P_{eddy} = i_{eddy}^2 R_{core} \quad (3.2)$$

where  $i_{eddy}$  is the value of the eddy current induced in the core,  $R_{core}$  is the resistance of the core material, and  $P_{eddy}$  is the power loss due to the eddy current (14).

We choose polycarbonate as a control because this material is an insulator and has extremely high resistance which would not allow an eddy current; therefore coupling is only between the probe loop and the sensor loop. Figure 3.18 shows the sensor loop mounted to polycarbonate and Figure 3.19 shows the experimental set-up.

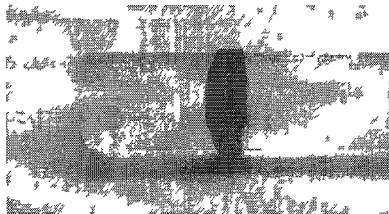


Figure 3.18 - Sensor loop on polycarbonate cylinder

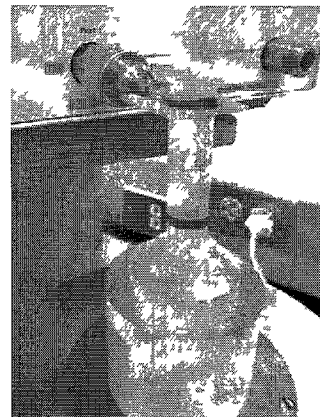


Figure 3.19 – Polycarbonate sensor loop inside probe loop

Figure 3.20 shows the impedance and phase information for the polycarbonate cylinder sensor loop assembly. A clear resonance is produced at approximately 1.4 GHz where the imaginary part of the impedance goes to zero. For a parallel resonant circuit, the bandwidth is measured from the magnitude data that corresponds to half power (3dB). Since voltage is proportional to impedance, half power on the impedance curve equals 70.7% of the maximum impedance. (15). Q-factor can be calculated based on the following formula.

$$Q = \frac{f_r}{f_u - f_l} \quad (3.3)$$

where  $f_r$  is the resonant frequency,  $f_l$  is the lower frequency, and  $f_u$  is the upper frequency (the difference of the upper and lower frequency is also referred to as bandwidth). The Q-factor of the plastic cylinder is 60.4.

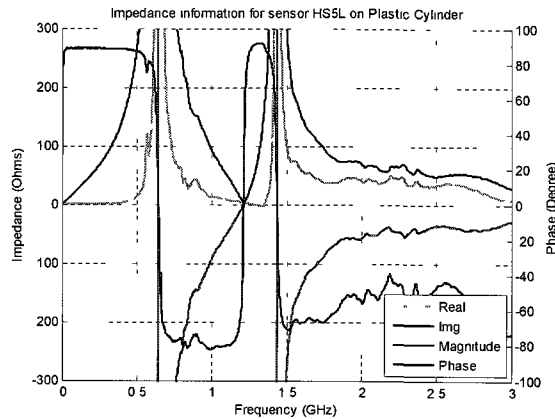


Figure 3.20 - Polycarbonate mounted sensor loop response

We mounted the sensor loop to a copper cylinder because of copper's low electrical resistance ( $16.78 \text{ n}\Omega \cdot \text{m}$  at  $20 \text{ }^\circ\text{C}$ ), serving as a benchmark of the sensor loops response on a low loss material. Figure 3.21 shows the sensor loop mounted on the copper insert and Figure 3.22 shows the experimental set-up.

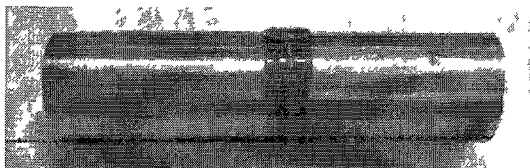


Figure 3.21 - Sensor loop on copper cylinder

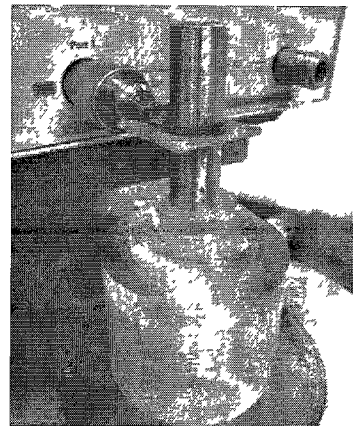


Figure 3.22 – Copper sensor loop inside probe loop

Figure 3.23 shows the impedance and phase information for the copper cylinder sensor loop assembly. Resonance occurs at approximately 1.6 GHz and the Q-factor was 31.5.

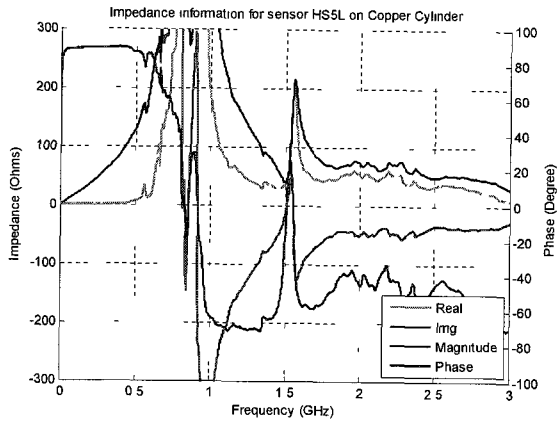


Figure 3.23 - Copper mounted sensor loop response

We choose high strength steel (HSS) and carbide because most tools used in machining are of one of these materials. Figure 3.24 shows the sensor loop mounted to a 2 flute high strength steel tool bit and Figure 3.25 shows the experimental set-up.



Figure 3.24 - Sensor loop on high strength steel tool bit

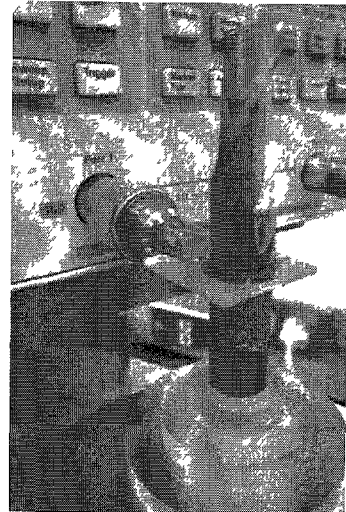


Figure 3.25 – HSS sensor loop inside probe loop

Figure 3.26 shows the impedance and phase information for the HSS tool bit sensor loop assembly. A weak resonance indicated by the magnitude is shown at 1.7 GHz, although no-zero crossing is observed in the phase. The Q-factor for the HSS tool bit was 10.1.



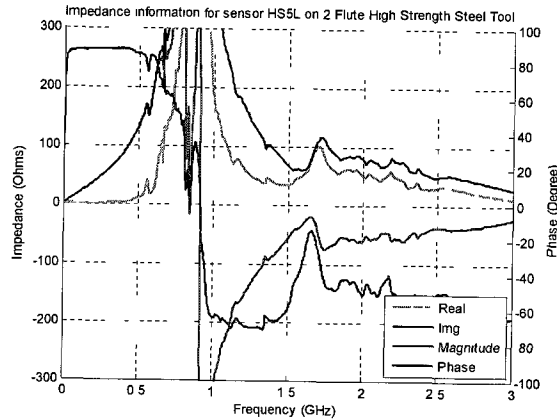


Figure 3.26 - High strength steel tool bit mounted sensor loop response

Figure 3.27 shows the sensor loop mounted to a double sided 4 flute carbide tool bit and Figure 3.28 shows the experimental set-up.

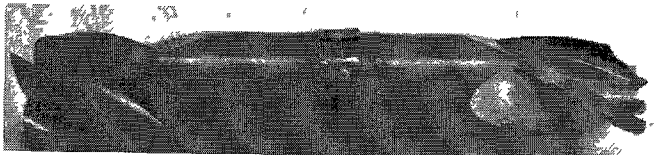


Figure 3.27 - Sensor loop on carbide tool bit



Figure 3.28 – Carbide sensor loop inside probe loop

Figure 3.29 shows the impedance and phase information for the cemented carbide tool bit sensor loop assembly. We observe resonance at 1.7 GHz indicated by a zero-crossing in the phase information. The Q-factor for the carbide tool bit was 19.3.

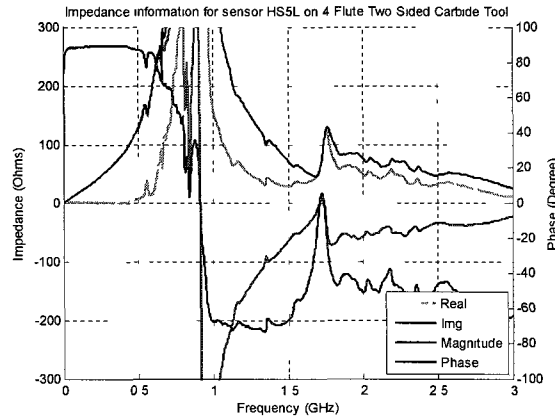


Figure 3.29 - Carbide tool bit mounted sensor loop response

From these results, we attempted to increase the Q-factor for the HSS tool bit and carbide tool bit by mounting 50  $\mu\text{m}$  thick copper foil between the sensor and the tool bit. The electrical connection from the copper to the tool bit was facilitated with Pelco colloidal silver liquid as can be seen in Figure 3.30 and Figure 3.31.

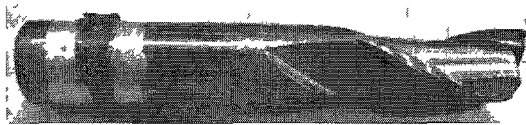


Figure 3.30 - Sensor loop on HSS

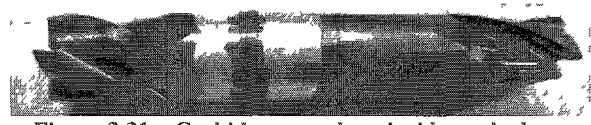


Figure 3.31 - Carbide sensor loop inside probe loop

Figure 3.32 and Figure 3.33 shows the impedance and phase information for the sensor and tool assemblies shown above. We see resonance occur in both plots, as well as a Q-factor increase when comparing the copper and silver standoff assembly responses to the bare tool response in Figure 3.26 and Figure 3.29. The Q-factor for the copper foil and silver liquid on the carbide tool bit was 30.8. The Q-factor for the copper foil and silver liquid on the HSS tool bit was 29.6.

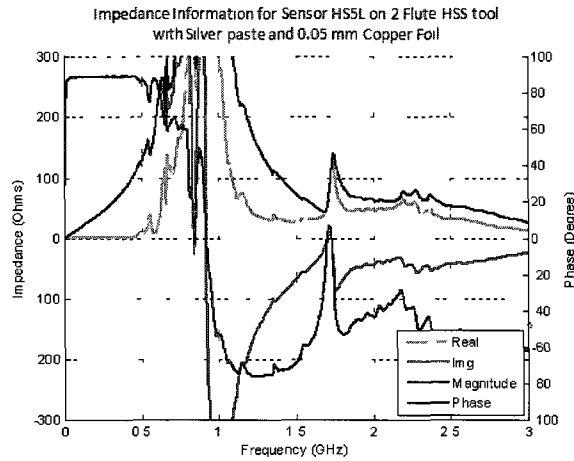


Figure 3.32 - System response of sensor loop with Ag/Cu standoff on HSS tool bit

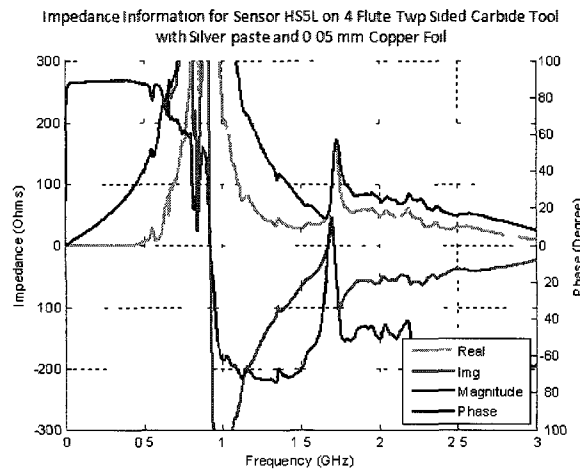


Figure 3.33 - System response of sensor loop with Ag/Cu standoff on carbide tool bit

Table 3-3 shows the Q-factors observed for the different insert materials. We conclude from this information that the resistance of the core material has an impact on the Q-factor of the resonance and is an important factor that requires consideration. From a design perspective, implementing a shorted copper loop beneath our sensor loop displaces the sensor further from the tool surface which could impact the strain sensitivity. More investigation is needed to evaluate this claim.

<b>Material</b>	<b>Quality Factor (Q)</b>
Polycarbonate	60.4
Copper	31.5
HSS	10.1
Carbide	19.3
HSS with Cu and Ag	29.6
Carbide with Cu and Ag	30.8

Table 3-3 - Quality factors for the insert materials tested

### **3.3 DIELECTRIC THICKNESS**

The purpose of this experiment was to increase coupling between the outer probe loop and the inner sensor loop. The coupling was evaluated for several different dielectric thicknesses between the sensor loop and the tool bit.

The 5 flute carbide tool bit was mounted on a vertical translation stage mounted to a fixed post on a breadboard. The coupling between a sensor loop and the tool was evaluated for three different dielectric thicknesses listed in Table 3-4.

<b>Description</b>	<b>Tool Stand-off Distance (<math>\mu\text{m}</math>)</b>
Insulated motor wire	50
One-ply Kapton	88.9
Two-ply Kapton	177.8

Table 3-4 - Sensor loop to tool separation distance

The sensor loop consisted of bare 30 AWG wire except for the case were insulated motor wire with 50  $\mu\text{m}$  thick dielectric was used for the smallest standoff distance. The Kapton tape consisted of 50  $\mu\text{m}$  thick polyimide film with 40  $\mu\text{m}$  thick adhesive. The sensor loop consists of the wire and a 0.6 pF ceramic capacitor. Figure 3.34 shows the 5-flute carbide end mill tool bit with the different sensor loops.

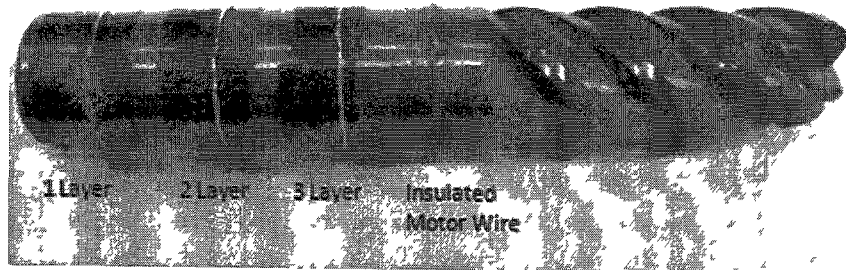


Figure 3.34 - Sensor loops mounted on carbide tool bit

The probe loop was a 14.61 mm inner diameter loop, 0.813 mm wide and 18  $\mu\text{m}$  thick trace on 1.45 mm thick FR-4, shown in Figure 3.2. We connected the loop to Agilent Technologies E5062A 75-ohm Vector Network Analyzer (VNA) with a 50 ohm type-N to SMA adaptor and 50-ohm SMA end launch connector. Given that we used one probe loop with a fixed diameter, the only other variable in addition to the stand-off distance was the distance between the sensor loop and probe loop. We could have accounted for the sensor loop to probe loop distance by using multiple probe loops with different diameters, but then errors in alignment and repeatability arise.

Figure 3.35 shows the impedance and phase dependence for the probe loop connected to the VNA. The phase discontinuity at  $\sim 470$  MHz and 1.5 GHz is attributed to the impedance mismatch of the adaptor and connector to the VNA's source. The response from this plot can be used as a control, such that any differences from this response are due solely to the presence of the sensor loop.

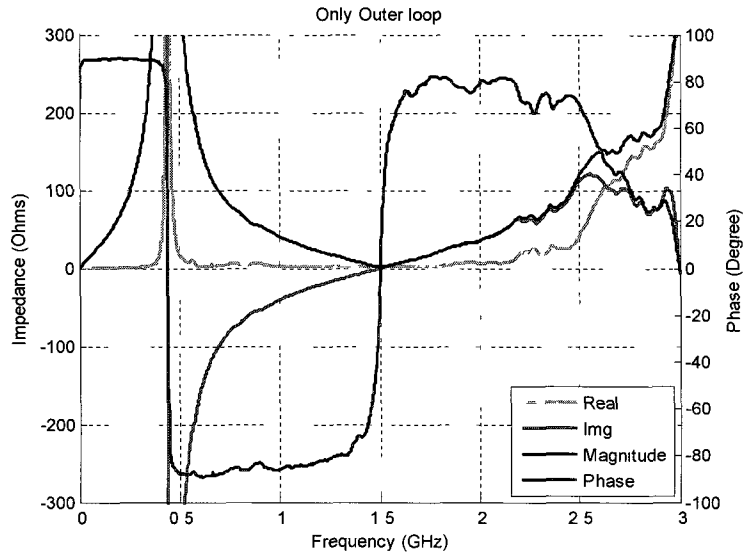


Figure 3.35 - Only Probe Loop's response

Figure 3.36 shows the response for no-standoff sensor loop with the 0.6 pF capacitor. Ripples were seen throughout the spectrum when comparing this response to Figure 3.35, but no true resonant behavior was produced.

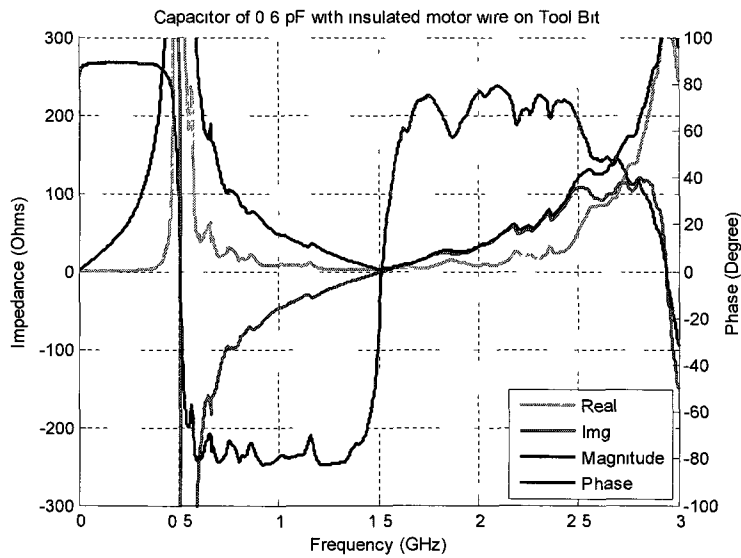


Figure 3.36 - Probe loop and no-standoff sensor response

Figure 3.37 shows the sensor loop response for the wire with 88.9  $\mu\text{m}$  thickness dielectric with the 0.6 pF capacitor. A resonant peak with a quality factor of 53.5 was exhibited at approximately 1.65 GHz.

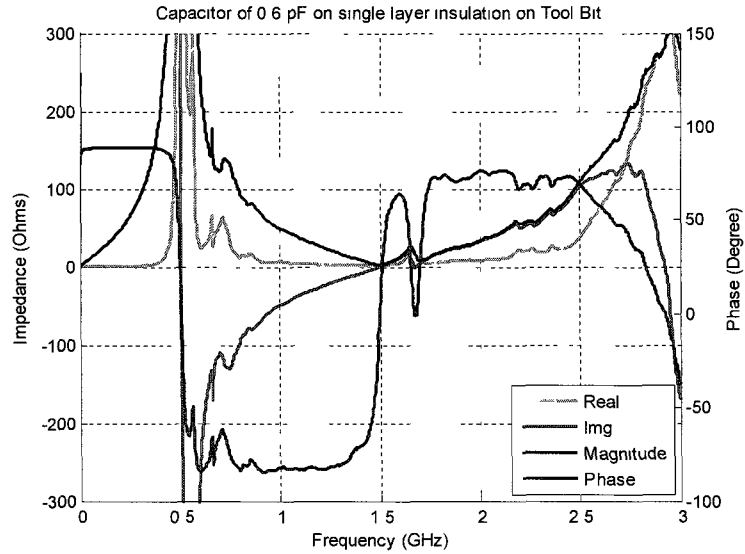


Figure 3.37 - Probe loop and one-ply standoff sensor response

Figure 3.38 shows that the resonant peak shifted downward to 1.5 GHz and quality factor of 76.0, when the sensor loop has 177.8  $\mu\text{m}$  thickness of dielectric between the wire loop and the tool.

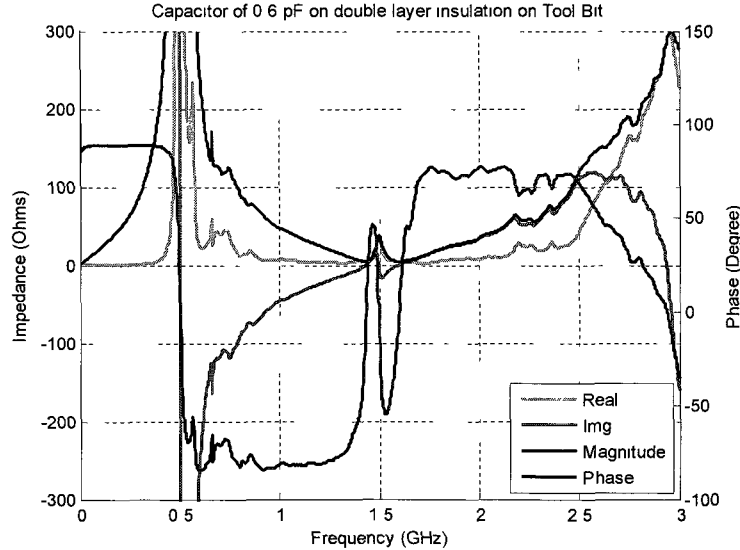


Figure 3.38 - Probe loop and two-ply standoff sensor response

The data presented above show that increasing the stand-off distance between the tool surface and the sensor loop increases the coupling. The dielectric thickness for maximum coupling was 177.8  $\mu\text{m}$ .

With an increase in dielectric stand-off distance, there is a decrease in the probe loop to sensor loop separation distance. A reduction in the probe loop diameter was shown to change the quality factor by 12.5 per mm, while an increase in the dielectric stand-off distance was shown to change the quality factor by 126.5 per mm.

### 3.4 SENSOR PERTURBATIONS

The purpose of this experiment was to determine the system resonant frequency sensitivity to variations in sensor loop location. The sensor loop location was evaluated for displacements in x, y, and z directions as a function of rotation ( $\theta$ ) about the z-axis. The origin for rotation is when the sensor is 180 degrees from the input to the loop. Figure 3.39 shows the coordinate system from the above perspective.

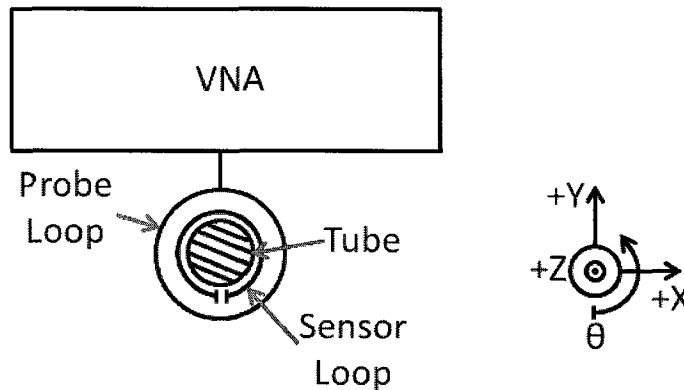


Figure 3.39 – Equipment layout and coordinate system

We represented the tool by an aluminum tube with a 29.21 mm inner diameter and a 31.75 mm outer diameter and the sensor loop with a Pyralux band of 1.35 mm vertical thickness wrapped around the circumference of the tube with a 7.57 mm overlap section producing a parallel plate capacitor. Figure 3.40 shows a picture of the actual sensor band mounted to the aluminum tube.



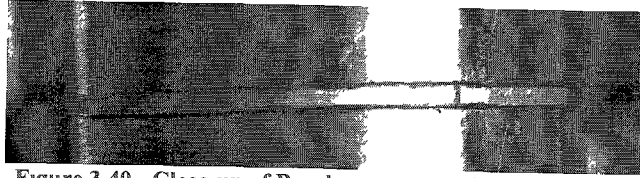


Figure 3.40 - Close-up of Piralux sensor on Aluminum tube

For the probe loop, we used a two turn printed circuit board (PCB) loop with a trace thickness of  $18\ \mu\text{m}$  and trace width of  $4\ \text{mm}$ . The signal was launched into the loop through a  $25\ \text{mm}$  transverse electro-magnetic transmission line connected to a  $50\text{-ohm}$  SMA end launch connector. Figure 3.41 shows the actual probe loop and SMA connector.

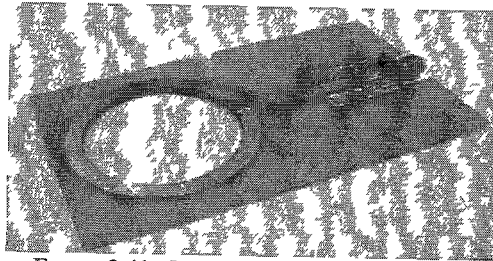


Figure 3.41 - Double turn PCB probe loop

The aluminum tube was placed on a rotational stage ( $\theta$ ) which was mounted to a vertical translation stage ( $z$ -axis) connected to a post with its base fixed to two translational stages ( $x$ -axis and  $y$ -axis) mounted on an optical bread-board. Figure 3.42 shows a picture of the experimental set-up.

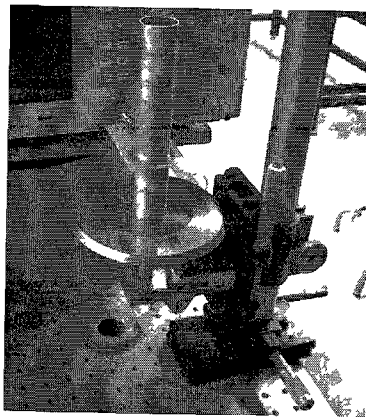


Figure 3.42 - Photo of experimental set-up showing rotational and translational stages

We benchmarked the sensor at the origin by recording the resonant frequency as indicated by the phase discontinuity from the S11 scattering parameter for 30 degree rotation increments; this is represented in the following plots as ‘origin’. Then with the sensor displaced  $\pm 50 \mu\text{m}$  in the x, y, or z directions, the resonant frequency was again recorded at 30 degree rotational steps. The 30 degree step size was determined to be small enough to characterize system response waveform.

Figure 3.43 shows the resonant frequency of the system as a function of angular displacement due to displacements in the x-direction, which is lateral to the transmission line coupling to the probe loop. The resonant frequency of the system varies by 0.1 % as the sensor is rotated. This frequency variation due to the lateral displacement is a magnitude of two higher than the strain resolution design parameter, but given that it follows a periodic, repeatable waveform could be removed with signal post-processing.

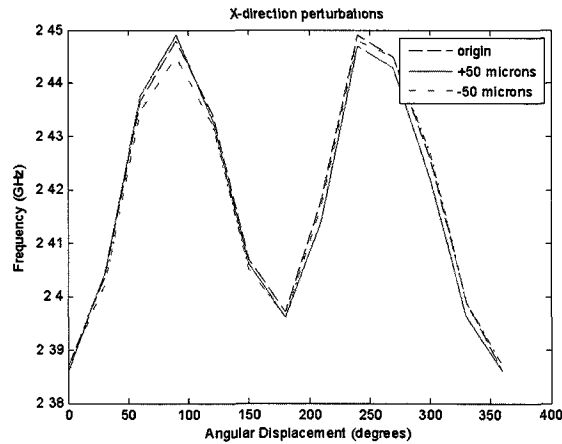


Figure 3.43 - Resonant frequency variation due to x-direction displacement

Figure 3.44 shows the resonant frequency of the system as a function of angular displacement due to displacements in the y-direction, which is longitudinal to the transmission line coupling to the probe loop. The resonant frequency of the system varies by a maximum of 0.8 % as the sensor is rotated. The frequency variation due to

this displacement of the sensor is about a magnitude of about three times higher than the strain resolution design parameter. This coordinate perturbation produces the greatest effect when compared to the x-axis and z-axis responses; therefore the design and implementation of the system should be to minimize this displacement.

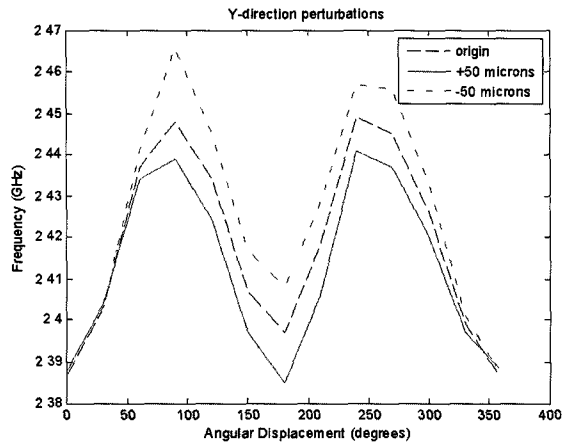


Figure 3.44 - Resonant frequency variation due to y-direction displacement

Figure 3.45 shows the resonant frequency of the system as a function of angular displacement due to displacements in the z-direction, which is along the axis of the transmission line coupling to the probe loop. The resonant frequency of the system varies by 0.1 % as the sensor is rotated. This frequency variation due to this displacement is magnitude of two times higher than the strain resolution design parameter, but given that it follows a periodic waveform could be removed with signal processing.

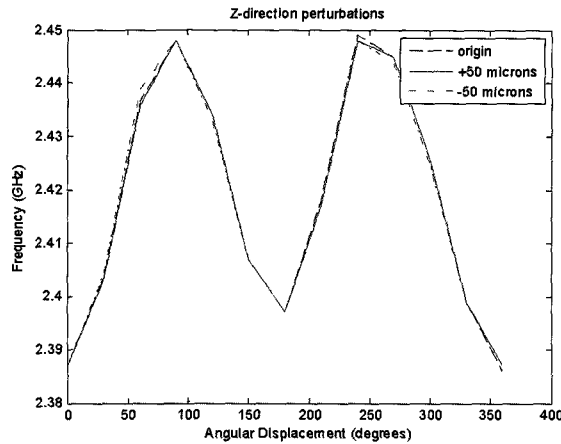


Figure 3.45 - Resonant frequency variation due to z-direction displacement

The strain signal we expect to observe from our sensor is proportional to the normalized change in frequency. Figure 3.46 shows the normalized frequency change as a function of rotation angle and sensor displacement. The figure shows that the y-axis variation, moving the sensor closer and farther from probe loop feed point, yields a much stronger dependence than seen in the x-axis or z-axis directions.

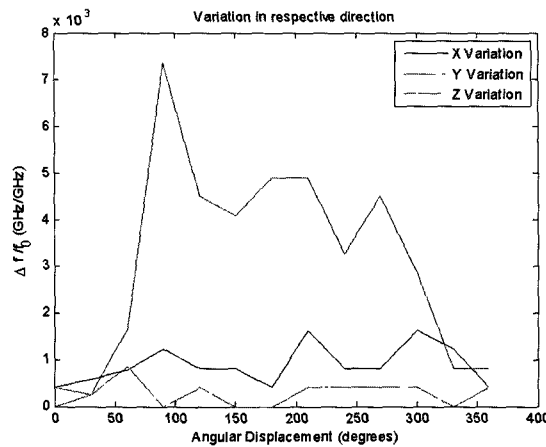


Figure 3.46 - Normalized change in frequency for various displacement directions

### 3.5 CHAPTER SUMMARY

In this chapter, we experimentally observed that the frequency change due to sensor capacitance was greatest when the sensor had a capacitance of less than 1 pF.

This was determined using Pyralux overlap type capacitors and discrete surface mount technology capacitors mounted on high strength steel or cemented carbide tool bits.

We experimentally determined that a reduction in the insert material's conductance reduced the quality factor of the system resonance. The reduction of conductance increases the depth that induced currents penetrate in the insert material, which increases the power loss to the insert material.

We experimentally concluded that a greater stand-off distance from the sensor loop to the insert material increased the quality factor of the resonance. The highest quality factor of 76 was observed using a Kapton stand-off distance of 177.8  $\mu\text{m}$ .

Finally, we experimentally found the greatest system resonant frequency sensitivity due to sensor loop displacement occurred when the sensor loop was traversed in the direction of the probe loop feed.

## CHAPTER 4

### STRAIN SENSOR

This chapter is focused on the design of the strain sensor, which is a component of the sensor loop. In previous chapters, the strain sensor has also been referred to as a variable capacitor. We begin with the material stack up used for the fabrication of the sensor. Next we look at the different parameters for increasing the capacitance and obtaining a better strain sensitivity. Then we discuss the deformation of the tool bit during a cutting process and the associated strains. Finally, we show simulations on how the ICCS's capacitance will vary with orientation and strain.

#### 4.1 SENSOR MATERIAL

The sensor loop is the portion of the system that detects strain. The sensor loop resides on the shank of the tool bit and detects strain with an interdigitated comb capacitor structure (ICCS). The probe loop is excited by a radio frequency (RF) source, which provides the electro-magnetic coupling required for communication between the probe loop and the sensor loop.

There are two components to the sensor loop, the ICCS and the inductive loop. Figure 4.1 shows a simplified electrical schematic of the sensor loop.

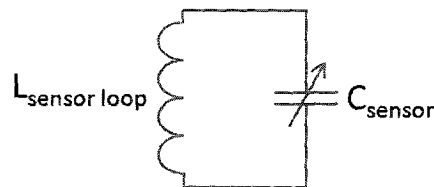


Figure 4.1 - Simplified sensor loop representation

The ICCS strain sensor (represented in Figure 4.1 as a variable capacitor labeled  $C_{\text{sensor}}$ ) is located at the termination of the inductive loop. The sensor loop assembly was produced using a double sided flexible circuit manufacturing technique. The base laminate is ½ oz. copper (bottom layer), 25 µm adhesive, 76 µm Dupont Kapton, 25 µm adhesive, and ½ oz. copper (top layer). The top and bottom layer copper was pattern plated for a 1.5 oz. finished copper weight. The bottom and top layer are insulated with 51 µm adhesive and 25 µm Dupont Kapton. Figure 4.2 shows a cross-section of the material stack up.

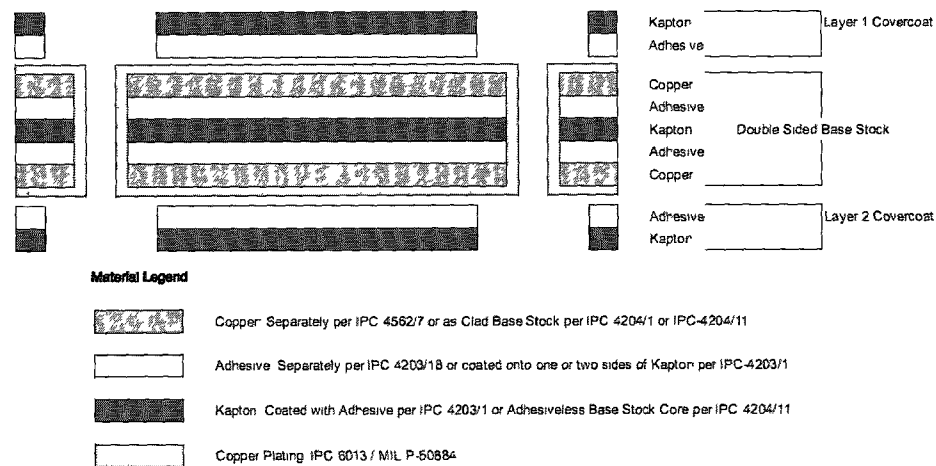


Figure 4.2 - 2-layer flexible circuit construction (16)

The ICCS was printed on the bottom layer of the board to give it close proximity to the strained surface, and the inductive loop was printed on the top layer to increase coupling to the probe loop and decrease radiative losses induced into the machine tool. The ICCS and probe loop are connected with an octagon via with an outer diameter of 1.42 mm, an inner diameter of 0.74 mm, and a drill size of 0.33 mm.

## 4.2 ICCS DESIGN

We designed several different iterations for the ICCS portion of the sensor loop. The variables that we explored were: number of fingers, length of fingers, double-layer capacitors, proximity of via distance to sensor, via capacitance, and multilayer ceramic capacitors. Lvovich, Liu and Smiechowski provided the relation below which relates the capacitance to its geometrical design (see Figure 4.17 or Figure 4.18 for simulated plot of normalized capacitance versus strain).

$$C = LN \frac{4\epsilon_0\epsilon_r}{\pi} \sum_{n=1}^{\infty} \frac{1}{2n-1} J_0^2\left(\frac{(2n-1)\pi s}{2(s+w)}\right) \quad (4.1)$$

where  $N$  is the number of fingers,  $L$  is the length of the finger overlap,  $s$  is the width of the space between the fingers,  $w$  is the width of the finger,  $J_0$  is a zero-order Bessel function,  $\epsilon_0$  is the permittivity of free space, and  $\epsilon_r$  is the relative permittivity of the dielectric.

The number of fingers is directly proportional to the capacitance of the sensor based on the Equation 4.1. The number of fingers was a factor we explored for two reasons, with fewer fingers we are detecting strain over a smaller area as illustrated in Figure 4.3 yielding a better spatial resolution. However, with more fingers we produce a larger capacitance thus yielding a lower system resonant frequency. Most of the sensors we designed had a total finger count between 4 and 12; we also experimented with double layer capacitors having a total of up to 24 fingers.



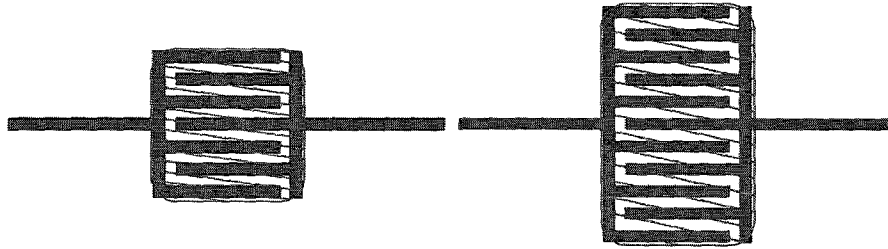


Figure 4.3 - Strain sensitive areas (red cross-hatched) for sensors with different number of fingers

We also increased the capacitance by increasing the length of the fingers. A substantial portion of the sensors we designed were of two different lengths: 1.27 mm and 2.54 mm. We also experimented with other designs which contained multiple sensors on the same assembly (an example is provided in Figure 4.4); the finger lengths of these designs were: 2.46mm, 2.60 mm and 2.66 mm. This example used two different finger lengths to produce two different capacitances, which creates two separate signals (two different resonant frequencies).

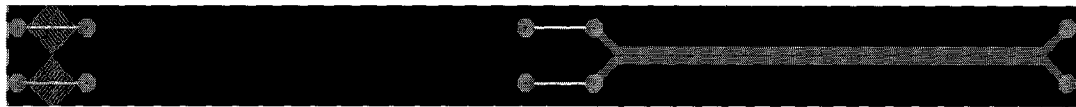


Figure 4.4 - Torsional strain sensors on the same assembly (equal number fingers, differing length of fingers)

Another method used to increase the capacitance was placing two capacitors in parallel. In a parallel configuration, the capacitors capacitance sums together. This was accomplished by printing ICCS's on both the top and bottom layer of double layer board. Figure 4.5 shows the circuit schematic representation and the physical representation for this configuration.

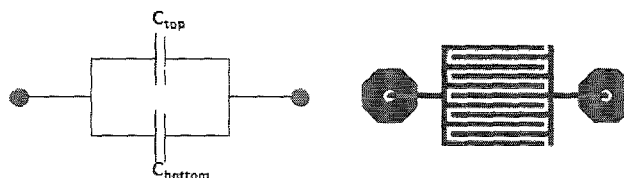


Figure 4.5 - Left is the circuit schematic representation, right is the board level representation (top and bottom layers directly overlaid)

Another variable that impacts the total capacitance of the sensor loop is the stray capacitance between the via and the sensor and the via itself. Figure 4.6 shows a 3-D CAD model explaining the components of an ICCS assembly.

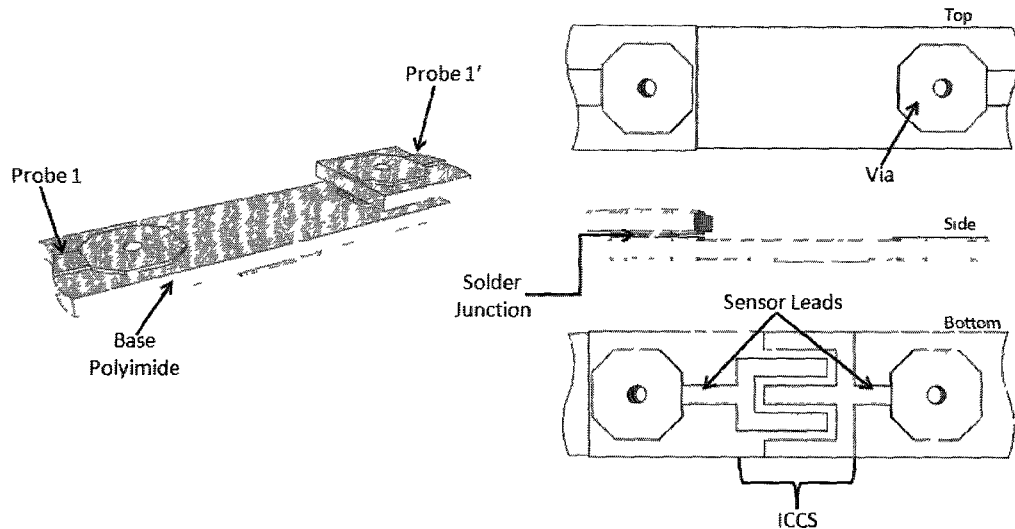


Figure 4.6 - Perspective, Top, Side, and Bottom view of Sensor assembly

Figure 4.7 and Figure 4.8 show an ICCS assembly with the polyimide removed with explanation of the sources of capacitance associated with the sensor.

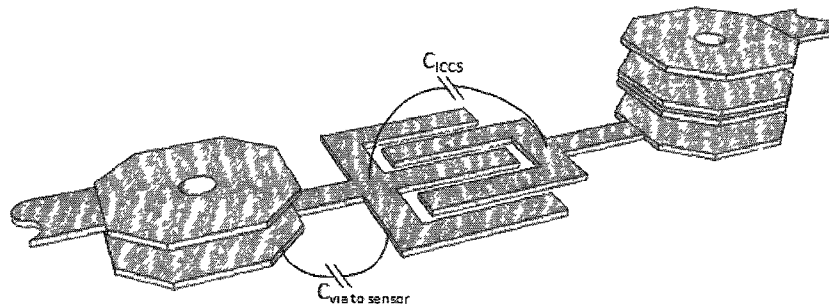


Figure 4.7 - Parametric view of assembly with associated capacitance



Figure 4.8 - Side View of assembly with associated capacitance

With these sources of capacitance thoroughly understood, we can add additional complexity to Figure 4.1 producing Figure 4.9.

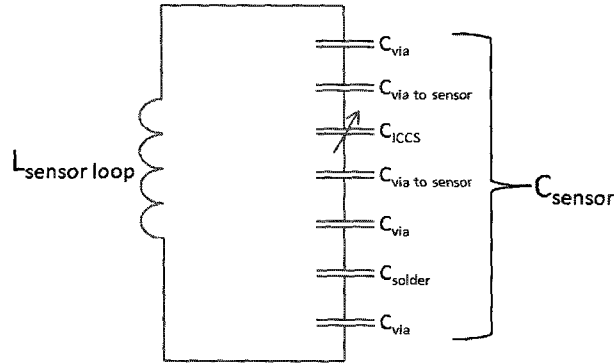


Figure 4.9 - Expanded capacitance for sensor loop assembly

These effects are shown in a serial configuration with only one variable capacitive element. The capacitance from the via to sensor could be represented as variable as well, but its effect is small when compared to the capacitance change with respect to the ICCS. With further investigation and testing, the configuration (serial/parallel) of the capacitances may need to be altered.

We designed our sensors to evaluate the relative impact of several of these additional capacitances by producing three types of sensors: fixed via to via distance, fixed sensor to via distance, and sensors without vias. Figure 4.10 shows an illustration of these designs. The fixed via to via distance is 3.45 mm and the fixed via to sensor distance is 0.128 mm.

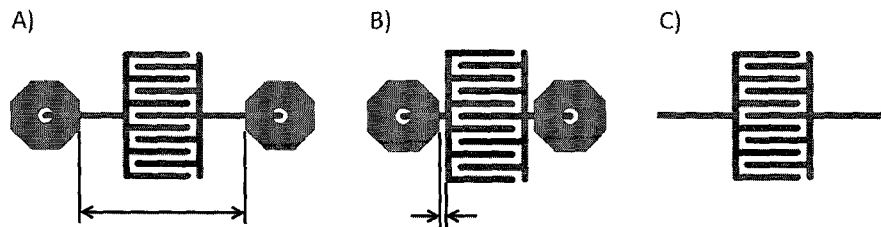


Figure 4.10 – ICSS designs: A) fixed via to via distance, B) fixed via to sensor distance, and C) sensor without vias

The solder junction capacitance is constant once a sensor assembly is attached to a tool bit, but may be a source of variability when evaluating reproducibility. Given the operating frequency of our system, residual flux from the soldering process can be a

source of capacitance (17). Another component of capacitance at this junction is due to the parallel plate capacitance of the via connection. Figure 4.11 shows a solder joint with and without parallel plate capacitance.

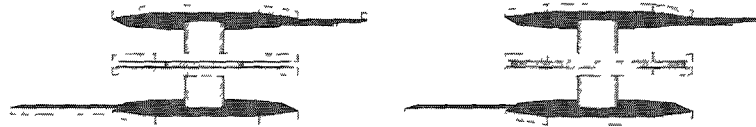


Figure 4.11 – Left: Via connection with parallel plate capacitance, Right: Via connection with negligible parallel plate capacitance

### 4.3 TOOL DEFORMATION

When a cutting tool is removing material from a work piece, the bending and torsional strains are needed to fully describe the tools deformation. Figure 4.12 shows a tool bit undergoing a cutting process.

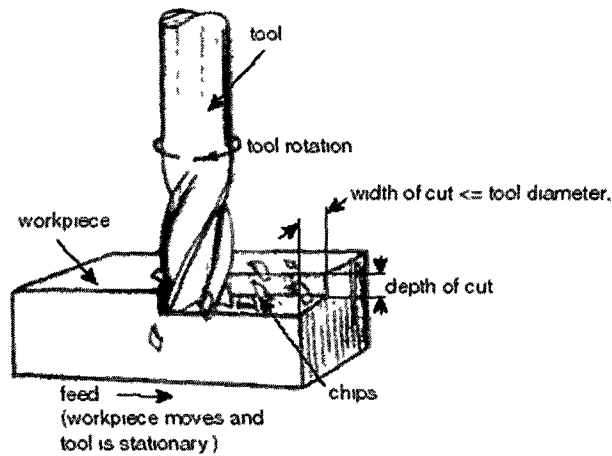


Figure 4.12 - Work piece and tool bit during cutting process (18)

The bending and torsional strains on a tool bit are shown visually in Figure 4.13. Figure 4.13a shows a tool bit undeformed before the cutting process, and Figure 4.13b shows a tool with only bending strain and Figure 4.13c shows a tool bit with only torsional strain. Both bending and torsional strain occur simultaneously during a cutting process when using a multiple tooth tool bit. Although for calibration, a single tooth tool bit with specific sensor location can be used to nearly isolate the two strain signals.

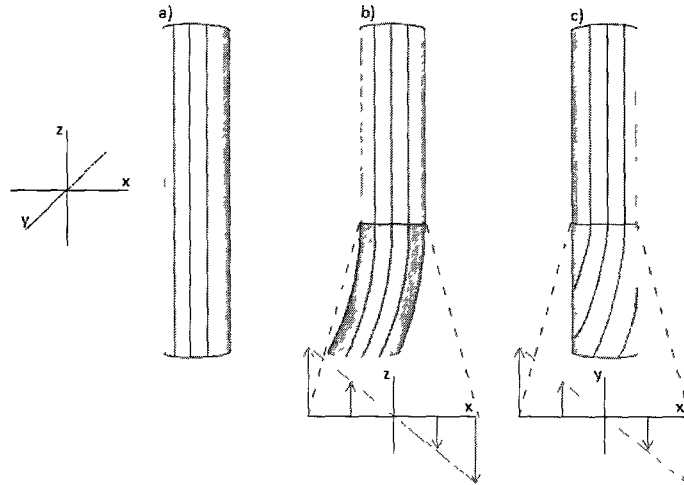


Figure 4.13 - Undeformed tool (a), tool exhibiting bending stress (b), and tool exhibiting torsional stress (c)

The plot below Figure 4.13b shows the bending strain in the x-z plane. In this plot, the right side of the tool bit is in tension and the left side of the tool bit is in compression. This type of strain is measured by using a vertically oriented comb capacitor (i.e. the comb capacitor's fingers aligned in the z-axis). Figure 4.14 shows a vertically oriented gage, designed for bending strain detection.

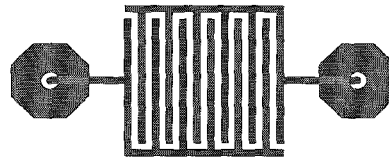


Figure 4.14 - Bending Sensor

The plot shown below Figure 4.13c shows the torsional strain in the x-y plane. This type of strain is measured using a comb capacitor rotated 45 degrees to the z-axis. Figure 4.15 shows a 45 degree rotated gage, designed for torsional strain detection.

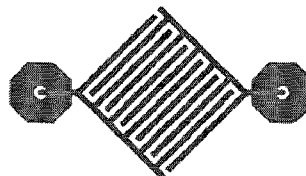


Figure 4.15 - Torsional Sensor

The bending and torsional strains happen simultaneously and orthogonal effects due to Poisson's ratio occur. Therefore the signal measured directly from the gages will

contain information from the bending and torsional strain. As mention previously, through proper testing and calibration utilizing a single tooth tool bit with specific sensor locations, the strains can be approximately isolated resulting in the desired measurements.

#### **4.4 ICCS ORIENTATION**

The purpose of this simulation was to determine the strain sensitivity of the interdigitated comb capacitor as a function of its orientation. The three sensor orientations we investigated were designed and produced on the flexible circuit board.

The three sensor designs we investigated had fingers aligned horizontally, vertically, and 45 degrees rotated. Figure 4.16 shows the three sensor orientations.

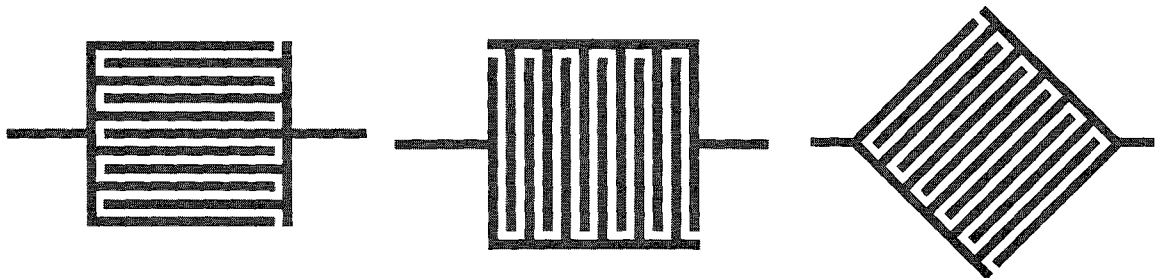


Figure 4.16 - Comb capacitor orientations

Equation 4.1 was used to calculate the change in capacitance based on geometrical parameters. Assuming a uniaxial loading situation, the in-plane geometrical parameters were deformed according to the load and the out-of-plane geometrical parameters were deformed according to the load and Poisson's ratio.

Figure 4.17 shows the direction of the load for the horizontally oriented gage and the resulting normalized capacitance change versus strain. The relation between strain and capacitance in this orientation is

$$\frac{\Delta C}{C} = \nu * \epsilon_{axial} \tag{4.2}$$

where  $\nu$  is Poisson's ratio and  $\epsilon_{axial}$  is the axial strain. This sensor, when mounted on a tool bit, would be most sensitive to circumferential strain.

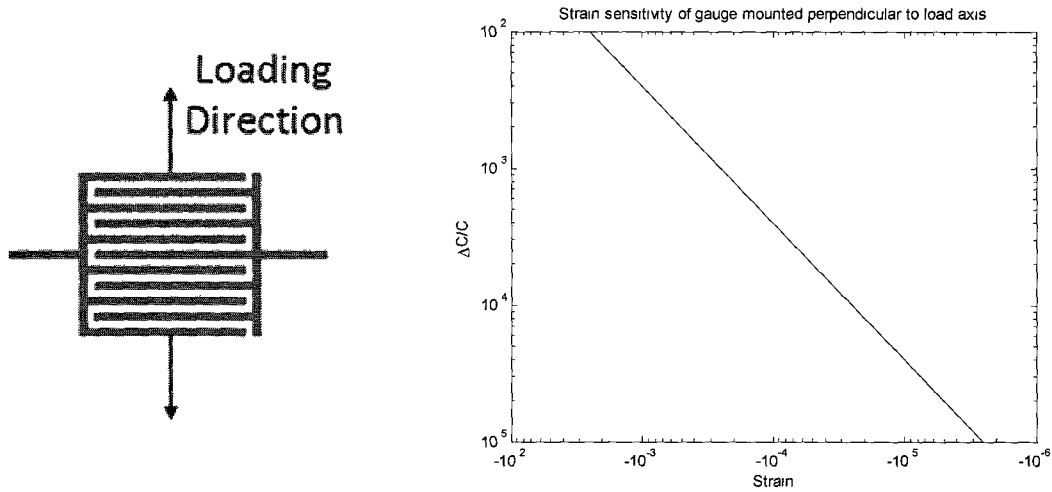


Figure 4.17 - Comb capacitor orientation perpendicular to force application and resulting output

Figure 4.18 shows the direction of the load for the vertically oriented gage and the resulting normalized capacitance change versus strain. The relation between strain and capacitance in this orientation is provided in Equation 4.3. This sensor, when outfitted to a tool bit, would be most sensitive to axial strain.

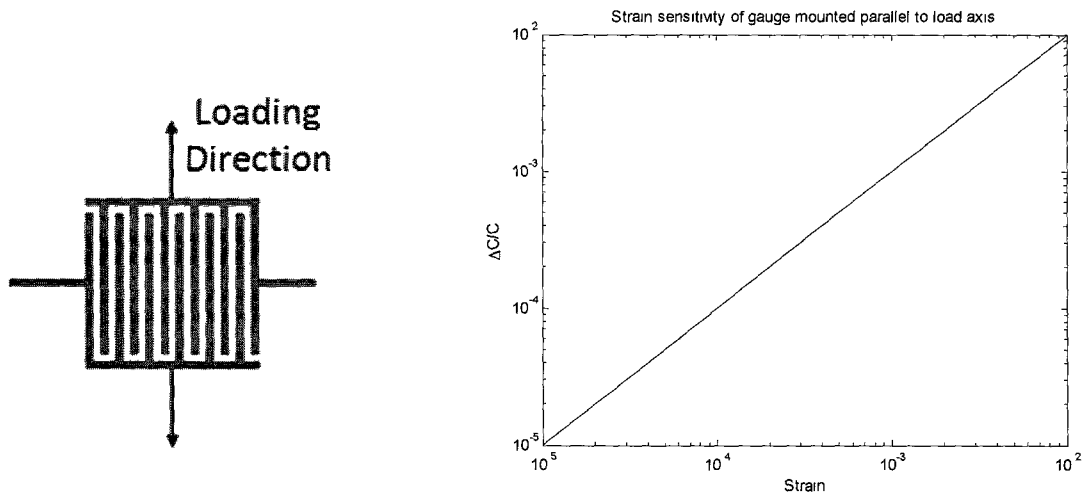


Figure 4.18 - Comb capacitor orientation parallel to force application and resulting output

$$\frac{\Delta C}{C} = \epsilon_{ax} \tag{4.3}$$

The rotated sensor's normalized change in capacitance versus strain relationship is more complicated than the horizontal and vertical sensors. If the rotated sensor experienced a pure shear strain, then the output will be similar to that in Figure 4.18. This loading scenario can be visualized using Figure 4.19 (19). Figure 4.19A shows a differential element under a state of pure shear, Figure 4.19B shows the differential element decomposed into its principal tensile stresses ( $\sigma_1$  and  $\sigma_2$ ), and Figure 4.19C shows the Mohr's circle representation of pure shear.

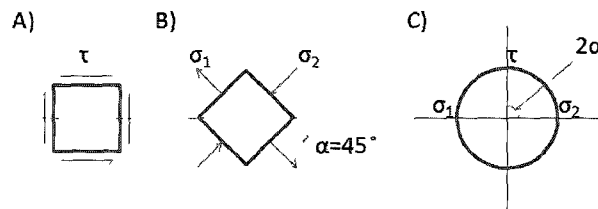


Figure 4.19 - Pure shear strained differential element

However, when the loading state is more complicated than pure shear, the sensor will experience a strain along the axis of the fingers as well as transverse to the axis of the fingers. Given that it is difficult to specify the ratio of strain from torsion and bending, it is difficult to develop a closed form solution. Figure 4.20 provides a simplified visual representation showing this more complex strain state. Figure 4.20A shows a differential element under shear and bending strain, Figure 4.20B shows the differential element decomposed into its principal tensile stresses ( $\sigma_1$  and  $\sigma_2$ ), and Figure 4.20C shows the Mohr's circle representation.

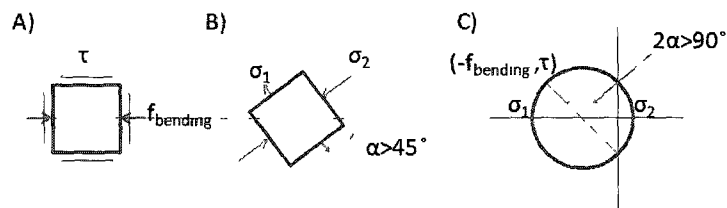


Figure 4.20 - Complex strain state differential element



## **4.5 CHAPTER SUMMARY**

In this chapter, we began by describing the material's that were used for producing the ICCS sensors and sensor loops. We described the various parameters of the sensors and sensor loops and their impact on the total sensor loop capacitance, which were designed and manufactured using a flexible circuit technique.

Next, we discussed the deformation of a tool bit during the material removal process as well as candidate designs of how the various strains can be detected. Finally, we present results of simulations for the expected change in capacitance for the various designs. We determined from simulation that a sensor with its fingers oriented in the direction of the strain was more sensitive than a sensor with its fingers oriented perpendicular to the strain. The ICCS sensor with its fingers oriented parallel to the strain yielded a normalized change in capacitance which was equal to strain, whereas the ICCS sensor with its fingers oriented perpendicular to strain yielded a normalized change in capacitance equal to the product of strain and Poisson's ratio.

## CHAPTER 5

### RESONANCE DETECTION

This chapter details the equipment and circuit used for resonance detection. We begin with the commercially available vector network analyzer and a description of its functionality. Then, we discuss the design process of our in-house fabricated resonance detection circuit. Finally, a comparison is made between results obtained with the commercially available vector network analyzer and our fabricated circuit.

#### **5.1 COMMERCIAL VECTOR NETWORK ANALYZER**

We initially began developing and characterizing our system (probe and sensor loop) with Agilent Technologies E5062A Vector Network Analyzer (VNA). This highly sensitive, robust piece of equipment provided critical information early in the design cycle for concept validation. Yet with any highly complex piece of equipment, it had excessive functionality and also carried an expensive price tag (~\$20k). In addition to the price and excessive functionality of a VNA, the space inside a CNC mill machining envelope is fully utilized and cannot accommodate a 0.23 X 0.37 X 0.42 m<sup>3</sup> VNA. The VNA is not suited for the harsh environment produced during a machining process. With these reasons as motivation, we determined that producing our own resonance detection circuit was important.

A VNA is similar in function to a spectrum analyzer with a tracking generator circuit (20). Figure 5.1 provides a high-level block diagram for a functional understanding of the components for a VNA, where  $a_{DUT}$  is the test signal injected into

the DUT,  $b_{DUT}$  is the received signal altered by the DUT, and  $\Gamma_{DUT}$  is the reflection coefficient of the DUT.

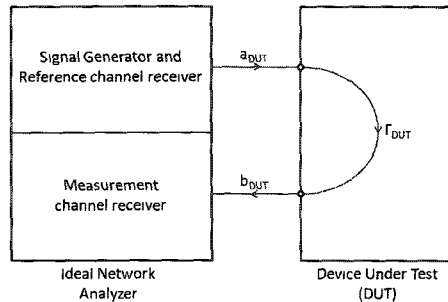


Figure 5.1 - Simplified version of Vector Network Analyzer

From this graphical representation, the major sub-systems of a VNA are seen: the generator (and its measurement), the device under test (DUT), and the receiver.

## **5.2 IN-HOUSE FABRICATED VECTOR NETWORK ANALYZER**

This section describes the circuit components and how they relate to the overall function of the resonance detection system.

Figure 5.2 shows a block diagram of the first version of the prototyped VNA/resonance detection circuit. Control of this circuit was provided by an Exetech 382280 Programmable DC power supply which generated the tuning voltage for the VCO. This voltage source was used because the tuning voltage range was 1 to 24 volts. We measured the output voltage from the power supply as it was applied to the tuning voltage of the VCO, and with help of the specification sheet for the VCO, we could determine the radio frequency output from the VCO. We utilized the automated test sequence function of the power supply to provide a stair step input voltage enabling a full spectrum frequency sweep of the VCO. This method was a benchmark, but unfortunately it yielded a 90 second sweep time and we also determined this device contained a large

amount of noise. The noise on the input to the VCO results in a frequency modulation at its output, which reduces the quality of the measurements.

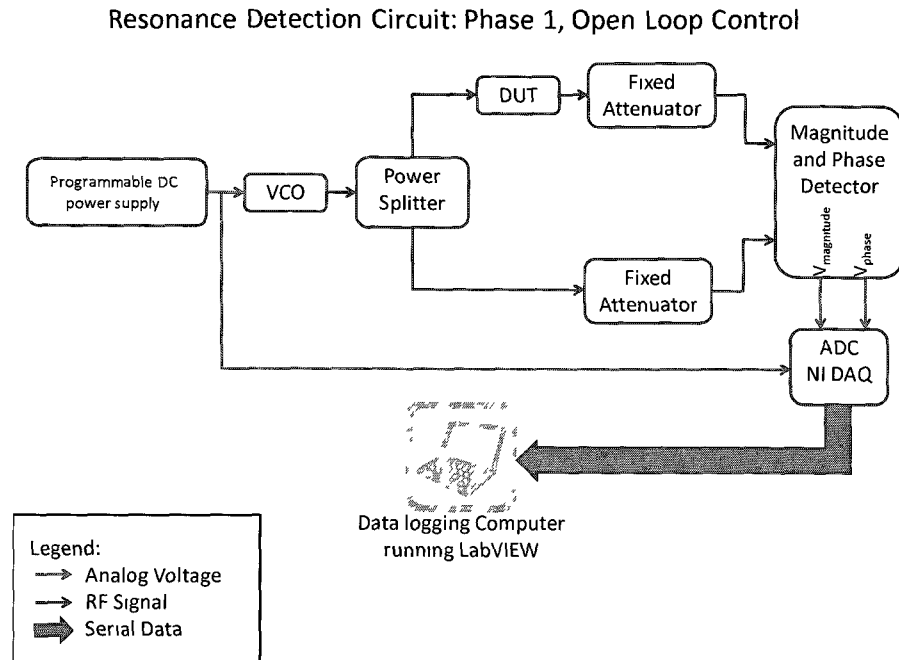


Figure 5.2 - Block diagram for the resonance detection circuit, Phase 1

We knew from experimentation with the VNA, that our system would resonate between 1 GHz to 1.5 GHz. We choose a ROS-1700W+ surface mount voltage controlled oscillator (VCO) from Mini-Circuits. This VCO had a frequency range of 770 to 1700 MHz, covering the resonant frequencies we observed with our VNA.

The DUT is the location of where our probe loop will be physically connected to the circuit. We represented the probe/sensor loop resonant circuit by connecting a surface mount 18 nH inductor and 1 pF capacitor in series. This configuration reduced complexity while preserving functionality, and enabled testing/debugging of the entire circuit.

The receiver portion of the circuit consists of an Analog Devices low frequency to 2.7 GHz magnitude and phase detector integrated circuit. It requires two signals, a reference signal (at -30dBm) and measurement signal (0 to -60 dBm), for proper

operation (similar to VNA shown in Figure 5.1). The two required signals are produced by passing the output from the VCO (+8dBm) directly to a Mini-circuits SYPS-252+ power splitter. The output from the VCO is reduced to -30 dBm by 5 dBm from the power splitter and two fixed attenuators (Mini-circuits GAT-15+ (-15dBm) and GAT-20+ (-20 dBm)). The measurement signal from the passive DUT is reduced to -3dBm with an 8dBm attenuator (Mini-circuits GAT-8+).

The National Instrument DAQ-6009 was used to measure the analogue voltages representative of magnitude, phase, and the input voltage to the VCO. This data was transferred via USB to a computer running LabVIEW for processing.

In the next design, we resolved the problem of VCO input noise by replacing the DC power supply with a function generator and amplifying circuit. Figure 5.3 shows the block diagram for the second version of the resonance detection circuit.

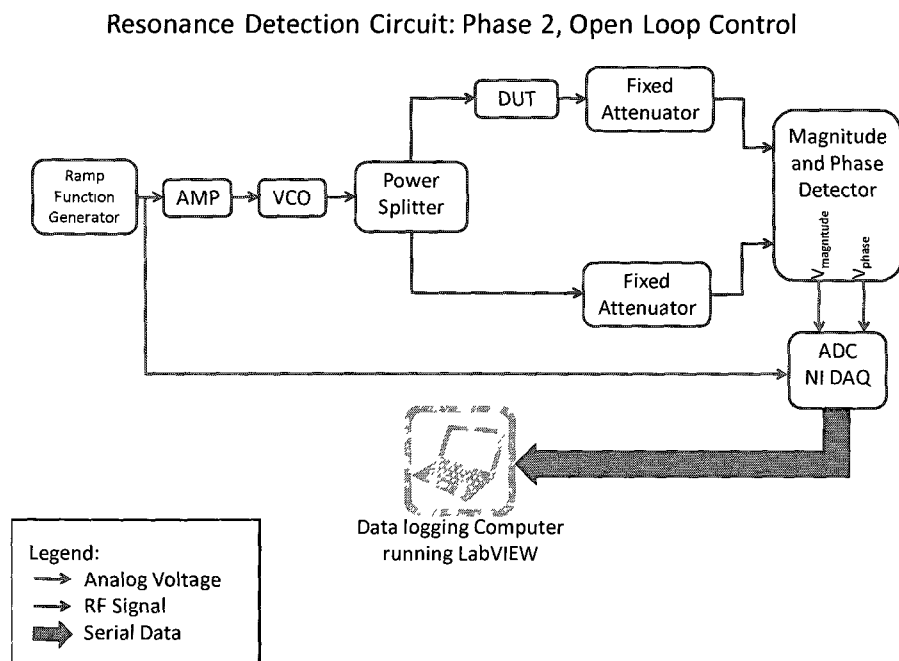


Figure 5.3 - Block diagram for the resonance detection circuit, Phase 2

We used a BK Precision 4084 function generator to produce a 5 Vpp sawtooth waveform with a 2.5 VDC offset. This signal was amplified with a Fairchild Semiconductor

LM358 operational amplifier configured as non-inverting amplifier to produce a 0 to 24 V sawtooth waveform. Phase 2 removed much of the VCO noise from the previous iteration, although it yielded difficulties in signal processing. The next upgrade we determined was to produce a better control architecture for easier signal processing, and thus better evaluation of system performance.

We exchanged Phase 2's open loop control design for closed loop control in Phase 3. Figure 5.4 shows the modifications in block diagram form for Phase 3.

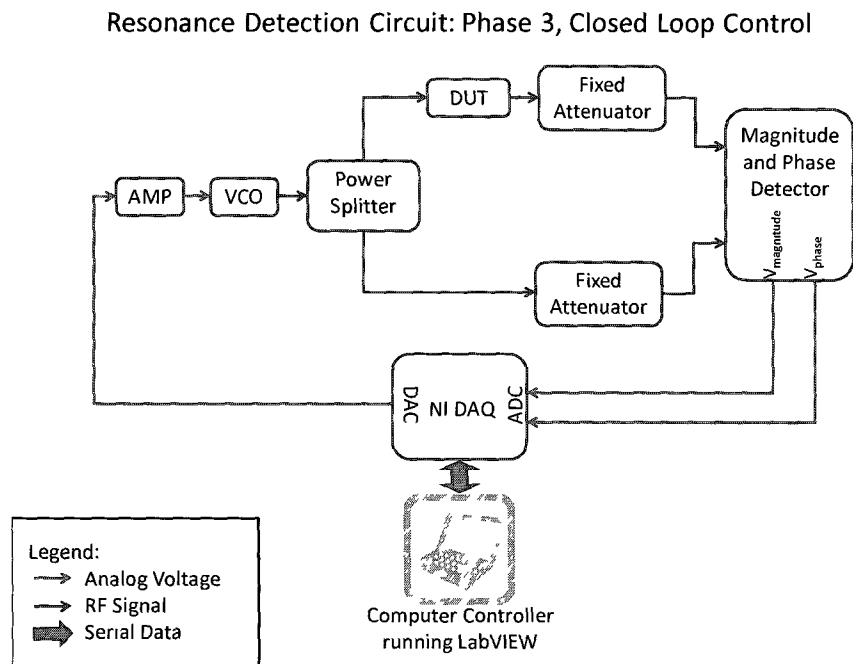
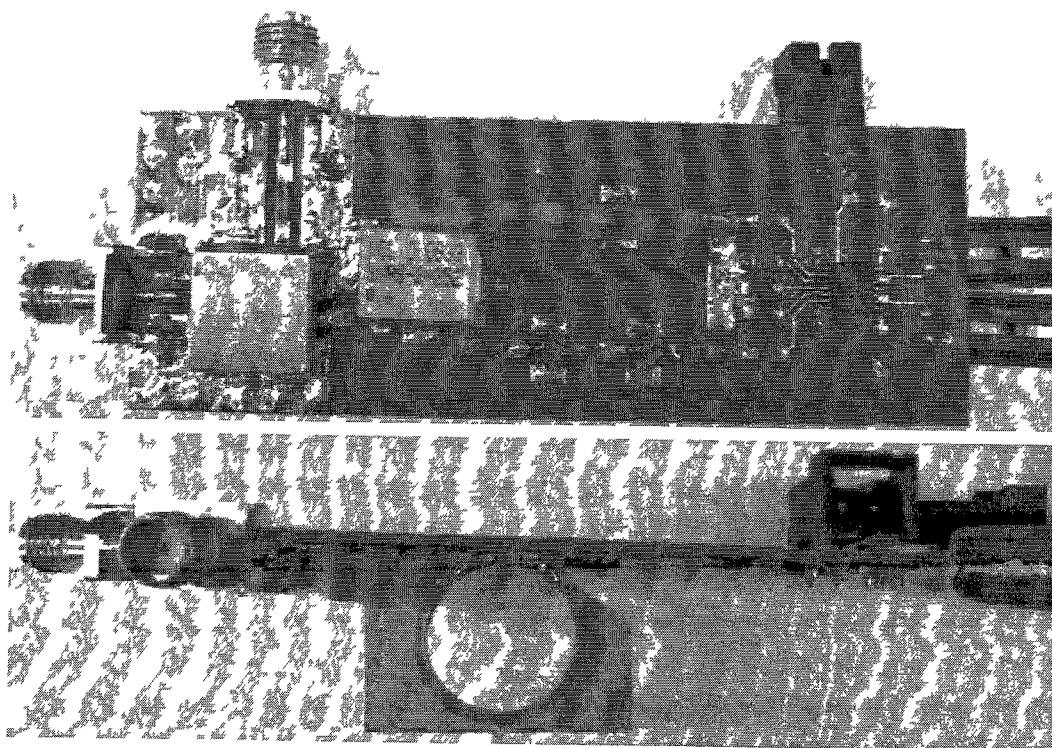


Figure 5.4 - Block diagram of the resonance detection circuit, Phase 3

We accomplished this by using an open digital to analog converter (DAC) port on the USB NI-DAQ. This allowed for closed loop control, real-time system observation, and the ability to hold the input voltage to the VCO constant for statistical noise analysis. Unfortunately, the DAC was only capable of producing an output voltage up to 5 VDC; therefore the circuit still required the use of the amplifying circuit. The amplifying circuit is yet another location for noise to corrupt the tuning voltage of the VCO.

Once Phase 3 was assembled and proper operation was verified, the discrete component resonant circuit was removed and the probe loop was attached. The sensor loop we tested was a 1.5 pF discrete capacitor with a single turn inductor made of 30 AWG wire, insulated from the 4 flute carbide end mill tool bit with 88.9  $\mu\text{m}$  of stand-off distance. The probe loop used to excite the sensor loop was the 14.53mm loop shown in Figure 2.6. For comparison, Figure 5.6 shows the magnitude and phase response measured with Agilent Technologies VNA using the aforementioned components. The probe loop mounted to our Resonance Detection circuit was an altered version of the 14.53mm loop. Figure 5.5 shows two views of the detection circuit built on 1 mm thick FR-4 (the bottom layer is a continuous ground layer).



**Figure 5.5 - Front and Top View of actual Detection Circuit and Probe Loop**

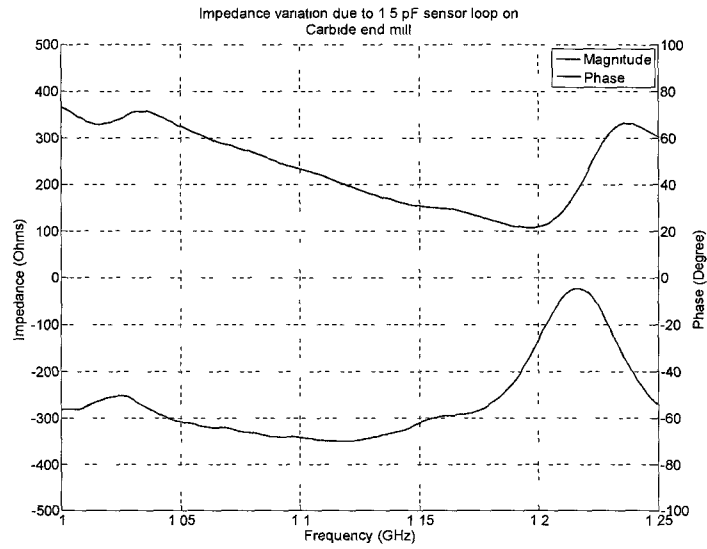


Figure 5.6 - VNA captured magnitude and phase plot

The magnitude and phase response measured with our resonance detection is shown in Figure 5.7 and Figure 5.8, respectively. These plots show the average and standard deviation of 1000 samples at each individual frequency step at a sampling frequency of 1 kHz.

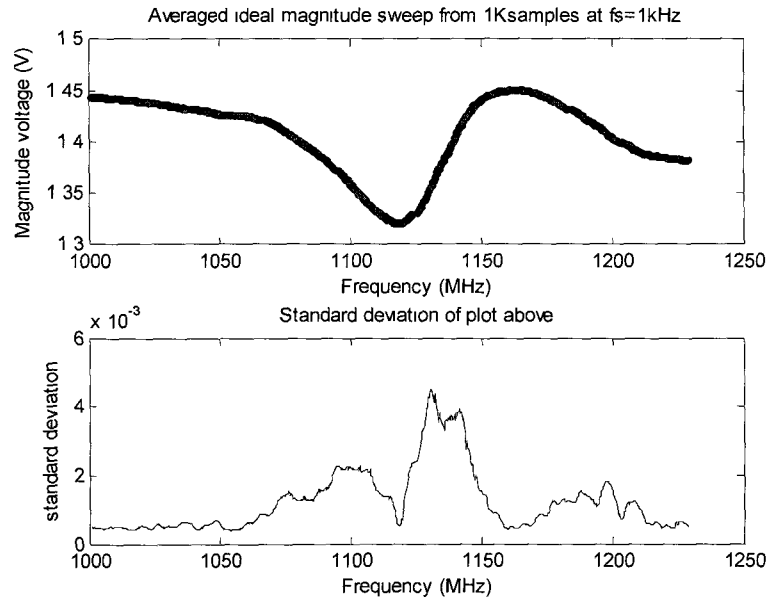


Figure 5.7 – Averaged magnitude plot and corresponding standard deviation



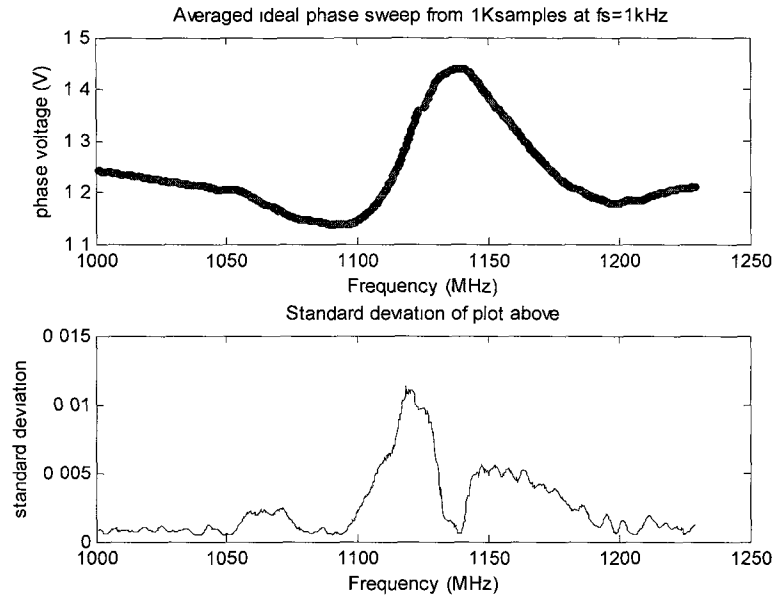


Figure 5.8 – Averaged phase plot and corresponding standard deviation

Our circuit’s resonant frequency was only 80 MHz away from that measured with Agilent Technologies VNA and this error was minimal when considering the frequency range we are working in. The main observation to take from Figure 5.6 through Figure 5.8 was the similarity between the shape of the magnitude and phase response. This similarity verifies we have built a working resonance detection circuit which was capable of achieving results comparable to a commercially available VNA.

### **5.3 CHAPTER SUMMARY**

In this chapter, we addressed the commercially available VNA and its functionality. Then we discussed how we recreated the VNA in discrete integrated circuits and the design process used to reduce noise and improve measurement quality. Finally, we compared results for identical resonant circuit systems with both systems and showed that the in-house fabricated circuit’s performance was comparable to the VNA.

## CHAPTER 6

### CONCLUSIONS

Using a capacitively terminated sensor loop we achieved the measurement of strain in a cylindrical aluminum structure, wirelessly with a stationary probe loop through electromagnetic resonance. The prototype system used a parallel plate type capacitor and exhibited a 2.4943 (MHz/MHz)/ $\epsilon$  sensitivity.

It was found that a 12.7 mm inner diameter circular probe loop manufactured on 1.27 mm FR-4 with a copper trace cross-section of 18  $\mu\text{m}$  by 0.83 mm, yielded no self resonances for the 1 to 2 GHz frequency regime. It was determined that this antenna produced the highest quality factor when the sensor loop to probe loop distance was 0.69 mm and the circuit contained no resistive components.

We determined that the strain sensor, when mounted on high strength steel or cemented carbide tool bits, should have an undeformed capacitance of less than 1 pF for the greatest frequency change with capacitance. We concluded there is degradation in the quality factor of the resonance for insert materials with lower electrical resistivity. We were able to reduce this effect by placing a shorted loop made of copper foil, using silver paste to facilitate the electrical connection to the tool bit, below the sensor loop. Another method we found to increase the quality factor of the resonance was to increase the dielectric stand-off distance between the sensor loop and the tool bit to 177.8  $\mu\text{m}$ . We also found that there is a response due to the spatial location of the sensor loop and it is greatest when the motion is along the axis of the probe loop feed.

Through computer simulation, we found that the interdigitated comb capacitor structure would be most sensitive when the fingers are oriented parallel to the direction of the applied strain.

Finally, we designed, assembled and verified operation for a resonance detection circuit that yielded results comparable to a commercially available vector network analyzer.

## CHAPTER 7

### FUTURE WORK

This chapter describes future work that the author believed is important for further investigation in to this topic. We begin with an alternative approach to sensor design, in which the flexible circuit manufactured interdigitated comb capacitor structure would be replaced with off-the-shelf multilayer capacitors. Then we discuss trade-offs and issues with methods for the attachment of the sensor loop to the detection circuitry. Finally, we detail the final iteration of the detection circuit which contains all of the required circuitry.

#### 7.1 SENSOR DESIGN

Another capacitor design that could be used as strain sensor was a surface mount technology (SMT) multilayer ceramic capacitor (MLCC). These capacitors are made for population of printed circuit boards, but contain capacitive structures that may be exploited to detect strain. Figure 7.1 shows a MLCC package and its internal design.

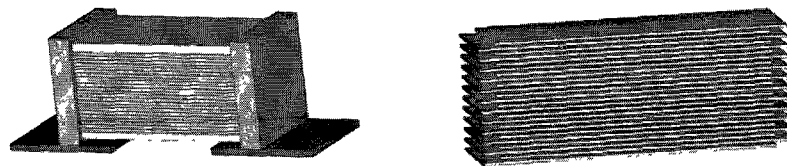


Figure 7.1 - SMT MLCC and internal design (21)

With further testing and evaluation, we can determine if these off-the-shelf SMT capacitors offer higher strain sensitivity than our flexible circuit fabricated sensors.

## 7.2 PROBE/DETECTION CIRCUITRY IMPLEMENTATION

The DUT portion of the circuit consists of the probe loop and sensor loop. From the view point of the detection circuit, the only variations that could occur in this section were the mounting direction of the probe loop. The probe loop can either be mounted perpendicular or parallel to the ground plane. Figure 7.2 and Figure 7.3 show a CAD model with the loop mounted parallel and perpendicular, respectively.

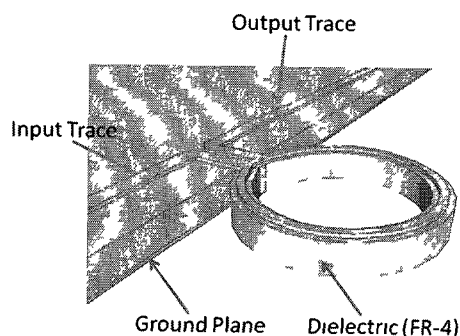


Figure 7.2 - Loop mounted parallel to ground plane

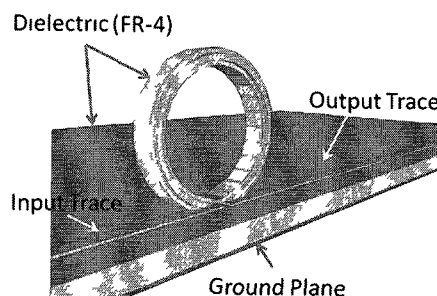


Figure 7.3 - Loop mounted perpendicular to ground plane

The positive effects of mounting the loop parallel to ground are we will be able to build it during the printed circuit board manufacturing process and shielding the input and output trace are easier. A negative effect of this design is the coupling that occurs between the input/output traces and ground plane. The perpendicular design would have to be attached after the main board is produced. This means reproducibility as well as shielding the input and output traces is difficult, yet it eliminates the coupling effects with the ground plane. Further experimentation and simulation is required to determine how profound the probe loop orientation is on system performance.

### 7.3 DETECTION CIRCUITY DESIGN

The final iteration of the resonance detection circuit is Phase 4. It simplifies the overall design while combining all of the positive effects of the previous versions. Figure 7.4 shows the block diagram view of Phase 4.

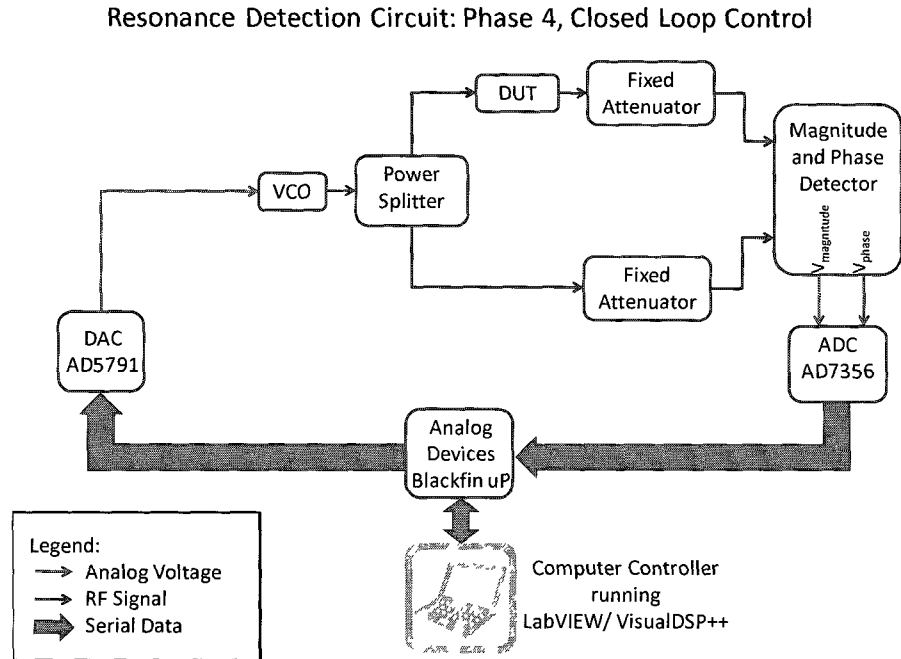


Figure 7.4 - Block diagram for resonance detection circuit, Phase 4, Final Design

This design replaces the 12-bit DAC of the NI-DAQ with an AD5721 20-bit DAC from Analog Devices. This integrated circuit (IC) accepts rails of  $\pm 14$  V which is sufficient for a VCO with a maximum tuning voltage of 12 V. It is also has a factory calibrated 1 ppm noise specification and is capable of producing 1 Msample/sec. We also replaced the 14-bit ADC of the NI-DAQ with an AD7356 differential input, dual simultaneous sampling 12-bit SAR ADC from Analog Devices. This IC is capable of taking a snap shot in time of both magnitude and phase simultaneously while also having a high enough sampling rate to characterize a 1 MHz sawtooth input waveform to the VCO. Both of these chips

will be actuated via an Analog Devices Site Development Platform which contains a Blackfin microprocessor (uP), programmed in LabVIEW/VisualDSP++.

## LIST OF REFERENCES

1. **Delio, T.S.** *Method for Controlling Chatter in a Machine Tool*. 5,170,358 United States of America, December 8, 1992.
2. **Boylestad, Robert.** *Introductory Circuit Analysis*. New Jersey : Prentice Hall, 2003.
3. *Resonantly Coupled Antennas for Passive Sensors*. **Rindorf, Lars, Lading, Lars and Olav, Breinbjerg**. 2008. IEEE Sensors. pp. 1611-1614.
4. **Pilkey, Walter and Pilkey, Orrin.** *Mechanics of Solids*. New York, NY : Quantum Publishers, 1974.
5. *Design and characterization of a passive wireless strain sensor*. **Jia, Y, et al., et al.** 2006, Measurement Science Technology, pp. 2869-2876.
6. **Chuang, J, Thomson, D and Bridges, G.** *Embeddable wireless strain sensor based on resonant rf cavities*. s.l. : American Institute of Physics, 2005. pp. 1-7.
7. *A wireless batch sealed absolute capacitive pressure sensor*. **Akar, Orhan, Akin, Tayfun and Najafi, Khalil**. s.l. : Elsevier, 2001, Elsevier: Sensors and Actuators, pp. 29-38.
8. *A resonant printed-circuit sensor for remote query monitoring of environmental parameters*. **Ong, K and Grimes, C.** 2000, Smart Material Structures, pp. 421-428.
9. *Resonantly Coupled Antennas for Passive Sensors*. **Rindorf, Lars, Lading, Lars and Breinbjerg, Olav**. 2008. IEEE Sensors. pp. 1611-1614.
10. **Lacoste, Robert.** VECTOR'SoC: A 1 GHz Vectorial Network Analyzer. *psocdeveloper.com*. [Online] 2002. [Cited: 9 [http://www.psocdeveloper.com/uploads/tx\\_piapappnote/an2090.pdf](http://www.psocdeveloper.com/uploads/tx_piapappnote/an2090.pdf), 2010.]
11. *Design and Optimization of Resonance-Based Efficient Wireless Power Delivery Systems for Biomedical Implants*. **RamRakhyani, Anil, Mirabbasi, Shahriar and Chiao, Mu**. s.l. : IEEE, 2011. IEEE Transactions on Biomedical Circuits and Systems. pp. 48-63.
12. **Storr, Wayne.** Inductors in Parallel. *Electronics-Tutorials*. [Online] July 2011. [Cited: July 27, 2011.] <http://www.electronics-tutorials.ws/inductor/parallel-inductors.html>.
13. **Wang, Ruye.** Quality Factor, Peak Frequency and Bandwidth. *Harvey Mudd College; Electrical Engineering Class E84*. [Online] 06 28, 2011. [Cited: 07 26, 2011.] <http://fourier.eng.hmc.edu/e84/lectures/ch3/node7.html>.
14. **Boylestad.** *Introductory Circuit Analysis*. s.l. : Prentice Hall, 2002.
15. Q and bandwidth of a resonant circuit. *All about Circuits*. [Online] [http://www.allaboutcircuits.com/vol\\_2/chpt\\_6/6.html](http://www.allaboutcircuits.com/vol_2/chpt_6/6.html).
16. **Vulcan.** Typical Material Stack up for Double-Sided Flex Circuits. *Vulcan Electric*. [Online] [Cited: 6 2, 2011.] [http://www.vulcanelectric.com/downloads/SU\\_DoubleLayer.pdf](http://www.vulcanelectric.com/downloads/SU_DoubleLayer.pdf).
17. *Measurement of Stray Capacitance Due to Solder Flux Residue on Radio Frequency Circuit Boards*. **Heutmaker, Michael, Fletcher, Linda and Sohn, John**. s.l. : IEEE, 1995. MTT-S Symposium. pp. 105-109.
18. **Desfosses, Bennett.** *An Improved Power Threshold Method for Estimating Tool Wear During Milling*. Durham, NH : s.n., 2007.



19. **Menon, Devdas and Sengupta, Amlan.** Prestressed Concrete Structures. [Online] [Cited: 06 19, 2011.] [http://nptel.iitm.ac.in/courses/IIT-MADRAS/PreStressed\\_Concrete\\_Structures/pdf/5\\_Analysis\\_Design\\_for\\_Shear\\_Torsion/Section5.4.pdf](http://nptel.iitm.ac.in/courses/IIT-MADRAS/PreStressed_Concrete_Structures/pdf/5_Analysis_Design_for_Shear_Torsion/Section5.4.pdf).
20. **Hiebel, Michael.** *Fundamentals of Vector Network Analysis*. München : Rohbe & Schwarz GmbH & Co. KG, 2007.
21. **McMorrow, Scott, Weir, Steve and Zanella, Fabrizio.** Using Full Wave Solvers for Practical Analysis of Capacitor. *CST*. [Online] [Cited: 6 6, 2011.] [http://www.cst.com/Content/Documents/Articles/article402/FullWaveCapacitorModeling\\_CST%20users%20forum.pdf](http://www.cst.com/Content/Documents/Articles/article402/FullWaveCapacitorModeling_CST%20users%20forum.pdf).

## **APPENDIX**

## MathCAD: Calculations

### Proof-of-concept Matlab Variable Derivation

The definition of the resonant frequency based on its inductance and capacitance is

$$f = \frac{1}{2\pi\sqrt{L\cdot C}}$$

The unstrained frequency in MHz of the circuit is

$$f_0 := 475.1875$$

We can solve the original equation for the LC product

guess

$$x := 0.000000000000000001$$

Given

$$f_0 = \frac{1}{2\pi\sqrt{x}}$$

$$\text{Find}(x) = 1.121787 \times 10^{-7}$$

$$LC_{\text{prod}} := 1.121787 \times 10^{-7}$$

## Probe Diameter Section

### Quality Factor

$$f_{r\_0.573in} := 1.8019948125\text{GHz} \quad f_{l\_0.573in} := 1.7869963125\text{GHz} \quad f_{u\_0.573in} := 1.81980553125\text{GHz}$$

$$Q_{0.573in} := \frac{f_{r\_0.573in}}{f_{u\_0.573in} - f_{l\_0.573in}}$$

$$Q_{0.573in} = 54.923$$

$$f_{r\_0.594in} := 1.770123\text{GHz} \quad f_{l\_0.594in} := 1.75418709375\text{GHz} \quad f_{u\_0.594in} := 1.79168334375\text{GHz}$$

$$Q_{0.594in} := \frac{f_{r\_0.594in}}{f_{u\_0.594in} - f_{l\_0.594in}}$$

$$Q_{0.594in} = 47.208$$

$$f_{r\_0.612in} := 1.7644985625\text{GHz} \quad f_{l\_0.612in} := 1.7457504375\text{GHz} \quad f_{u\_0.612in} := 1.788871125\text{GHz}$$

$$Q_{0.612in} := \frac{f_{r\_0.612in}}{f_{u\_0.612in} - f_{l\_0.612in}}$$

$$Q_{0.612in} = 40.92$$

### Inductance

$$f_{r\_0.573in} = \frac{1}{2\pi\sqrt{X_{tot}}}$$

$$C_{meas} := 0.856 \cdot 10^{-12}$$

$$X_{tot\_0.573in} := 7.80069307 \cdot 10^{-21}$$

$$L_{0.573in} := \frac{X_{tot\_0.573in}}{C_{meas}}$$

$$L_{0.573in} = 9.113 \times 10^{-9} \text{ H}$$

$$f_{r\_0.594in} = \frac{1}{2\pi\sqrt{X_{tot}}}$$

$$X_{tot\_0.594in} := 8.23167927 \cdot 10^{-21}$$

$$L_{0.594in} := \frac{X_{tot\_0.594in}}{C_{meas}}$$

$$L_{0.594in} = 9.616 \times 10^{-9} \text{ H}$$

$$f_{r\_0.612in} = \frac{1}{2\pi\sqrt{X_{tot}}}$$

$$X_{tot\_0.612in} = 8.31143369 \cdot 10^{-21}$$

$$L_{0.612in} = \frac{X_{tot\_0.612in}}{C_{meas}}$$

$$L_{0.612in} = 9.71 \times 10^{-9} \text{ H}$$

### Resistance

$$R_{0.573in} = \frac{1}{Q_{0.573in}} \sqrt{\frac{L_{0.573in}}{C_{meas}}}$$

$$R_{0.573in} = 1.879 \text{ } \Omega$$

$$R_{0.594in} = \frac{1}{Q_{0.594in}} \sqrt{\frac{L_{0.594in}}{C_{meas}}}$$

$$R_{0.594in} = 2.245 \text{ } \Omega$$

$$R_{0.612in} = \frac{1}{Q_{0.612in}} \sqrt{\frac{L_{0.612in}}{C_{meas}}}$$

$$R_{0.612in} = 2.603 \text{ } \Omega$$

### Self Inductance (Probe Loop)

Wire's radius

$$R_{wire} = 6.824 \cdot 10^{-5} \text{ m}$$

Radius of the loop

$$r_{0.573dloop} = \left( 0.286 + \frac{0.032}{2} \right) \cdot in$$

$$r_{0.594dloop} = \left( 0.297 + \frac{0.032}{2} \right) \cdot in$$

$$r_{0.612dloop} = \left( 0.306 + \frac{0.032}{2} \right) \cdot in$$

$$L_{0.573dloop} = \mu_0 r_{0.573dloop} \left( \ln \left( \frac{8 \cdot r_{0.573dloop}}{R_{wire}} \right) - 2 \right)$$

$$L_{0.573dloop} = 4.628 \times 10^{-8} \text{ H}$$

$$L_{0.594dloop} = \mu_0 r_{0.594dloop} \left( \ln \left( \frac{8 \cdot r_{0.594dloop}}{R_{wire}} \right) - 2 \right)$$

$$L_{0.594dloop} = 4.833 \times 10^{-8} \text{ H}$$

$$L_{0.612dloop} = \mu_0 r_{0.612dloop} \left( \ln \left( \frac{8 \cdot r_{0.612dloop}}{R_{wire}} \right) - 2 \right)$$

$$L_{0.612dloop} = 5.001 \times 10^{-8} \text{ H}$$

### Self Inductance (Sensor Loop)

Wire's radius

$$\text{thick} := 0.0021\text{in}$$

$$\text{height} := 0.05\text{in}$$

$$a_{\text{sens}} := \text{thick} \cdot \text{height} \quad \left( \frac{a_{\text{sens}}}{\pi} \right)^{.5} = 1.468 \times 10^{-4} \text{m}$$

$$R_{\text{wiresensor}} := 1.468 \times 10^{-4} \text{m}$$

Radius of the loop

$$r_{\text{sensorloop}} := 0.25\text{in} + (51 + 25 + 25 + 76 + 25) \cdot 10^{-6} \text{m} + 0.0015\text{in}$$

$$L_{\text{sensorloop}} := \mu_0 \cdot r_{\text{sensorloop}} \cdot \left( \ln \left( \frac{8 \cdot r_{\text{sensorloop}}}{R_{\text{wiresensor}}} \right) - 2 \right)$$

$$L_{\text{sensorloop}} = 3.216 \times 10^{-8} \text{H}$$

### Mutual Inductance

#### 0.573 Diameter loop

$$a := r_{0.573\text{dloop}} \quad b := r_{\text{sensorloop}} \quad d := \left( r_{0.573\text{dloop}} - \frac{0.032}{2} \text{in} \right) - (r_{\text{sensorloop}} + 0.0015\text{in})$$

$$k_{0.573\text{dloop}} := \left[ \frac{4 \cdot a \cdot b}{(a + b)^2 + d^2} \right]^{0.5} \quad k_{0.573\text{dloop}} = 996.134 \times 10^{-3}$$

Elliptic integrals evaluated in Matlab

$$K_{\text{max}} := 4.1671$$

$$E := 1.0071$$

$$M_{0.573\text{dloop}} := \mu_0 (a \cdot b)^{0.5} \cdot \left[ \left( \frac{2}{k_{0.573\text{dloop}}} - k_{0.573\text{dloop}} \right) \cdot K - \frac{2}{k_{0.573\text{dloop}}} \cdot E \right]$$

$$M_{0.573\text{dloop}} = 19.598 \times 10^{-9} \text{H}$$

#### 0.594 Diameter loop

$$a_{\text{max}} := r_{0.594\text{dloop}} \quad b_{\text{max}} := r_{\text{sensorloop}} \quad d_{\text{max}} := \left( r_{0.594\text{dloop}} - \frac{0.032}{2} \text{in} \right) - (r_{\text{sensorloop}} + 0.0015\text{in})$$

$$k_{0.594\text{dloop}} := \left[ \frac{4 \cdot a \cdot b}{(a + b)^2 + d^2} \right]^{0.5} \quad k_{0.594\text{dloop}} = 993.6475 \times 10^{-3}$$

Elliptic integrals evaluated in Matlab

$$K_{\text{max}} := 3.9204$$

$$E_{\text{max}} := 1.0109$$

$$M_{0.594\text{dloop}} = \mu_0 \cdot (a \cdot b)^{0.5} \cdot \left[ \left( \frac{2}{k_{0.594\text{dloop}}} - k_{0.594\text{dloop}} \right) \cdot K - \frac{2}{k_{0.594\text{dloop}}} \cdot E \right]$$

$$M_{0.594\text{dloop}} = 17.834 \times 10^{-9} \text{ H}$$

### 0.612 Diameter loop

$$a_w = r_{0.612\text{dloop}} \quad b_w = r_{\text{sensorloop}} \quad d_w = \left( r_{0.612\text{dloop}} - \frac{0.032}{2} \text{ in} \right) - (r_{\text{sensorloop}} + 0.0015 \text{ in})$$

$$k_{0.612\text{dloop}} = \left[ \frac{4 \cdot a \cdot b}{(a + b)^2 + d^2} \right]^{0.5} \quad k_{0.612\text{dloop}} = 991.2271 \times 10^{-3}$$

Elliptic integrals evaluated in Matlab  $K_w = 3.7604$   $E_w = 1.0143$

$$M_{0.612\text{dloop}} = \mu_0 \cdot (a \cdot b)^{0.5} \cdot \left[ \left( \frac{2}{k_{0.612\text{dloop}}} - k_{0.612\text{dloop}} \right) \cdot K - \frac{2}{k_{0.612\text{dloop}}} \cdot E \right]$$

$$M_{0.612\text{dloop}} = 16.73 \times 10^{-9} \text{ H}$$

### Estimated Total Inductance

$$L_{0.573\text{total}} = \left( \frac{L_{0.573\text{dloop}} \cdot L_{\text{sensorloop}} - M_{0.573\text{dloop}}^2}{L_{0.573\text{dloop}} + L_{\text{sensorloop}} + M_{0.573\text{dloop}}} \right)$$

+

$$L_{0.573\text{total}} = 1.127 \times 10^{-8} \text{ H}$$

$$L_{0.594\text{total}} = \left[ \frac{L_{0.594\text{dloop}} \cdot L_{\text{sensorloop}} - M_{0.594\text{dloop}}^2}{(L_{0.594\text{dloop}} + L_{\text{sensorloop}}) + M_{0.594\text{dloop}}} \right]$$

$$L_{0.594\text{total}} = 1.257 \times 10^{-8} \text{ H}$$

$$L_{0.612\text{total}} = \left[ \frac{L_{0.612\text{dloop}} \cdot L_{\text{sensorloop}} - M_{0.612\text{dloop}}^2}{(L_{0.612\text{dloop}} + L_{\text{sensorloop}}) + M_{0.612\text{dloop}}} \right]$$

$$L_{0.612\text{total}} = 1.343 \times 10^{-8} \text{ H}$$

### Coupling coefficient

$$k_{0.573} := \frac{M_{0.573\text{dloop}}}{\sqrt{L_{0.573\text{dloop}} \cdot L_{\text{sensorloop}}}} \quad \boxed{k_{0.573} = 0.508}$$

$$k_{0.594} := \frac{M_{0.594\text{dloop}}}{\sqrt{L_{0.594\text{dloop}} \cdot L_{\text{sensorloop}}}} \quad \boxed{k_{0.594} = 0.452}$$

$$k_{0.612} := \frac{M_{0.612\text{dloop}}}{\sqrt{L_{0.612\text{dloop}} \cdot L_{\text{sensorloop}}}} \quad \boxed{k_{0.612} = 0.417}$$

### Separation Area

$$r_{\text{out}} := \left( r_{0.573\text{dloop}} - \frac{0.032}{2} \text{in} \right) \quad r_{\text{in}} := (r_{\text{sensorloop}} + 0.0015\text{in})$$

$$A_{\text{sep}0.573} := \pi \cdot r_{\text{out}}^2 - \pi \cdot r_{\text{in}}^2 \quad \boxed{A_{\text{sep}0.573} = 27.767 \text{mm}^2}$$

$$r_{\text{out}} := \left( r_{0.594\text{dloop}} - \frac{0.032}{2} \text{in} \right)$$

$$A_{\text{sep}0.594} := \pi \cdot r_{\text{out}}^2 - \pi \cdot r_{\text{in}}^2 \quad \boxed{A_{\text{sep}0.594} = 40.765 \text{mm}^2}$$

$$r_{\text{out}} := \left( r_{0.612\text{dloop}} - \frac{0.032}{2} \text{in} \right)$$

$$A_{\text{sep}0.612} := \pi \cdot r_{\text{out}}^2 - \pi \cdot r_{\text{in}}^2 \quad \boxed{A_{\text{sep}0.612} = 51.765 \text{mm}^2}$$

### Resistance of probe loop

Assumption: magnetic permeability of core material is air  $\mu_r := 1$

$$\rho_{\text{copper}} := 1.68 \cdot 10^{-8} \Omega \cdot \text{m} \quad \sigma_{\text{copper}} := 5.96 \cdot 10^7 \frac{\text{S}}{\text{m}}$$

$$\mu := \mu_r \cdot \mu_0 \quad w := 0.032\text{in} \quad h := 18 \cdot 10^{-6} \text{m}$$



**Probe 0.573 in**

$$\text{Len}_{\text{probe0.573}} := 2 \cdot \pi \cdot r_{0.573} \cdot d_{\text{loop}} \quad \omega_{0.573\text{in}} := 2\pi \cdot f_r_{0.573\text{in}}$$

$$\delta_{0.573} := \sqrt{\frac{2}{\omega_{0.573\text{in}} \cdot \mu \cdot \sigma_{\text{copper}}}}$$

$$R_{\text{probe0.573}} := \frac{\rho_{\text{copper}} \cdot \text{Len}_{\text{probe0.573}}}{w \cdot \delta_{0.573} \cdot \left(1 - e^{\frac{-h}{\delta_{0.573}}}\right)}$$

$$R_{\text{probe0.573}} = 0.649 \Omega$$

**Probe 0.594 in**

$$\text{Len}_{\text{probe0.594}} := 2 \cdot \pi \cdot r_{0.594} \cdot d_{\text{loop}} \quad \omega_{0.594\text{in}} := 2\pi \cdot f_r_{0.594\text{in}}$$

$$\delta_{0.594} := \sqrt{\frac{2}{\omega_{0.594\text{in}} \cdot \mu \cdot \sigma_{\text{copper}}}}$$

$$R_{\text{probe0.594}} := \frac{\rho_{\text{copper}} \cdot \text{Len}_{\text{probe0.594}}}{w \cdot \delta_{0.594} \cdot \left(1 - e^{\frac{-h}{\delta_{0.594}}}\right)}$$

$$R_{\text{probe0.594}} = 0.666 \Omega$$

**Probe 0.612 in**

$$\text{Len}_{\text{probe0.612}} := 2 \cdot \pi \cdot r_{0.612} \cdot d_{\text{loop}} \quad \omega_{0.612\text{in}} := 2\pi \cdot f_r_{0.612\text{in}}$$

$$\delta_{0.612} := \sqrt{\frac{2}{\omega_{0.612\text{in}} \cdot \mu \cdot \sigma_{\text{copper}}}}$$

$$R_{\text{probe0.612}} := \frac{\rho_{\text{copper}} \cdot \text{Len}_{\text{probe0.612}}}{w \cdot \delta_{0.612} \cdot \left(1 - e^{\frac{-h}{\delta_{0.612}}}\right)}$$

$$R_{\text{probe0.612}} = 0.684 \Omega$$

## Resistance of Sensor Loop

$$Len_{\text{sensor}} := 2 \cdot \pi r_{\text{sensorloop}}$$

Assumption: magnetic permeability of core material is copper  $\mu_{\text{core}} := 0.999994$

$$\sigma_{\text{copper}} := 5.96 \cdot 10^7 \frac{\text{S}}{\text{m}} \quad \mu_{\text{core}} := \mu_r \cdot \mu_0 \quad w_{\text{core}} := 0.0021 \text{in} \quad h_{\text{core}} := 0.05 \text{in}$$

With fres for 0.573in probe loop

$$\delta_{\text{sensor}0.573} := \sqrt{\frac{2}{\omega_{0.573 \text{in}} \cdot \mu \cdot \sigma_{\text{copper}}}}$$

$$R_{\text{sensorwith}0.573 \text{in}} := \frac{\rho_{\text{copper}} \cdot Len_{\text{sensor}}}{w \cdot \delta_{\text{sensor}0.573} \cdot \left(1 - e^{\frac{-h}{\delta_{\text{sensor}0.573}}}\right)}$$

$$R_{\text{sensorwith}0.573 \text{in}} = 8.492 \Omega$$

With fres for 0.594in probe loop

$$\delta_{\text{sensor}0.594} := \sqrt{\frac{2}{\omega_{0.594 \text{in}} \cdot \mu \cdot \sigma_{\text{copper}}}}$$

$$R_{\text{sensorwith}0.594 \text{in}} := \frac{\rho_{\text{copper}} \cdot Len_{\text{sensor}}}{w \cdot \delta_{\text{sensor}0.594} \cdot \left(1 - e^{\frac{-h}{\delta_{\text{sensor}0.594}}}\right)}$$

$$R_{\text{sensorwith}0.594 \text{in}} = 8.417 \Omega$$

With fres for 0.612in probe loop

$$\delta_{\text{sensor}0.612} := \sqrt{\frac{2}{\omega_{0.612 \text{in}} \cdot \mu \cdot \sigma_{\text{copper}}}}$$

$$R_{\text{sensorwith}0.612 \text{in}} := \frac{\rho_{\text{copper}} \cdot Len_{\text{sensor}}}{w \cdot \delta_{\text{sensor}0.612} \cdot \left(1 - e^{\frac{-h}{\delta_{\text{sensor}0.612}}}\right)}$$

$$R_{\text{sensorwith}0.612 \text{in}} = 8.403 \Omega$$

### Resistance of Insert Material

$$Len_{insert} := 2 \cdot \pi \frac{0.5in}{2}$$

With fres for 0.573in probe loop

$$\frac{w}{w} := \delta_{sensor0.573} \quad \frac{h}{w} := h + \delta_{sensor0.573}$$

$$R_{insert0.573} := \frac{\rho_{copper} \cdot Len_{insert}}{w \cdot \delta_{sensor0.573} \cdot \left(1 - e^{\frac{-h}{\delta_{sensor0.573}}}\right)}$$

$$R_{insert0.573} = 284.197 \Omega$$

With fres for 0.594in probe loop

$$\frac{w}{w} := \delta_{sensor0.594} \quad \frac{h}{w} := h + \delta_{sensor0.594}$$

$$R_{insert0.594} := \frac{\rho_{copper} \cdot Len_{insert}}{w \cdot \delta_{sensor0.594} \cdot \left(1 - e^{\frac{-h}{\delta_{sensor0.594}}}\right)}$$

$$R_{insert0.594} = 279.171 \Omega$$

With fres for 0.612in probe loop

$$\frac{w}{w} := \delta_{sensor0.612} \quad \frac{h}{w} := h + \delta_{sensor0.612}$$

$$R_{insert0.612} := \frac{\rho_{copper} \cdot Len_{insert}}{w \cdot \delta_{sensor0.612} \cdot \left(1 - e^{\frac{-h}{\delta_{sensor0.612}}}\right)}$$

$$R_{insert0.612} = 278.284 \Omega$$

### Height of inductance loop on insert

$$\text{sensor\_innerR} := r_{\text{sensorloop}} - 0.0015 \text{in}$$

$$r_0 := \text{sensor\_innerR} - 0.25 \text{in}$$

$$r := \frac{r_0}{e^{-1}} \quad \text{radius to top of skin depth location}$$

$$w_{\text{w}} := \sqrt{r^2 - r_0^2} \quad \text{height above sensor loop}$$

$$w_{\text{total}} := h + 2 \cdot w$$

$$w_{\text{total}} = 2.296 \text{mm}$$

### Capacitance Estimation

$$w_{\text{ic}} := 127 \mu\text{m} \quad h_{\text{w}} := 202 \mu\text{m}$$

$$l_{\text{ic}} := 0.1 \text{in}$$

$$N_{\text{w}} := 11 \quad \epsilon_r := 3.5$$

$$A_1 := 4.409 \cdot \tanh \left[ 0.55 \left( \frac{202}{127} \right)^{0.45} \right] \cdot 10^{-6} \frac{\text{pF}}{\mu\text{m}} \quad A_2 := 9.92 \cdot \tanh \left[ 0.52 \left( \frac{202}{127} \right)^{0.5} \right] \cdot 10^{-6} \frac{\text{pF}}{\mu\text{m}}$$

$$C_L := (\epsilon_r + 1) \cdot l_{\text{ic}} \cdot [(N - 3)A_1 + A_2]$$

$$C_L = 0.303 \text{pF}$$

## Insert Material

$$f_{r\_plastic} := 1.435\text{GHz} \quad f_{l\_plastic} := 1.42125\text{GHz} \quad f_{u\_plastic} := 1.445\text{GHz}$$

$$Q_{plastic} := \frac{f_{r\_plastic}}{f_{u\_plastic} - f_{l\_plastic}}$$

$$Q_{plastic} = 60.421$$

$$f_{r\_copper} := 1.56\text{GHz} \quad f_{l\_copper} := 1.542\text{GHz} \quad f_{u\_copper} := 1.5915\text{GHz}$$

$$Q_{copper} := \frac{f_{r\_copper}}{f_{u\_copper} - f_{l\_copper}}$$

$$Q_{copper} = 31.515$$

$$f_{r\_hss} := 1.72\text{GHz} \quad f_{l\_hss} := 1.659\text{GHz} \quad f_{u\_hss} := 1.83\text{GHz}$$

$$Q_{hss} := \frac{f_{r\_hss}}{f_{u\_hss} - f_{l\_hss}}$$

$$Q_{hss} = 10.058$$

$$f_{r\_carbide} := 1.759\text{GHz} \quad f_{l\_carbide} := 1.733\text{GHz} \quad f_{u\_carbide} := 1.824\text{GHz}$$

$$Q_{carbide} := \frac{f_{r\_carbide}}{f_{u\_carbide} - f_{l\_carbide}}$$

$$Q_{carbide} = 19.33$$

$$f_{r\_carbide\_cu.ag} := 1.725GHz \quad f_{l\_carbide\_cu.ag} := 1.706GHz \quad f_{u\_carbide\_cu.ag} := 1.762GHz$$

$$Q_{carbide\_cu.ag} := \frac{f_{r\_carbide\_cu.ag}}{f_{u\_carbide\_cu.ag} - f_{l\_carbide\_cu.ag}}$$

$$Q_{carbide\_cu.ag} = 30.804$$

$$f_{r\_hss\_cu.ag} := 1.744GHz \quad f_{l\_hss\_cu.ag} := 1.723GHz \quad f_{u\_hss\_cu.ag} := 1.782GHz$$

$$Q_{hss\_cu.ag} := \frac{f_{r\_hss\_cu.ag}}{f_{u\_hss\_cu.ag} - f_{l\_hss\_cu.ag}}$$

$$Q_{hss\_cu.ag} = 29.559$$

### Dielectric Thickness

$$f_{r\_oneply} := 1.6557594375GHz \quad f_{l\_oneply} := 1.6407609375GHz \quad f_{u\_oneply} := 1.67169534375GHz$$

$$Q_{oneply} := \frac{f_{r\_oneply}}{f_{u\_oneply} - f_{l\_oneply}}$$

$$Q_{oneply} = 53.525$$

$$f_{r\_twoply} := 1.496400375GHz \quad f_{l\_twoply} := 1.48608890625GHz \quad f_{u\_twoply} := 1.5057744375GHz$$

$$Q_{twoply} := \frac{f_{r\_twoply}}{f_{u\_twoply} - f_{l\_twoply}}$$

$$Q_{twoply} = 76.015$$

## Matlab: Calculations and Plotting Routines

### Proof-of-Concept Section:

```
clc; clear all; close all;

strain=[2e-4:1e-5:11e-4];
f=475.1875;

% for i = 1:length(strain)
%     fstrained(i)=1/(2*pi*sqrt(1.121787e-7*(1+strain(i))));
%     fout(i)=f-fstrained(i);
% end

for i = 1:length(strain)
    delfovafpred(i)=strain(i)/2;
end
% plot(strain,fout)
% title('resonant frequency')
% figure
% plot(strain,fstrained)

figure
plot(strain,delfovafpred,strain,2.4943*strain-0.0002,'r')
title('Normalized change in frequency vs. strain');
xlabel('Strain (mm/mm)');
ylabel('\Deltaf/f_0');
legend('Predicted','Experimental',2);

clc; clear all; close all;

strain=[1e-6:1e-7:11e-4];
for i = 1:length(strain)
    delfovafpred2(i)=strain(i)/2;
end
figure
loglog(strain,delfovafpred2)
title('Predicted normalized change in frequency vs. strain');
xlabel('Strain (mm/mm)');
ylabel('\Deltaf/f_0');

%% plotting the traversing data

dist=[1.825,1.46,1.095,0.73,0.365,0,-0.365,-0.73,-1.095,-1.46,-1.825];
origfrq=[467.3125,471.1875,473.3125,474.375,475,475.1875,475,474.125,471.5,465.625,456.8125];
delf=[0.016572406,0.00841773,0.003945811,0.001709851,0.000394581,0,0.000394581,0.002235959,0.007760095,0.020123635,0.038668946];

[AX,H1,H2] = plotyy(dist,origfrq,dist,delf,'plot');
set(get(AX(1),'Ylabel'),'String','Frequency (MHz)')
set(get(AX(2),'Ylabel'),'String','\Deltaf/f_0 (MHz/MHz)')
xlabel('Displacement (mm)')
title('Frequency Shift due to Vertical Displacement')
```

```
set(H1,'LineStyle','--','Marker','*')
set(H2,'LineStyle','--','Marker','o')
```

### Probe Geometry Section:

#### Example Complex Impedance data import to Polar form and Plot Routine

%% impedance from rotation of single pass pcb loop with no resistance inside loop is 1.1pF capacitor

```
clear all;
importcsv('C:\Documents and Settings\UNH-FFR\Desktop\load balancing
v2\probe_resistance(8-16-11)\first loop\NO-RESISTANCE.CSV')
Freq = data(:,1)/1e9;
Z = data(:,2)+j*data(:,3);
Phase = angle(Z)*180/pi;
figure;
hold on;
grid on;
% Plotting the graph of freq versus real part of Z
Real= plot(Freq,real(Z),'color',[0 1 0],'LineWidth',2);
% Plotting the graph of freq versus imaginary part of Z
Img = plot(Freq,imag(Z),'color',[1 0 0],'LineWidth',2);
ylim([-300 300]);
% Plotting the graph of freq versus abs value of Z
Yamp=line(Freq,abs(Z),'color',[0 0 0],'LineWidth',2);
% Added two Yaxes i.e.,Yleft for amplitude and YRight for Phase
ax1= gca;
ylabel('Impedance (Ohms)');
ax2= axes('Position',get(ax1,'Position'),...
         'YAxisLocation','right',...
         'Color','none',...
         'YColor',[0 0 1]);
Yphase=line(Freq,Phase,'color',[0 0 1],'LineWidth',2,'parent',ax2);
ylim([-90 90]);
ylabel('Phase (Degree)');
xlabel('Frequency (GHz)');
%Added legend to graph
legend1=legend([Real Img Yamp
Yphase],'Real','Img','Magnitude','Phase',4);
title({'Impedance Variation for No resistance probe loop; ICCS/30AWG on
2 flute carbide'});
hold off;
```

### Probe Diameter Section:

```
%% skin depth
% variables
freq=[1.75e9:1e7:1.81e9]; %frequency range
mu_core=1.257e-6; %magnetic permeability of the core (air),
thus mu_not
sig_coil=5.96e7; %conductivity of the coil material (copper)

% calc
for i =1:length(freq)
    d(i)=sqrt(2/(2*pi*freq(i)*mu_core*sig_coil)); %skin depth
calculation
```



```

end

% plot routine
plot(freq,d);
title('Skin depth vs. Frequency');
xlabel('Frequency (Hz)');
ylabel('Skin Depth (m)');

%% self inductance of insert material
a=2.296e-3*d; %area of square inductor for insert material

for i=1:length(freq)
    radius_insertwire(i)=(a(i)/pi)^(1/2); %calculating radius for
circle conductor equal to square of inductor
end
radius_insertloop=(6.35e-3)-radius_insertwire; % radius of loop with
0.5in copper inductor based on radius

% calc
for i =1:length(freq)
    L_insert(i)=1.257e-
6*radius_insertloop(i)*(log((8*radius_insertloop(i))/radius_insertwire(
i))-2);
end

figure
plot(freq,L_insert);
title('Insert Inductance versus Frequency');
xlabel('Frequency (Hz)');
ylabel('Inductance (H)');

%% mutual inductance between sensor loop and insert material
a1=6.59e-3; %radius of sensor loop
radius_sensorwire=1.468e-4; %radius of the sensor wire
b1=radius_insertloop; %radius of the insert material loop
d1=(a1-radius_sensorwire)-(b1+radius_insertwire); %separation distance
between sensor and insert

% calculating mutual for sensor and insert
for i=1:length(freq)
    k(i)=sqrt(((4*a1*b1(i))/((a1+b1(i))^2+d1(i)^2)));
    [K1,E1] = ellipke(k(i));
    Mut_sensinsert(i)=1.257e-6*(a1*b1(i))^(0.5)*(((2/k(i))-k(i))*K1-
((2/k(i))*E1));
end

figure
plot(freq,Mut_sensinsert)
title('Sensor/Insert Mutual Inductance versus Frequency');
xlabel('Frequency (Hz)');
ylabel('Inductance (H)');

```

```

%% calculating total sensor/insert inductance
sen_ind=3.216e-8; %sensor inductance (H)

for i =1:length(freq)

total_sens_insert_ind(i)=(sen_ind*L_insert(i))/((sen_ind+L_insert(i)));
% no mutual

total_sens_insert_ind(i)=(sen_ind*L_insert(i))/((sen_ind+L_insert(i)));
end

figure
plot(freq,total_sens_insert_ind)
title('Total Sensor/Insert Inductance versus Frequency');
xlabel('Frequency (Hz)');
ylabel('Inductance (H)');

% calculating total sensor/insert inductance
probe_ind1=1.127e-8; %probe inductances
probe_mut1=19.598e-9; %probe/sensor mutual
probe_ind2=1.257e-8;
probe_mut2=17.834e-9;
probe_ind3=1.343e-8;
probe_mut3=16.73e-9;

for i =1:length(freq) %total system inductance
total_ind_probe1(i)=(probe_ind1*total_sens_insert_ind(i)-
probe_mut1^2)/((probe_ind1+total_sens_insert_ind(i))-2*probe_mut1);
total_ind_probe2(i)=(probe_ind2*total_sens_insert_ind(i)-
probe_mut2^2)/((probe_ind2+total_sens_insert_ind(i))-2*probe_mut2);
total_ind_probe3(i)=(probe_ind3*total_sens_insert_ind(i)-
probe_mut3^2)/((probe_ind3+total_sens_insert_ind(i))-2*probe_mut3);
end

figure
plot(freq,total_ind_probe1,freq,total_ind_probe2,freq,total_ind_probe3)
title('Total Inductance (probe/sensor/insert) versus Frequency');
xlabel('Frequency (Hz)');
ylabel('Inductance (H)');
%ylim([7e-9 8.2e-9]);
legend('14.53mm probe','15.09mm probe','15.54mm probe',1);

%% resistance of insert material, probe, sensor (rho*L/A)
rho=1.68e-8;
sig=5.96e7;

% cross section geometry
wprobe=8.128e-4; %horizontal width of probe trace (0.032in)
hsens=5.334e-5; %horizontal width of sensor band (0.0021in)
wsensor=1.27e-3; %vertical height of sensor band (0.05 in)
winsert=2.296e-3; %vertical height of insert skin depth
lprobe=18e-6; %veritcal height of probe trace (18um)

```

```

% circumferential lengths
sensleng=0.041;
probelleng=48.197e-3;
probe2leng=49.953e-3;
probe3leng=51.389e-3;

% area of current using skin depth
for i =1:length(freq)
    sd_area_probe(i)=(wprobe*hprobe)-((wprobe-2*d(i))*(hprobe-2*d(i)));
    sd_area_sensor(i)=(wsensor*hsens)-((wsensor-2*d(i))*(hsens-
2*d(i)));
end

% calc
for i =1:length(freq)
    res_insert(i)=(rho*2*pi*radius_insertloop(i))/(winsert*d(i)); % for
insert
    res_sensor(i)=(rho*sensleng)/(sd_area_sensor(i)); % for sensor
    res_probel(i)=(rho*probelleng)/(sd_area_probe(i)); % for probe1
    res_probe2(i)=(rho*probe2leng)/(sd_area_probe(i)); % for probe1
    res_probe3(i)=(rho*probe3leng)/(sd_area_probe(i)); % for probe1
end

figure;
plot(freq,res_insert);
title('Insert Resistance versus Frequency');
xlabel('Frequency (Hz)');
ylabel('Resistance (\Omega)');
figure;
plot(freq,res_sensor);
title('Sensor Resistance versus Frequency');
xlabel('Frequency (Hz)');
ylabel('Resistance (\Omega)');
figure;
plot(freq,res_probel,freq,res_probe2,freq,res_probe3);
title('Probe Resistance versus Frequency');
xlabel('Frequency (Hz)');
ylabel('Resistance (\Omega)');
legend('14.53mm','15.09mm','15.54mm',4);

for i =1:length(freq)
    total_res_reg1(i)=(res_insert(i)+res_sensor(i)+res_probel(i));
    total_res_reg2(i)=(res_insert(i)+res_sensor(i)+res_probe2(i));
    total_res_reg3(i)=(res_insert(i)+res_sensor(i)+res_probe3(i));
end
figure
plot(freq,total_res_reg1,freq,total_res_reg2,freq,total_res_reg3);
title('Total Resistance (probe/sensor/insert) versus Frequency');
xlabel('Frequency (Hz)');
ylabel('Resistance (\Omega)');
legend('14.53mm probe','15.09mm probe','15.54mm probe',4)

%% resistance due to skin depth using cap pressure sensor equation

```

```

% calc of resistance due to skin depth using cap pressure sensor
equation
for i =1:length(freq)
    xres_insert(i)=(rho*2*pi*radius_insertloop(i))/(winsert*d(i)*(1-
exp((-d(i))/d(i)))); % for insert
    xres_sensor(i)=(rho*sensleng)/(wsensor*d(i)*(1-exp((-
hsens)/d(i)))); % for sensor
    xres_probel(i)=(rho*probelleng)/(wprobe*d(i)*(1-exp((-
hprobe)/d(i)))); % for probel
    xres_probe2(i)=(rho*probe2leng)/(wprobe*d(i)*(1-exp((-
hprobe)/d(i)))); % for probel
    xres_probe3(i)=(rho*probe3leng)/(wprobe*d(i)*(1-exp((-
hprobe)/d(i)))); % for probel
end

figure;
plot(freq,xres_insert);
title('Insert Resistance versus Frequency');
xlabel('Frequency (Hz)');
ylabel('Resistance (\Omega)');
figure;
plot(freq,xres_sensor);
title('Sensor Resistance versus Frequency');
xlabel('Frequency (Hz)');
ylabel('Resistance (\Omega)');
figure;
plot(freq,xres_probel,freq,xres_probe2,freq,xres_probe3);
title('Probe Resistance versus Frequency');
xlabel('Frequency (Hz)');
ylabel('Resistance (\Omega)');
legend('14.53mm', '15.09mm', '15.54mm', 4);

for i =1:length(freq)
    total_resx1(i)=(xres_insert(i)+xres_sensor(i)+xres_probel(i));
    total_resx2(i)=(xres_insert(i)+xres_sensor(i)+xres_probe2(i));
    total_resx3(i)=(xres_insert(i)+xres_sensor(i)+xres_probe3(i));
end
figure;
plot(freq,total_resx1,freq,total_resx2,freq,total_resx3);
title('Total Resistance (probe/sensor/insert) versus Frequency');
xlabel('Frequency (Hz)');
ylabel('Resistance (\Omega)');
legend('14.53mm probe', '15.09mm probe', '15.54mm probe', 4)

```

### Sensor Capacitance Section:

```
%% plot of global resonance data
```

```

discretcaps=[0.1 0.2 0.3 0.4 0.5 0.6 0.7 0.8 0.9 1.5 0.6 0.6 11.55];
dc_freq=[2.3 2.1 1.95 1.88 1.79 1.65 1.59 1.53 1.39 1.18 1.65 1.5 0.5];

pocap=[1.73 3.39 5.89 2.471 1.968 3.704 5.84];
po_freq=[1.66 1.2 0.98 1.092 1.027 0.82103 0.73354];

```

```

freq=linspace(0.05,12);
capfit=1.3805*freq.^(-0.294);

plot(discretecaps,dc_freq,'+',pocap,po_freq,'*',freq,capfit);
axis([0 12 0 3]);
title('HSS or Carbide tool insert sensor loops');
xlabel('Capacitance (pF)');
ylabel('Frequency (GHz)');
legend('Discrete Capacitors','Overlap Capacitors','Power Law');

%% simulation for variable d in capacitance equation
%electrical properties
e_0=8.85e-12; % (F/m)
etot=3.8*e_0;

%glue and dielectric thickness
d_glue=3.16e-4; %separation distance
d_poly=5.08e-5;
d_glue=d_glue-d_poly;
d_poly_tol=[d_poly-(d_poly*.1):d_poly/20:d_poly+(d_poly*.1)];

dtot=d_glue+d_poly_tol;

x=ones(1,5);
frqc0=x*1.092; frqca=x*1.027; frqcb=x*0.82103; frqcc=x*0.73354;
frqc1=x*1.66; frqc2=x*1.2; frqc3=x*0.98;

%displaced 2.471 pF sensor
w0=2.54e-3;
l0=9.144e-3;
c0=(w0*l0*etot)./dtot;
c0=c0*10^12

%displaced 1.968 pF sensor
wa=2.388e-3;
la=7.747e-3;
ca=(wa*la*etot)./dtot;
ca=ca*10^12

%displaced 3.704 pF sensor
wb=2.388e-3;
lb=0.015;
cb=(wb*lb*etot)./dtot;
cb=cb*10^12

%displaced 5.84 pF sensor
wc=2.388e-3;
lc=0.023;
cc=(wc*lc*etot)./dtot;
cc=cc*10^12

%1.73 pF sensor

```

```

w1=2.794e-3;
l1=5.842e-3;
c1=(w1*l1*etot) ./dtot;
c1=c1*10^12

%3.398 pF sensor
w2=2.794e-3;
l2=0.011;
c2=(w2*l2*etot) ./dtot;
c2=c2*10^12

%5.89 pF sensor
w3=2.794e-3;
l3=0.02;
c3=(w3*l3*etot) ./dtot;
c3=c3*10^12

plot(c0, frqc0, 'b', ca, frqca, 'b', cb, frqcb, 'b', cc, frqcc, 'b', c1, frqc1, 'b', c2, frqc2, 'b', c3, frqc3, 'b')
axis([.5 8 0 2]);
title('Pyrallax Manufacturing Tolerance Influence on Capacitance Estimation');
xlabel('Capacitance (pF)');
ylabel('Frequency (GHz)');
hold on

ha=1.71*ones(1,6); hb=1.765*ones(1,6);
vbar=1.66; vtot=[vbar-0.025:0.01:vbar+0.025];

h2=1.938*ones(1,6); h3=2.001*ones(1,6);
vbar=1.027; vtot2=[vbar-0.025:0.01:vbar+0.025];

h4=2.433*ones(1,6); h5=2.512*ones(1,6);
vbar=1.092; vtot3=[vbar-0.025:0.01:vbar+0.025];

h6=3.874*ones(1,6); h7=3.752*ones(1,6);
vbar=0.821; vtot4=[vbar-0.025:0.01:vbar+0.025];

h8=3.219*ones(1,6); h9=3.324*ones(1,6);
vbar=1.2; vtot5=[vbar-0.025:0.01:vbar+0.025];

h10=5.853*ones(1,6); h11=6.044*ones(1,6);
vbar=0.98; vtot6=[vbar-0.025:0.01:vbar+0.025];

h12=5.753*ones(1,6); h13=5.941*ones(1,6);
vbar=0.7335; vtot7=[vbar-0.025:0.01:vbar+0.025];

hold on
plot(ha,vtot,'b',hb,vtot,'b')
plot(h2,vtot2,'b',h3,vtot2,'b')
plot(h4,vtot3,'b',h5,vtot3,'b')
plot(h6,vtot4,'b',h7,vtot4,'b')
plot(h8,vtot5,'b',h9,vtot5,'b')
plot(h10,vtot6,'b',h11,vtot6,'b')
plot(h12,vtot7,'b',h13,vtot7,'b')

```

```

hold off

%% variance due to permittivity
k=[-.175:.025:.175];
etot=(3.8+k)*e_0;
dtot=d_glue+d_poly;

x=ones(1,15);
frqc0=x*1.092; frqca=x*1.027; frqcb=x*0.82103; frqcc=x*0.73354;
frqc1=x*1.66; frqc2=x*1.2; frqc3=x*0.98;

%displaced 2.471 pF sensor
w0=2.54e-3;
l0=9.144e-3;
c0=(w0*l0.*etot)/dtot;
c0=c0*10^12

%displaced 1.968 pF sensor
wa=2.388e-3;
la=7.747e-3;
ca=(wa*la.*etot)/dtot;
ca=ca*10^12

%displaced 3.704 pF sensor
wb=2.388e-3;
lb=0.015;
cb=(wb*lb.*etot)/dtot;
cb=cb*10^12

%displaced 5.84 pF sensor
wc=2.388e-3;
lc=0.023;
cc=(wc*lc.*etot)/dtot;
cc=cc*10^12

%1.73 pF sensor
w1=2.794e-3;
l1=5.842e-3;
c1=(w1*l1.*etot)/dtot;
c1=c1*10^12

%3.398 pF sensor
w2=2.794e-3;
l2=0.011;
c2=(w2*l2.*etot)/dtot;
c2=c2*10^12

%5.89 pF sensor
w3=2.794e-3;
l3=0.02;
c3=(w3*l3.*etot)/dtot;
c3=c3*10^12

plot(c0,frqc0,'b',ca,frqca,'b',cb,frqcb,'b',cc,frqcc,'b',c1,frqc1,'b',c
2,frqc2,'b',c3,frqc3,'b')

```

```

axis([.5 8 0 2]);
title('Simulated \epsilon_r Influence on Capacitance Estimation');
xlabel('Capacitance (pF)');
ylabel('Frequency (GHz)');
hold on

ha=1.657*ones(1,6); hb=1.817*ones(1,6);
vbar=1.66; vtot=[vbar-0.025:0.01:vbar+0.025];

h2=1.878*ones(1,6); h3=2.059*ones(1,6);
vbar=1.027; vtot2=[vbar-0.025:0.01:vbar+0.025];

h4=2.358*ones(1,6); h5=2.586*ones(1,6);
vbar=1.092; vtot3=[vbar-0.025:0.01:vbar+0.025];

h6=3.637*ones(1,6); h7=3.988*ones(1,6);
vbar=0.821; vtot4=[vbar-0.025:0.01:vbar+0.025];

h8=3.12*ones(1,6); h9=3.421*ones(1,6);
vbar=1.2; vtot5=[vbar-0.025:0.01:vbar+0.025];

h10=5.673*ones(1,6); h11=6.221*ones(1,6);
vbar=0.98; vtot6=[vbar-0.025:0.01:vbar+0.025];

h12=5.576*ones(1,6); h13=6.114*ones(1,6);
vbar=0.7335; vtot7=[vbar-0.025:0.01:vbar+0.025];

hold on
plot(ha,vtot,'b',hb,vtot,'b')
plot(h2,vtot2,'b',h3,vtot2,'b')
plot(h4,vtot3,'b',h5,vtot3,'b')
plot(h6,vtot4,'b',h7,vtot4,'b')
plot(h8,vtot5,'b',h9,vtot5,'b')
plot(h10,vtot6,'b',h11,vtot6,'b')
plot(h12,vtot7,'b',h13,vtot7,'b')
hold off

```

### Sensor Capacitance Section:

```

strain(1)=1e-5;
strain(2)=4e-5;
strain(3)=1e-4;
strain(4)=4e-4;
strain(5)=1e-2;
strain(6)=0;
nu = .25;
N=12; % number of fingers
perm=8.85e-12; %permittivity in F/m
k=4; %relative permittivity

for c=1:6 %strain transverse to fingers
    L = .0254*.05*(1+nu*strain(c)); %finger length
    s = .005*.0254*(1-strain(c)); %spacing in meters
    w=.005*.0254*(1-strain(c)); %width of finger
    dum = 0;

```



```

    for n=1:100
        argument=(2*n-1)*pi*s/(2*(s+w));
        dum= dum+(besselj(0,argument))^2;
    end
    cap(c)=dum*L*N*4*perm*k/pi;
end
% z=(cap-cap(6))/cap(6);
% p=polyfit(strain,z,1)
% slope=p(1)
% for c=1:6 % strain along finger
%     L = .0254*.05*(1+strain(c)); %finger length
%     s= .005*.0254*(1-nu*strain(c)); %spacing in meters
%     w=.005*.0254*(1-nu*strain(c)); %width of finger
%     dum = 0;
%
%     for n=1:100
%         argument=(2*n-1)*pi*s/(2*(s+w));
%         dum= dum+(besselj(0,argument))^2;
%     end
%     cap(c)=dum*L*N*4*perm*k/pi
% end
loglog((cap-cap(6))/cap(6),strain)
xlim([10^-5 10^-2])
xlabel ('Strain')
ylabel ('\DeltaC/C')
title('Strain sensitivity of gauge mounted parallel to load axis')

```